Continuous Crystallization in a Helically Coiled Flow Tube Crystallizer

Dissertation
zur Erlangung des akademischen Grades

Doktoringenieurin
(Dr.-Ing.)

von M. Sc. Viktoria Wiedmeyer
geb. am 02. Mai 1988 in Beckendorf-Neindorf

genehmigt durch die Fakultät für Verfahrens- und Systemtechnik der Otto-von-Guericke-Universität Magdeburg

Promotionskommission:
- Apl. Prof. Dr. rer. nat. Heike Lorenz (Vorsitz)
- Prof. Dr.-Ing. habil. Kai Sundmacher (Gutachter)
- Univ.-Prof. Dipl.-Ing. Dr. techn. Johannes Khinast (Gutachter)
- Prof. Dr.-Ing. Norbert Kockmann (Gutachter)

eingereicht am: 27. November 2019
Promotionskolloquium am: 30. Juni 2020

Abstract

This dissertation discusses a tubular setup with regard to its potential for continuous crystallization of narrow crystal size distributions. This application of tubular setups is motivated by a demand for new devices and strategies for continuous crystallization on a small scale. Among the continuous crystallizers is the helically coiled flow tube, which combines the advantages of high mass and heat transfer rates for cooling crystallization.

The dissertation is divided into three main parts. First, residence time distributions and crystal growth are determined experimentally in straight tubes and in helically coiled flow tubes. Next, a momentum balance model is developed to validate the measured particle residence time distributions. Finally, the evolution of crystal size distributions in helically coiled flow tubes is modeled and simulated with a coupled population balance equation system.

This study shows in crystallization experiments that an improved radial mixing and more uniform residence time distributions are reached by using helically coiled flow tubes rather than straight tubes. In helically coiled flow tube crystallizers, flow rates in the transient and turbulent regimes are neither necessary nor beneficial. The operation at laminar flow rates enables relatively long residence times and large final crystal sizes after crystal growth, even at short tube lengths. For this reason, helically coiled flow tube crystallizers can be realized with low pressure loss.

The residence times of non-neutrally buoyant spherical particles and angular crystals are measured experimentally in straight and helically coiled flow tubes. In both setups, large particles are faster than small particles, a finding observed for the first time, here, for crystals in helically coiled flow tubes. The observation can be explained, in a first approximation, by a newly developed model. The movement of single particles in straight tubes is modeled with a momentum balance. Forces dominating particle residence time are identified, and the experimental size dependency of the residence time distribution is reproduced. The residence time distribution is independent of the wall material, which allows the material to be chosen depending on the application. Moreover, the findings of this study can also be applied to other solid-liquid processes with spherical and irregular particles.

The population balance equation system is parameterized from seeded batch experiments. Subsequently, continuous growth-dominated crystallization in helically coiled flow tubes is simulated. Though plug flow is not reached, a size-dependent residence time is advantageous because small crystals have more time to grow than large ones. Therefore, helically coiled flow tubes offer the potential to narrow crystal size distributions. For potash alum, independent of seed crystal size distributions, the width of crystal size distributions remains nearly constant despite growth rate dispersion. It is shown that narrow crystal size distributions can be produced in the device, during cooling crystallization, at laminar flow rates. Furthermore, a large product mass flow of large crystals and a high yield can be reached simultaneously, in helically coiled flow tubes. Hence, the dissertation is an important step towards the industrial application of continuous crystallization for narrowly distributed size-specific crystals.

Kurzzusammenfassung

In dieser Arbeit wird das Potential eines Strömungsrohres für die Kristallisation untersucht. In der kontinuierlichen Kristallisation wurden zuletzt vermehrt neue kontinuierliche Apparate und Konzepte für kleinvolumige Produkte entwickelt. Darunter befinden sich Wendelrohrkristaller, die hohe Stoff- und Wärmetransportraten ermöglichen und so Vorteile für die Kühlungskristallisation bieten.

Die Arbeit gliedert sich in drei Teile. Zuerst werden Verweilzeitverteilungen und Wachstumsraten experimentell in geraden Rohren und in Wendelrohren gemessen. Um die Verweilzeitverteilungen zu validieren, wird die Partikelbewegung basierend auf einer Momentenbilanz modelliert. Schließlich wird die Entwicklung der Kristallgrößenverteilung in Wendelrohren mit einem gekoppelten Populationsbilanzsystem modelliert und simuliert.

Für die Kristallisation sollten Wendelrohre gegenüber geraden Rohren bevorzugt werden, da sie eine bessere radiale Vermischung und engere Verweilzeitverteilungen ermöglichen. Es wird gezeigt, dass in den Wendelrohren dafür keine instationären oder turbulenten Strömungsgeschwindigkeiten notwendig sind. Der Betrieb bei laminaren Bedingungen ermöglicht somit auch in kurzen Rohren lange Verweilzeiten zur Erzeugung großer Kristalle durch Wachstum. Dadurch können Wendelrohrkristaller mit niedrigem Druckverlust betrieben werden.

Die Partikelverweilzeit wird für übliche kugelförmige Partikel und auch für eckige Kristalle experimentell bestimmt. Sowohl in geraden Rohren als auch in Wendelrohren sind große Partikel schneller als kleine Partikel. Für Kristalle wurde diese partikelgrößenabhängige Verweilzeit das erste Mal im Wendelrohr beobachtet und sie kann mit einem neu entwickelten Impulsbilanzmodell in erster Näherung erklärt werden. Das Modell beschreibt die Bewegung eines einzelnen Partikels in einem geraden Rohr. Dadurch können die Kräfte identifiziert werden, die die partikelgrößenabhängige Verweilzeit verursachen. Die Verweilzeitverteilung ist unabhängig vom Wandmaterial. Bei der Implementierung eines Wendelrohrkristallers kann das Wandmaterial daher je nach Anwendung frei ausgewählt werden. Die Verweilzeitergebnisse können auch für andere Fest-Flüssig-Prozesse in Wendelrohren mit kugelförmigen und unregelmäßigen Partikeln relevant sein.

Das Populationsbilanzsystem wird basierend auf Batch-Experimenten unter Zugabe von Saatkristallen parametrisiert. Dies ermöglicht die Simulation der kontinuierlichen wachstumsdominierten Kristallisation im Wendelrohr. Auch wenn keine ideale Pfropfenströmung erreicht wird, ist eine partikelgrößenabhängige Verweilzeit vorteilhaft, da kleine Kristalle mehr Zeit zum Wachsen haben als große Kristalle. Dadurch haben Wendelrohre das Potential Kristallpopulationen mit einer engen Größenverteilung zu erzeugen. Für Kalialaun bleibt die Breite der Kristallgrößenverteilung trotz Wachstumsratendispersion, unabhängig von der Anfangsverteilung, nahezu konstant. Es wird gezeigt, dass mittels Kristallwachstum in Wendelrohren enge Kristallgrößenverteilungen bei laminaren Strömungsgeschwindigkeiten erzeugt werden. Gleichzeitig können große Massenströme, große Kristalle und hohe Ausbeuten erreicht werden. Damit stellt die Arbeit einen wichtigen Schritt zur kontinuierlichen Kristallisation von engen Kristallgrößenverteilungen für industrielle Anwendungen dar.

Contents

Notation

Latin Symbols

Symbol	Unit	Definition
$\mathbf{a}$	$\mathrm{m\,s^{-2}}$	acceleration vector
a	$\mathrm{m\,s^{-2}}$	acceleration
b	m	tube wall thickness
c_D	$-$	drag coefficient
d	m	diameter
d_p	m	sphere volume equivalent particle diameter
D	$\mathrm{m^2\,s^{-1}}$	dispersion coefficient
De	$-$	Dean number
e_c	$-$	collision elasticity coefficient
f	$\mathrm{m^{-1}}$	number density distribution
$\dot{f}$	$\mathrm{m^{-1}\,s^{-1}}$	number density distribution flow rate
f_D	$-$	correction factor of the Stokes drag force
f_G	$-$	Goldman correction factor of the drag force
f_M	$-$	correction factor of the Magnus force
f_S	$-$	correction factor of the Saffman force
$\mathbf{F}$	$\mathrm{m\,kg\,s^{-2}}$	force vector in Cartesian coordinates
F	$\mathrm{m\,kg\,s^{-2}}$	absolute value of a component of the force
g	$\mathrm{m\,s^{-2}}$	gravity of Earth
$\mathbf{G}$	$\mathrm{m\,s^{-1}}$	growth and dissolution rate vector
G	$\mathrm{m\,s^{-1}}$	growth and dissolution rate of one crystal face
$\mathbf{h}$	m	vector of perpendicular distances of crystal faces from crystal center
h	m	perpendicular distance of a crystal face from crystal center
Δh	m	width of a control volume in h
i	$-$	index of finite control volume along the h-coordinate
j	$-$	index of finite control volume along the z-coordinate
k_V	$-$	volumetric shape factor
l	m	tube length
m	kg	mass
$\dot{m}$	$\mathrm{kg\,s^{-1}}$	mass flow rate
M	$\mathrm{kg\,mol^{-1}}$	molar mass
n_t	$-$	index of the current time step
N	$-$	number of control volumes
p	m	screw pitch
p_1	$\mathrm{m\,s^{-1}}$	pre-exponential factor of the growth and dissolution kinetics
p_2	$\mathrm{J\,mol^{-1}}$	activation energy of the growth kinetics

Symbol	Unit	Definition
p_3	–	exponent of the growth and dissolution kinetics
Δp	Pa	pressure drop
P	–	dimensionless pitch
r	–	the ratio of successive gradients on the grid of finite control volumes
$\mathbf{r}$	m	Cartesian coordinate vector
R	m	tube radius
R_m	$\mathrm{J\,mol^{-1}\,K^{-1}}$	molar gas constant
Re	–	Reynolds number
Re_critical	–	critical Reynolds number
Re_r	–	Reynolds number of rotation
Re_s	–	shear Reynolds number
St	–	Stokes number
t_c	–	torsion parameter
t	s	time
Δt	s	time step
T	K	temperature
$\mathbf{v}$	$\mathrm{m\,s^{-1}}$	linear velocity vector
v	$\mathrm{m\,s^{-1}}$	absolute value of a component of the linear velocity
v_f	$\mathrm{m\,s^{-1}}$	average fluid velocity
V	$\mathrm{m^3}$	volume
w	kg hydrate per kg added H_2O	mass loading in the fluid
x	m	horizontal coordinate in the circular cross-section of the tube
y	m	vertical coordinate in the circular cross-section of the tube
Δz	m	width of a control volume in z in finite volume method (in Chapter 6); step size in z in forward implementation (in Appendix A)
z	m	axial tube coordinate

Greek Symbols

Symbol	Unit	Definition
α	$^\circ$	azimuth
β_{Re}	–	dimensionless shear rate
β	$^\circ$	angle between particle velocity and its component perpendicular to the wall before wall collision
δ	m	shortest distance between tube wall and sphere hull
ε	–	small parameter to avoid zero division
η	%	yield
η_f	$\mathrm{kg\,m^{-1}\,s^{-1}}$	dynamic viscosity of the fluid
ϑ	°C	temperature
κ	$\mathrm{S\,m^{-1}}$	conductivity
λ	–	curvature ratio
$\lambda_\mathrm{friction}$	–	Darcy friction coefficient
μ	m	arithmetic mean of the seed size h
μ_c	–	collision friction coefficient
ρ	$\mathrm{kg\,m^{-3}}$	density
σ	–	relative supersaturation
τ	s	residence time
Φ	–	slope limiter function
χ_anh	–	fraction of the molar masses of the anhydrate to the hydrate
$\boldsymbol{\omega}$	$\mathrm{rad\,s^{-1}}$	angular velocity vector
ω	$\mathrm{rad\,s^{-1}}$	angular velocity of a component

Subscripts

Symbol	Definition
a	setup a
anh	anhydrate
batch	batch seeding
b	setup b
c	coil
conti	continuous seeding
D	drag
down	downward flow
elastic	perfectly elastic collision
f	fluid
GB	gravity and buoyancy
high	high flow rate
hyd	hydrate
in	inlet (seed addition point)
inlet	tube section before the seed addition point
I	first quadrant
low	low flow rate
M	Magnus
min	minimum (internal or external coordinate)
max	maximum (internal or external coordinate, Hagen-Poiseuille velocity)
n	normal
out	outlet
p	particle (phase)
parallel	movement parallel to a wall
rel	relative velocity between fluid and particle
sat	equilibrium saturation at a given temperature
seed	seed crystals
seed,small	seed crystals of the small fraction
seed,mix	seed crystals of the mixed fraction
S	Saffman
tracer	total tube section from reservoir to outlet
up	upward flow
w	water
w,added	free or added water
wall	wall collision

Superscripts

Symbol	Definition
a	next time step after a wall collision
b	current time step before a wall collision

Abbreviations

CFD	computational fluid dynamics
CFI	coiled flow inverter
CSD	crystal size distribution
CSSD	crystal size and shape distribution
DEM	discrete element method
HCT	helically coiled flow tube
KDP	potassium dihydrogen phosphate
FVM	finite volume method
MSMPR	mixed suspension mixed product removal
MSMPRC	mixed suspension mixed product removal crystallizer
ODE	ordinary differential equation
PDE	partial differential equation
PBE	population balance equation
PF	plug flow
RT	residence time
RTD	residence time distribution

1 Introduction

Motivation

The first industrial crystallizers emerged about 150 years ago (Hofmann and Melches, 2013). In the 1960s, continuous units for large tonnage bulk commodity products were developed. In the following decades, new strategies for the production of specialty-effect chemicals on a smaller scale were required, and batch and semibatch crystallizers were manufactured (Tavare, 1995). Around the millennium, research on continuous crystallization intensified again. Research and industry consortia emerged, such as the Novartis-MIT center for Continuous Manufacturing in the U.S., which was launched in 2007, and the CMAC Future Manufacturing Research Hub in the UK, which started in 2011. Further initiatives in pharmaceutical crystallization are listed by Khinast and Rantanen (2017). Researchers have been trained in the network CORE (Continuous Resolution and Deracemization of Chiral Compounds by Crystallization) since 2016. In 2018, the European Research Council assigned an ERC Advanced Grant in this area, for studying secondary nucleation for the intensification of continuous crystallization (SNICC). The development and application of continuous processes were also encouraged by regulatory authorities. The U.S. Food and Drug Administration (2004) recommended that: "gains in quality, safety and/or efficiency [...] are likely to come from: [...] Facilitating continuous processing to improve efficiency and manage variability. For example, use of dedicated small-scale equipment (to eliminate certain scale-up issues)".

Crystallization is usually but one step in long process chains and is therefore part of many production chains for solid chemicals. In the pharmaceutical industry, most production lines contain at least one, but usually several, crystallization steps (ter Horst et al., 2015). When these chains become continuous (Khinast and Rantanen, 2017), this also applies to the integration of crystallization steps. Further, measures for containment constrain pharmaceutical production (Khinast and Rantanen, 2017). Fully connected chains facilitate inherent containment for employee protection. To this end, the development of continuous crystallization processes is necessary. They must be characterized, in order to identify possible applications and limitations. New strategies, like preferential continuous crystallization and periodic seeding, have been developed, e.g., by Qamar et al. (2013). On the one hand, traditional tools can be applied to these new strategies, or to devices that are new in the field, such as helically coiled flow tubes (HCTs) and coiled flow inverters (CFIs). On the other hand, improved tools for simulation, measurement and control can be applied.

One of the first reports on fluid flow in curved tubes was published by Dean (1927). Later, computational power permitted the simulation of fluid flow in curved tubes, which was intensely studied by Nigam and his co-researchers since the 1980s (Saxena and Nigam, 1983). The complexity of simulations increased in conjunction with numerical capacity, to study complete fluid flow and heat fields in coiled tubes (Kumar and Nigam, 2005; Wiedmeyer et al., 2017a). The particle phase was modeled (Cheng et al., 2005) and, then, also simulated, e.g., for fibers (Redlinger-Pohn et al., 2016b) in coiled tubes.

From an experimental perspective, crystallization is a traditional purification technique

and well established. This allows focus to be directed on secondary goals, next to purification. Some of these goals are related to crystal size distribution (CSD) and crystal size and shape distribution (CSSD) since these influence the effectiveness of downstream steps (Winn and Doherty, 2000) and the product quality (Hofmann and Melches, 2013). With respect to downstream processing, crystal compactness and width of the CSD impact the efficiency of solid-liquid separation, flowability influences transport, and dusting, and the CSD is relevant for storage in silos. In terms of product features, crystal faces determine the dissolution rate and the bioavailability of pharmaceuticals in the body (Variankaval et al., 2008), whereas reactive faces influence the performance of catalysts (Yang et al., 2008). To analyze the CSD and CSSD, several tools are available, e.g., in-situ and in-line single and dual projection imaging devices, off-line laser diffraction, Coulter counter, and in-situ focused beam reflectance measurement. The research of de Albuquerque et al. (2016) concluded that among these principles, only imaging techniques are able to reproduce the concentration profile and average length exactly. Considering imaging, the resolution and the limit of frame rates have also risen with the increase in computational power. This improvement allows online imaging and control (Eisenschmidt et al., 2016) based on crystal shape estimation with high accuracy (Borchert et al., 2014).

Uniform CSDs are often desired in crystallization. In the mixed suspension mixed product removal (MSMPR) concept, the residence time distribution (RTD) and the resulting CSD are broad. This is countered industrially by the classification of different crystals in a suitable crystallizer geometry, e.g., on a large scale, in the Oslo crystallizer (Hofmann and Melches, 2013). Another approach is to approximate plug flow in tubes for which one tubular arrangement is the HCT. HCTs have a wide application area. They facilitate high heat transfer rates and are therefore typically applied for heat exchange. The potential of HCTs for chemical reaction engineering was recognized in the 1950s (Jokiel and Sundmacher, 2019). In the area of food processing, the transport of spherical particles in coiled tubes has been studied experimentally. In crystallization, studies with pharmaceutical application have been published in the last years, of which one of the earliest was that of Eder et al. (2010).

Aim of the Dissertation

In crystallization processes, several crystallization phenomena occur simultaneously. The mechanisms of these phenomena, the affecting parameters, and how to model the phenomena are still not fully understood. To study the phenomena separately, process design can suppress some phenomena to a certain extent. Hydrodynamics affect not only the mixing of the liquid phase, thus, crystallization, but also the movement of populations of angular crystals. Hence, the flow influences some crystallization phenomena directly. The development of crystallizers requires an understanding of different scales. This dissertation shall contribute to the exploration of the process unit scale. Which is why the potential of HCTs for application in cooling crystallization is investigated. Using a tubular device, crystal breakage by crystal-stirrer collisions of high impact can be avoided. This is advantageous since breakage broadens the CSD. The aim of this dissertation is to identify the potential of the device to achieve narrow product CSDs and to prevent broadening of the initial CSD. A final crystal size after crystal growth is determined by the time for crystal growth, which is the crystal residence time. This study demonstrates the effect of fluid and crystal RTD on the width of the CSD. Maintaining a high yield is set as a secondary goal. Novel imaging tools and postprocessing are applied for accurate estimation of crystal size from crystal shape. The characterization of the device is ex-

perimentally performed in batch mode. Predictions for continuous operation are derived from modeling and simulations.

The present dissertation investigates the following questions:

1. What forces determine the particle RTD in HCTs?
2. How do wall material and flow direction affect the RTD of fluid and particles?
3. Is the mixing sufficient for crystallization experiments?
4. How do tube length, flow rate, as well as mass and width of the CSD affect RTD, CSD, product mass and yield for batch and steady seeding?
5. Can crystal populations of narrow CSD be produced in HCTs?

Numerous scientifically connected research topics lie beyond the scope of this study. Some of the closely related ones are listed as follows: This dissertation is limited to laminar flow, to keep tube lengths short. In the turbulent regime, mixing would change completely. The characteristic dimensions of the HCT such as ratios of particle to tube diameter, particle to coil diameter, and inner tube to coil diameter are similar in all experimental setups. Experiments with continuous seeding were not performed. Instead, batch seeding led to low suspension densities. Purity and the influence of additives are not discussed. This study assumes that crystal growth prevails and focuses only on this crystallization phenomenon. Additionally, the influence of aggregation might be significant for other substances and conditions. Dissolution was not applied although it is a powerful control variable to further change the CSD in the device. Growth rates are not parameterized, but kinetics from literature are selected. Imaging is applied to estimate crystal shapes, to calculate a measure of crystal size and a CSD. Existing imaging algorithms are adapted to the substance, whereas imaging itself is not a topic of this dissertation. A multivariate shape distribution is not considered. Variations of the liquid phase in the circular cross-section of the tubes are not taken into account. Advanced numerical methods are not applied to simulate the particle flow. Process control and optimization, for example of the temperature profile, are no matter of concern either.

Outline of the Dissertation

First, residence time (RT) and, in a second step, crystallization experiments are performed. Regarding the setup, reference RT measurements are conducted with spherical particles in straight tubes. These experiments had been performed before RT experiments in HCTs, since a more complex flow profile is expected for HCTs. The forces determining the particle RTD are identified for, in terms of momentum balances “simpler”, straight tubes. Third, modifications for HCTs are discussed. Last, crystallization in HCTs is modeled and simulated.

In Chapter 2, requirements and applications of continuous crystallizers are stated. Among these types of crystallizers, HCTs are classified in terms of mixing and RT. To this end, characteristic measures of the device are introduced and the state-of-the-art in flow field characterization is presented. Current applications of HCTs, in particular in crystallization, are reviewed.

In Chapter 3, RT experiments with glass beads of varying sizes are described for straight tubes of different wall materials.

In Chapter 4, various implemented HCT setups are presented. The results of fluid and crystal RT measurements are analyzed before conducting crystal growth experiments. The effect of the variation of several parameters like flow direction, wall material, fluid flow rates, and crystal size on the RTDs is evaluated.

In Chapter 5, a momentum balance model is implemented for the spherical glass beads in the straight tubes from Chapter 3. The trajectory of single particles is simulated. The RTs are calculated for the conditions in the experimental part. Finally, the transferability to HCTs is discussed.

In Chapter 6, a population balance model is developed for those HCTs presented in Chapter 4. The model is discretized via finite volume method (FVM) and then implemented. The fluid and crystal flow is simulated firstly without growth to determine the RTDs, next, with crystal growth. The simulation results are compared to the findings of the experiments. Continuously seeded crystallization in an HCT is also modeled and predicted via simulations.

In Chapter 7, the dissertation is summarized and concluded.

2 Selection of a Continuous HCT Crystallizer

In order to generate supersaturation, the method of cooling crystallization from solution is applied. Regarding substances, inorganic salts are analyzed in the solvent water. Crystallization is induced by the seeding of crystals. The setup is an HCT crystallizer. From a process view, tubular setups are an option to realize continuous crystallization. In this section, the setup is classified by the extent of mixing, by the mode of operation, and by the crystallizer model. Common deviations from ideal models are stated.

2.1 Process Goals

The choice of the crystallizer type depends on the priority of the main goals of the crystallization process. The main goal is solidification or purification. Further goals relate to the product specifications.

An overview of product properties is given by Wieckhusen (2013). Those that can be influenced directly are purity, yield, crystal size and shape distributions, and the crystal form (polymorph, solvate). Properties that can indirectly be influenced are downstream properties, such as filterability, drying ability, flowability, and bulk density. Additionally, there might be constraints on the process that have to be considered, like process integration, safety aspects related to heating or to the containment for employee protection, the ability for an expected scale-up, and economic aspects. Additional demands may focus on a wide operation window, concerning substance systems and flow rates (Klutz et al., 2015). The amount of supplied feed liquor and the production rate may be limited (Tavare, 1995). Low pressure drop, a sufficient fluidization of the particles, a practical realizable cooling profile (Hohmann et al., 2016a), and a compact design (Klutz et al., 2015) are desired.

The present study strives to fulfill purity requirements. The primary goal is to reach a defined CSD. The CSD influences product properties, such as the dissolution rate, related to, e.g., bioavailability and downstream processes. Downstream steps can be milling, transportation, storage, and solid liquid separation like filtration, washing, and drying. It is assumed that a narrow distribution is desired for improved downstream processing, concerning, among others, filterability and flowability (Sparks and Chase, 2016). In general, for a narrow product CSD, it is advantageous to have a process with a narrow RTD. In special cases, the statement needs to be modified since initially monodisperse crystal distributions may broaden in any process, due to growth rate dispersion, independent of the RTD. Classification of crystals of certain sizes may be superior to a crystallization process with uniform RTDs.

2.2 Types of Mixing

Crystallizers can be classified by their type of mixing. Howell et al. (2004) divide microfluidic devices into active and passive mixers. Active mixers are based on an external force or field. Passive mixers rely on the movement of the fluid on or over stationary structures. On the one hand, a division of the inlet stream and the merging at injection or mixing points may cause passive mixing. On the other hand, an apparatus geometry may perturb the flow, for example by ridges, troughs, bends, or herringbone constructions. Active mixers are effective but expensive to fabricate, complicated to operate, and more error-prone than passive mixers (Howell et al., 2004). Consequently, passive mixers are advantageous, provided that the increased surface area does not lead to fouling issues. A design that is based on passive mixing is chosen in the present study. The selection of the specific setup is discussed in the following sections.

Depending on the mixing concept, different hydrodynamic profiles result, which may be characterized by the extent of spatial inhomogeneities and by varying velocities during crystal collisions, for example with a stirrer. This type of crystal collision is usually of high energy impact. Good mixing results in a homogeneous profile of the state variables of interest. Hence, mixing affects all crystallization phenomena, especially breakage, aggregation, and nucleation. Nucleation, growth, and dissolution may also be influenced by local differences in supersaturation. In general, when narrow product CSDs are intended during crystal growth, good mixing is desired, but crystal collisions shall be avoided.

2.3 Mode of Operation

There are three modes of operation for crystallizers: batch, fed batch, and continuous. Batch crystallizers are flexible and simple to clean. Therefore, they are applied for multipurpose crystallizers. They are preferred for difficult materials that are prone to encrustation or have high viscosities. Batch crystallizers are used when small amounts of product are required, because of low capital investments and process development costs. Lewis et al. (2015) state that they are more economical for $1\,\mathrm{m}^3$ of product per day and less and for up to $5 \times 10^6\,\mathrm{kg}$ per year. For a production of up to $20 \times 10^6\,\mathrm{kg}$ per year, they are economically comparable to other crystallizers; hence, batch crystallizers are also applied in this range. They are used for expensive substances since the amount of off-spec product is low, but down times lead to quality variations. The product CSDs are narrow.

Fed batch crystallizers, which are also called semi batch crystallizers, offer similar features as batch crystallizers. They are designed to deal with strong heat effects, or to prevent the formation of by-products. Continuous crystallizers are operated in fed batch mode during dynamic periods: the start-up and the shut-down phase of a process.

Continuous crystallizers are operated at steady state where they deliver constant product quality. They have fewer down times than batch crystallizers. Hence, they are applied in continuous process chains. In those, containment risks, resulting from the further transport of the product suspension to a downstream process, are decreased. Continuous crystallizers are operated at a desired supersaturation, so that small nucleation rates can often be realized. The operation and labor costs are low, compared with batch crystallizers. Small amounts of products cause small flow rates and require small pipe diameters to realize high velocities and to prevent sedimentation. Consequently, continuous crystallizers are applied for large scale production. Lewis et al. (2015) mention that continuous crystallizers are not economical below a production of $5 \times 10^4\,\mathrm{kg}$ per day. Consequently,

they are applied to at least 5×10^6 kg per year and they are preferable from an economic point of view above 20×10^6 kg per year.

2.4 Types of Ideal Continuous Crystallizers

There are two ideal models for continuous crystallizers, namely the plug flow (PF) and the MSMPR crystallizer. The MSMPR model is based on complete mixing. The attributes of the suspension in the crystallizer are identical to those of the exit stream. Hence, the product withdrawal is unclassified and the RTD and the CSD are broad. The PF assumes complete radial, but no longitudinal, mixing. Therefore, the RTD is the narrowest of all continuous crystallizers. In practice, back mixing occurs and the RTD of the PF model widens as shown in Fig. 2.1 (solid dark line) in which τ is the mean RT of a pulse tracer, thus of the suspension. The CSD of an ideal PF is narrow and comparable to that of a batch (Hohmann et al., 2018). The batch and steady state PF description match when the batch time variable is exchanged by the axial PF coordinate. Compared with the MSMPR, the PF has a higher space-time yield (Hohmann et al., 2016a).

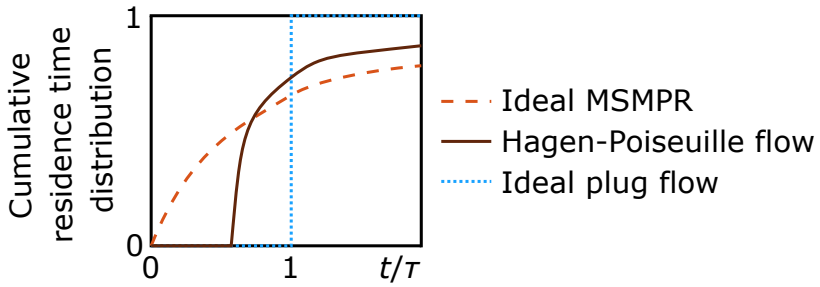

Figure 2.1: A scheme of the cumulative RT for a liquid pulse tracer for an ideal MSMPR, for an ideal plug flow, and for a Hagen-Poiseuille flow through an annular pipe.

2.5 Implementations of Continuous Crystallizers

Some crystallizer implementations approximate the continuous crystallizer models. In small-scale processes, MSMPR is often approached by strongly stirred crystallizers. The stirring leads to secondary nucleation, which may increase the width of the CSD, but may act as self-seeding and lead to a constant product CSD (Hohmann et al., 2018). There are designs that deviate from the MSMPR principle to reach narrower distributions. These setups separate the RT of mother liquor and crystals to influence yield and size. One example for such a separation is the classified product withdrawal (Tavare, 1995). MSMPR crystallizers are approximated by the main continuous industrial crystallizers, namely the circulation, the draft tube baffled, and the fluidized bed crystallizer. Devices approximating PF allow higher heat transfer rates than a batch or a single mixed suspension mixed product removal crystallizer (MSMPRC) due to higher surface-to-volume ratios. Hence, temperature and saturation can be adjusted faster. The PF model can be approximated by a series of MSMPRCs. For implementation the number of MSMPRCs is practically and economically limited (Hohmann et al., 2018). PF can also be approximated by a Couette flow device, an oscillatory baffled crystallizer, a Kenics static mixer, and by tubes.

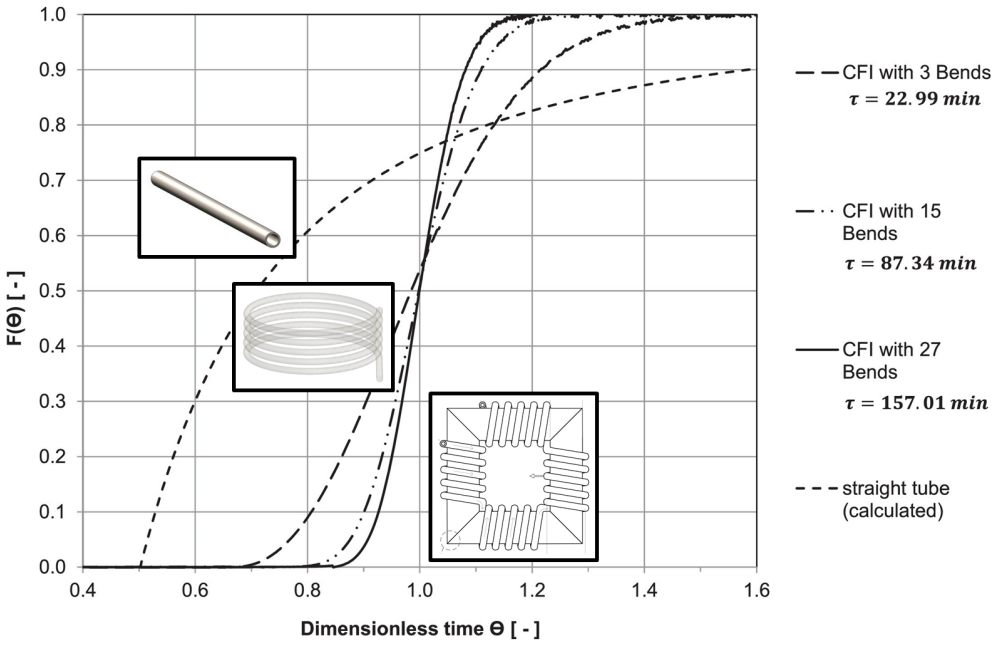

Figure 2.2: A scheme of the cumulative fluid residence time distribution in different tubes for an inner tube diameter d of 3×10^{-3} m, a coil tube diameter d_c of 6.3×10^{-2} m, a volume flow rate of 5.0×10^{-5} m^3 s^{-1}, and a Reynolds number Re of 24. The residence time distribution of a helically coiled flow tube is expected to lay between those of a straight tube and a coiled flow inverter.

Source: Reprinted with permission from Klutz et al. (2015), Copyright 2015, with permission from Elsevier. Modifications: Exemplary images of setups added.

It was discussed in Section 2.2 that passive mixers are advantageous regarding the design demands. Considering passive mixers, tubes offer the advantage of avoiding large surface areas and air bubble trapping resulting from additional internal structures. As passive mixers there are straight tubes, HCTs, and CFIs. Their typical fluid RTDs are shown in Fig. 2.2. Passive radial mixing increases with coiling and results in increased heat and mass transfer without requiring additional external energy. The fluid RTD width decreases from the straight tube to the HCT to the CFI. A narrow fluid RTD curve also indicates good radial mixing and low axial dispersion for particles. According to Koutsky and Adler (1964), back mixing is significantly reduced compared with straight tubes for Reynolds numbers from $Re \approx 300$ or $Re \approx 400$ to $Re \approx 3000$, but always remains below that of a straight tube. The flow in CFIs has been studied especially in liquid systems in several reports by Nigam. One of the first studies was published by Saxena and Nigam (1984). The parabolic laminar flow profile of straight tubes leads to broad RTDs. For a better mixing in turbulent flow, long straight tubes are required which leads to an increased loss of pressure. In helical coils, a secondary flow appears, which increases radial mixing and narrows the RTD (Castelain and Legentilhomme, 2006). Helical coils are compact, easy to fabricate and operate, and scale up is possible (Klutz et al., 2015). The CFI has the narrowest RTD of the coiled tubes providing long RTs. The CFI is built from bent HCTs. The bends change the direction of the centrifugal force, for which 90°-bends are optimal for mixing. This can be explained as follows. Behind a bend, the cross-sectional region of highest axial velocity becomes the area of the lowest axial velocity and vice versa (Klutz et al., 2015). The mean solid RT equals the mean fluid RT in

a CFI and the CSD of a batch crystallizer can be approached (Hohmann et al., 2018). To realize long RTs, long tubes are required or low Reynolds numbers can be applied, as long as sufficient fluidization is maintained. Special implementations exist to narrow the RTD, e.g., two liquid phases. However, this variation leads to longer tubes and scale-up issues (Hohmann et al., 2016a). For all PF implementations, the axial temperature control is challenging, and multiple thermostats may be required. Settling and, subsequently, clogging issues may occur.

There is a variety of curved tube geometries, which were reviewed by Vashisth et al. (2008), e.g., spiral tubes (Figueiredo and Raimundo, 1996) and chaotic tubes (Castelain and Legentilhomme, 2006). Helically coiled flow tubes provide narrow RTs and offer the advantage of passive mixing. The CFI is superior to the HCT regarding mixing, but the HCT is the basic unit of the CFI and should, therefore, be characterized.

2.6 The HCT

Compared with straight tubes, a radial fluid velocity appears in curved tubes. The characteristics of the fluid flow field in HCTs are explained in the following section. Typical dimensionless numbers, setup features, and operation modes that characterize a HCT are given with reference to literature applying HCTs in crystallization.

Fluid Flow Field and Dean Vortices

The flow field in the HCT is characterized by a secondary flow. Dean (1927) has shown analytically that a double vortex, which was later called "Dean vortex", develops in curved tubes. Adler (1934) and others extended the theoretical investigation of Dean for higher Re that were still below Re_{critical}. The extent of the secondary flow can be described by the Dean number. The Dean number is proportional to the Reynolds number and inversely proportional to the curvature ratio. Literature on the influence of curvature on secondary flow, pressure loss, and further transport processes was reviewed by Jokiel and Sundmacher (2019). For low Dean numbers, the fluid flow profile equals that of a straight tube. For increasing Dean numbers, the maximum axial velocity is shifted towards the outer side of the coiled tube (Vashisth et al., 2008).

A large number of simulations of the fluid flow in different geometries of curved tubes was performed by Nigam and co-workers (Kumar and Nigam, 2005; Mridha and Nigam, 2008; Saxena and Nigam, 1983; Singh et al., 2013; Vashisth and Nigam, 2009) and also by Palazoglu and Sandeep (2001). For one of the HCT setups that are investigated in the present study, the fluid flow was simulated by Wiedmeyer et al. (2017a). A direct numerical simulation of the fluid flow was carried out for two coils with 1 259 520 tetrahedral mesh cells as shown in Fig. 2.3. The resulting flow field is shown in Fig. 2.4a. As described by Vashisth et al. (2008), a higher velocity was observed in main flow direction at the outer wall and a Dean vortex developed. There is some instationarity in time in the fluid flow according to Fig. 2.4b,c, while the vortices stabilize the flow. The non-zero radial fluid velocity with its characteristic vortices is also referred to as "secondary flow". It enhances the radial mixing of the fluid at laminar flow regimes compared with straight tubes, and decreases the axial dispersion along the tube (Kurt et al., 2015). When particles are exposed to this flow field, it is expected that very small particles might easily follow the secondary flow. Large particles might stay in areas of higher axial velocity.

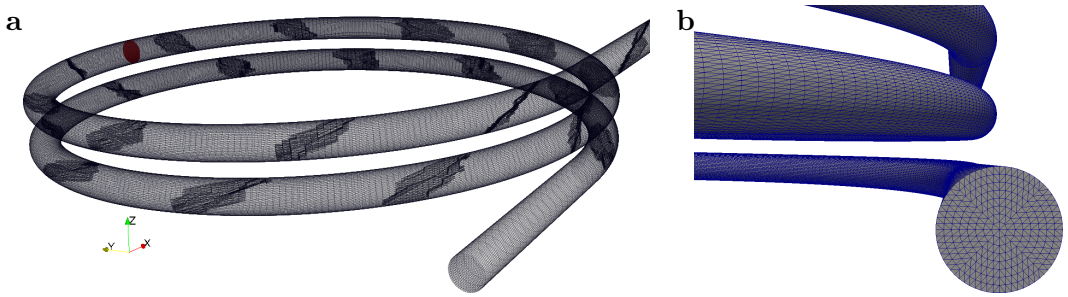

Figure 2.3: Geometry and mesh of two coils for the fluid flow field simulation. (a) A cross sectional slice is marked in red (top left) at half of the length of the second coil where the flow field is investigated; (b) magnified view of the tetrahedral mesh at the inlet.

Source: Reprinted with permission from Wiedmeyer et al. (2017a). Copyright 2017 American Chemical Society.

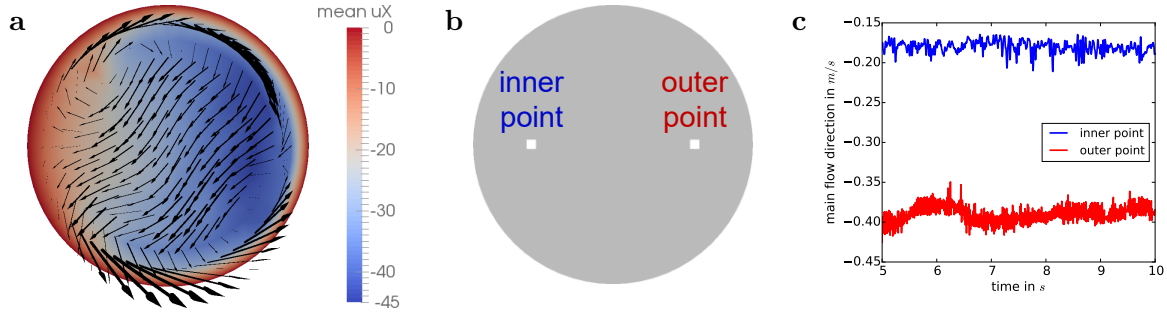

Figure 2.4: Velocity profile at the cross section that was marked in Figure 2.3 at half the length of the second coil. Forward axial flow is in the negative direction. The profile was calculated for an inner tube diameter d of 6×10^{-3} m, a distance p between two coil turns of 9×10^{-3} m, a coil tube diameter d_c of 114.5×10^{-3} m, a Reynolds number Re of 1280, and a Dean number De of 293. (a) Fluid flow field averaged over time in the cross section. The outer coil wall is at the right-hand side of the cross section. Color shows the temporal mean of the axial velocity in cm s^{-1}, arrows show the cross-sectional velocity; (b) cross section with two marked points; (c) temporal evolution of the axial velocity at the points marked in part b of this figure.

Source: Adapted with permission from Wiedmeyer et al. (2017a). Copyright 2017 American Chemical Society.

Spherical and food particles in HCTs were investigated experimentally by Chakrabandhu and Singh (2006); Palazoglu and Sandeep (2004); Sandeep et al. (1997) and theoretically and numerically by Cheng et al. (2005); Sandeep et al. (2000); Tiwari et al. (2006). All in all, the fluid RTD in HCTs is well studied. Some research on solid-liquid flow has been performed. Here, the solid-liquid investigation of spherical particles is experimentally extended by angular crystals.

Characteristic Dimensionless Quantities

A HCT configuration can be described by measures that are depicted in Figure 2.5. The

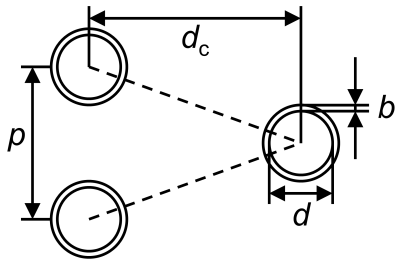

Figure 2.5: Scheme of measures of an HCT setup at the tube cross sections for a full coil with pitch p.

diameter d is the inner diameter of the tube and b describes the tube wall thickness. The pitch p and the coil diameter d_c are the vertical and horizontal distance from tube center to tube center where the pitch describes the height of one full coil.

The following scaled variables typically characterize the geometry of the setup and its transport properties

$$\lambda = \frac{d_c}{d}$$
$$P = \frac{p}{\pi d_c}$$
$$Re = \frac{d v_f \rho_f}{\eta_f}$$
$$De = \frac{Re}{\sqrt{\lambda}}$$
$$t_c = \frac{P}{Re}$$

where λ is the curvature ratio (Vashisth et al., 2008), P is the dimensionless pitch (Jokiel and Sundmacher, 2019), Re is the Reynolds number, De is the Dean number, and t_c is the torsion parameter (Hohmann et al., 2016a; Saxena and Nigam, 1983). The Reynolds number characterizes the flow conditions, where v_f is the average fluid velocity, ρ_f is the fluid density, and η_f is the dynamic viscosity of the fluid. Different correlations are available for the Dean number where the given one is used, e.g., by Adler (1934). Additionally, the Bodenstein number can be used to estimate the dispersion (Jokiel and Sundmacher, 2019) as performed by Klutz et al. (2015); Kurt et al. (2015) for CFIs for $Re \leq 150$. Further, the Stokes number St describes how a particle responds when the fluid flow field changes.

According to Vashisth et al. (2008), curvature affects the critical velocity and stabilizes the flow. They state that the secondary flow and mixing increase with decreasing curvature. The critical Reynolds number Re_{critical} in HCTs exceeds that of straight tubes since the secondary flow stabilizes the flow field. Re_{critical} is inversely proportional to the curvature ratio λ. Vashisth et al. (2008) give an overview of correlations from literature to calculate the critical Reynolds number indicating the transition from laminar to turbulent flow. They recommend among others the correlation of Kubair and Varrier (1961)

$$Re_{\text{critical}} = 12730\lambda^{-0.32} \tag{2.1}$$

for $10 < \lambda < 2000$ and that of Schmidt (1967)

$$Re_{\text{critical}} = 2300\left(1 + 8.6\lambda^{-0.45}\right)$$

for $\lambda < 200$, which is also suggested by Gnielinski (2013).

Helically Coiled Flow Tubes in Crystallization

Coiled tubes are traditionally used as heat exchangers. In chemical reaction engineering, coiled tubes have been proposed since the 1950s because of their good mixing properties (Jokiel and Sundmacher, 2019). Jokiel and Sundmacher (2019) give examples for the industrial use of coiled tubes in liquid-phase polymerization, virus deactivation, multiphase reactions, and crystallization.

Llano-Restrepo (2005) worked with a vertical continuous cooling crystallizer, which is a tower where only the cooling was realized by horizontal coils. Vashisth et al. (2008) reviewed the application of curved geometries in industry but do not mention crystallization applications. Since then, research on curved tubes for crystallization has been reported. Exemplary studies are cited below to introduce common setups and operation modes of HCTs, but it is not intended to give a complete review of all reports on crystallization in HCTs.

Khinast and co-workers (Besenhard et al., 2014a,b, 2015, 2017; Eder et al., 2010, 2011, 2012; Neugebauer and Khinast, 2015; Neugebauer et al., 2018) have investigated pharmaceutical substances and applied growth and dissolution cycles to dissolve fine particles experimentally and by modeling. Kockmann and colleagues (Bittorf et al., 2019; Hohmann et al., 2016a,b, 2018, 2019) studied the influence of dimensionless numbers and, hence, the coil design on the flow with a focus on CFIs. Sundmacher and colleagues (Wiedmeyer et al., 2017a,b) characterized the RTD in HCTs in the laminar regime and its effect on the CSD during growth. Further reports relate to seeding (Furuta et al., 2016; Rimez et al., 2019) and clogging (Chen et al., 2015).

Apart from the previously mentioned characteristic numbers, the setups may vary in further features, among which one is the coil orientation. Eder et al. (2011) crystallized in HCTs of vertical and horizontal orientations and, for their conditions, the orientation had no influence on the segregation and similar product qualities were achieved. Hohmann et al. (2018) mention that horizontal coils may be advantageous in reaching similar crystal and slurry RTs. Here, horizontal setups are applied to reduce the risk of settling of crystals in the lower part of coils.

Cooling of the tubes can be implemented by different approaches, e.g., one (Wiedmeyer et al., 2017a) or multiple (Neugebauer et al., 2018) baths, cooling with pressurized gas in an enclosure box (Hohmann et al., 2016a), tube-in-tube cooling, and segmented jackets. Here, water cooling is applied and two setups with a cooling bath as well as a setup with a double jacket for all coils are presented.

Combinations of particles and wall materials were reviewed by Hohmann et al. (2016a) for different tubes. Chen et al. (2015) reported that particle deposition was independent of the tube materials in their HCT setup.

Regarding the operation, Hohmann et al. (2018) state that spontaneous nucleation must be avoided by seeding or by inducing primary nucleation. Hohmann et al. (2016a) observed fast clogging during unseeded operation whereas Rimez et al. (2019) performed unseeded crystallization and invoked spontaneous nucleation in an HCT. Eder et al. (2012) used ultrasound in coiled tubes to generate seed crystals, before further growing

them in coiled tubes. Frequently, seeded cooling crystallization is performed to enable controlled crystallization (Bittorf et al., 2019; Hohmann et al., 2018; Neugebauer et al., 2018; Wiedmeyer et al., 2017a,b). The present study also applies seeded crystallization.

The number of fluid phases may exceed a single continuous phase. Two-phase segmented flow with air was realized by Eder et al. (2012); Hohmann et al. (2018); Neugebauer et al. (2018). The creation of stable bubbles may be tedious, but offers the advantage of good mixing within the slugs and uniform RTs. Liquid-liquid flows are also possible, but require an additional separation step. The present dissertation deals with one continuous phase.

Furthermore, all HCT-setups may be prone to non-ideal effects to a certain degree. Fouling may occur for some substances, and may lead to the necessity of regular cleaning of tubes. Fouling is discussed in Section 3.2. Strong supersaturation at cold tube walls should be avoided to prevent crystal growth on the walls. Although high cooling rates can be achieved compared with large vessels, the speed of cooling via surface area is finite. As discussed in Section 2.5, the mixing in HCTs deviates from plug-flow. Spatial variations in fluid concentration or in particle concentration may occur.

3 Residence Time Experiments in Straight Tubes

An aim of this study is to produce narrow CSDs continuously. The RT of crystals determines their time for crystal growth and therefore the crystal size. In the continuous PF model, perfect radial mixing, but no back mixing are assumed such that all crystals have the same RT. Hence, widening of the CSD is avoided. To obtain large crystals, the RT must be sufficiently high. PF is often associated with a tube. For tubes, the RT can be manipulated by the tube length and the crystal velocity, of which the latter is controlled by the fluid flow rate. In practice, the length of a straight tube is limited. To achieve RTs that are sufficient for crystallization at a limited tube length, the fluid flow rate can be reduced, but fluid flow in the laminar and transient flow regime deviates from the ideal PF and the RT of the crystals is distributed. This chapter investigates experimentally whether the mixing in an implemented straight tube setup is still close to PF and sufficient for crystallization.

The questions to be answered in this chapter:

1. Is the RTD of glass beads in the applied tube narrow?
2. Is the RT of glass beads equal to the mean fluid RT?
3. Is there a qualitative difference in the RTD for flow rates in the laminar and transient flow region?
4. Is there a difference in the RT for particles of varying size?
5. Do particles of varying size affect each other's RTs?
6. Does the wall material affect the RTD of the particles? If yes, how?
7. Is the mixing in the tube sufficient for crystallization experiments?

3.1 Setup and Procedure

The main part of the setup is a straight horizontal tube. The tube is located on the discharge side of a peristaltic pump (PD 5206 SP vario, Heidolph) as illustrated in Figure 3.1. There is a three-way valve between the pump and the tube for glass bead addition. The third nozzle is filled with glass beads and closed with a plug. For particle addition, the third inlet is opened. At the end of the tube, the suspension is imaged by a flow-through video microscope (QICPIC/R02, Sympatec). The cuvette of the microscope is located 0.4 m above the tube level. The total tube length, measured from the three-way valve to the cuvette of the microscope, is 20.5 m. It consists of two parts, a straight section of

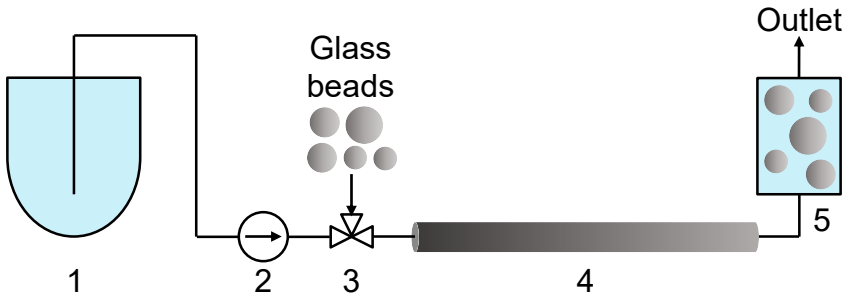

Figure 3.1: Piping and instrumentation diagram of the straight tube setup: 1 water reservoir, 2 peristaltic pump, 3 three-way cock, 4 straight tube, 5 cuvette of the flow-through microscope.

20 m length and an inclined section of 0.5 m length, which are connected by a hose coupling made of polyethylen. The last 0.5 m of the tube consist of silicone and this section inclines towards the level of the cuvette. It was not observed visually through the tube walls that beads sediment in this section or get slower. For the first straight part of the tube, two different tube materials are used, either silicone or glass. In case of silicone, the straight tube is made of a single piece. The straight part of the glass setup consists of several pieces of straight glass tubes of approximately 1.4 m length. They are connected by hollow silicone tubes wrapped around connecting glass tubes. The connectors are of a few centimeters length and a diameter that equals that of the glass tubes. Both setups are of the same total length. All tubes have the same radius of 2.5×10^{-3} m.

In the experiments, double-distilled water at room temperature is continuously pumped through the system. Two different pump speeds, called low and high, are applied. The measured mass flow rates are $(7.1 \pm 0.1) \times 10^{-3}\,\mathrm{kg\,s^{-1}}$ and $(10.9 \pm 0.2) \times 10^{-3}\,\mathrm{kg\,s^{-1}}$ for the silicone tube and $(7.2 \pm 0.2) \times 10^{-3}\,\mathrm{kg\,s^{-1}}$ and $(11.0 \pm 0.2) \times 10^{-3}\,\mathrm{kg\,s^{-1}}$ for the glass tube. For mass flow rates of $7.2 \times 10^{-3}\,\mathrm{kg\,s^{-1}}$ and $11 \times 10^{-3}\,\mathrm{kg\,s^{-1}}$, for the given tube radius, and for water at room temperature, the resulting Reynolds numbers are $Re = 1830$ and $Re = 2796$. Hence, the lower mass flow rate is in the laminar region whereas the higher mass flow rate is in the transition region, according to the discussion on Re_{critical} in Section 2.6.

A RT measurement starts when the glass beads are added. An amount of 0.1 g to 0.4 g of three different glass bead fractions of sizes 100 µm to 200 µm, 200 µm to 300 µm, 300 µm to 400 µm, and a mix thereof is applied. The glass beads (Silibeads type S, Sigmund Lindner) are spherical and have a density of $2500\,\mathrm{kg\,m^{-3}}$. Their density is 2.5 times higher than that of the fluid.

Imaging

The flow-through microscope records binary videos with 20 frames per second and their image resolution is 2048 pixel × 2048 pixel for a field of view of 0.005 m × 0.005 m. The 2D projections of the glass beads are recorded when they pass the window of the flow-through cell, which has an optical path length of 0.002 m. The postprocessing of the images includes a background subtraction, a single object identification, and an object quantification, for example to determine the sphere equivalent diameter of each projected glass bead. The image post processing is based on algorithms that were reported previously (Borchert and Sundmacher, 2011; Eisenschmidt, 2018).

3.2 Experimental Results

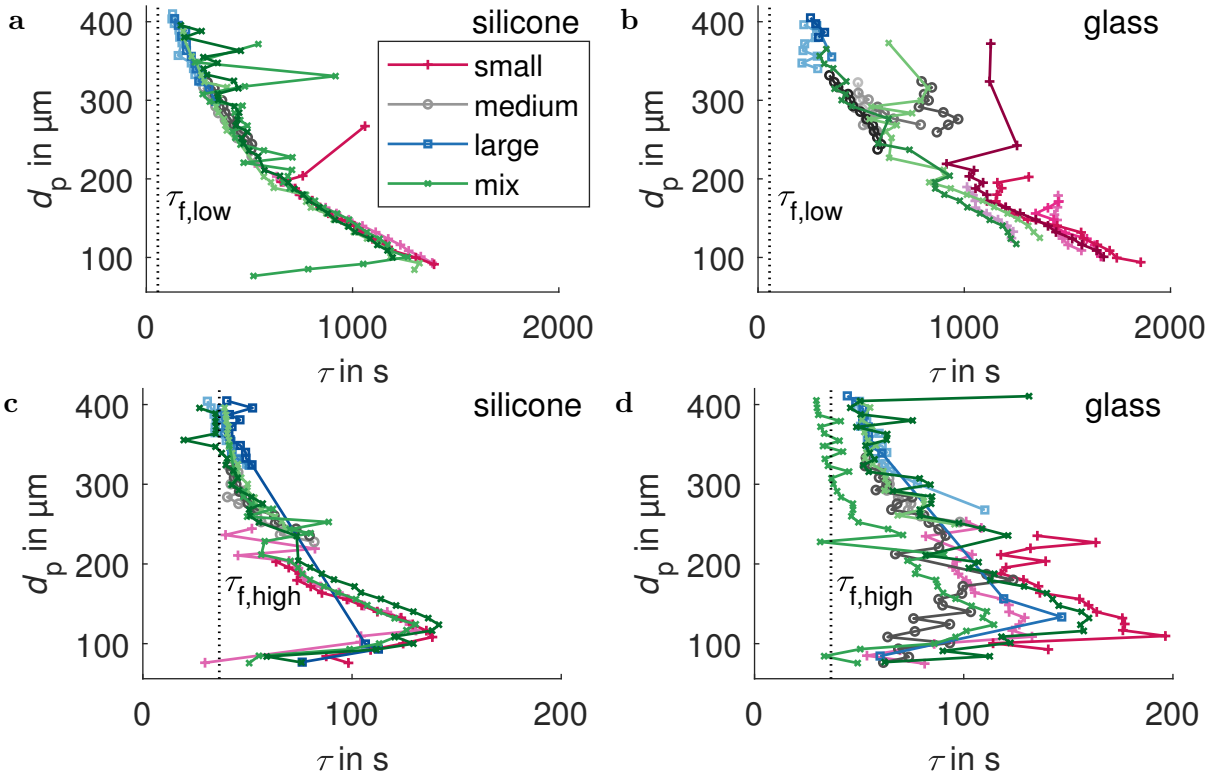

Figure 3.2: Average RT of glass beads of varying sphere diameter d_p (solid curve, markers shown for class widths of 8 µm) for several experiments with a small (magenta), medium (gray), large (blue), and mixed (green) size fraction and average fluid RT (dotted, black). Straight tubes consist of (a,c) silicone or (b,d) glass. Experiments at (a,b) low or (c,d) high average fluid mass flow with average fluid RT $\tau_{f,low/high}$.

The results of the RT experiments are shown in Figure 3.2. Regarding the first three questions of this chapter, there are the following findings. At the high fluid flow rate, the particle RTD varies from 0.5 to 5 times the average fluid RT (see Figure 3.2c,d). The particle RTD is broader at the low fluid flow rate where it varies from 6 to 33 times the average fluid RT (see Figure 3.2a,b). Hence, the RTD of the glass beads is broad in the straight tubes, where most particles are slower than the fluid. For transient flow, the mean fluid RT agrees with the RT of the large glass beads as depicted in Figure 3.2c,d. For laminar flow, the mean fluid RT is nearly 60 s, and it is considerably lower than that of the fastest glass beads as shown in Figure 3.2a,b. For laminar flow, the smallest investigated glass beads are the slowest. Whereas for transient fluid flow, 120 µm glass beads have the highest RT. Glass beads that are even smaller approach the RT of the fluid. Very small glass beads might be small enough to follow the fluid flow, and may thus approach the fluid velocity.

In Figure 3.2a,b, for the mass flow rate in the laminar region, the largest glass beads of 400 µm size have a RT of approximately 140 s in the silicone tube, and of approximately 250 s in the glass tube. The smallest glass beads have a considerably longer RT of approximately 1300 s in the silicone tube, and of approximately 1600 s in the glass tube. For transient flow in Figure 3.2c,d, the large glass beads have a RT of approximately 40 s, and

they are again faster than the small glass beads, with a RT of up to approximately 150 s.

The RT of particles of varying size, which is the focus of the fourth question, has also been reported. Baptista et al. (1996b) experimentally investigated single particles in a slightly inclined horizontal tube, with particles of a density which was 6 % or 42 % higher than that of the fluid. They also observed larger RTs for smaller particles, which they contributed to a smaller drag force for small particles compared with large ones. Additionally, they found that larger particles roll more than small ones. Furthermore, the particle rotation became more important for larger particles and for particles of higher density. Baptista's observations considering the RT dissimilarity of particles according to their size can be confirmed, here, in a setup with slightly higher density differences and for a particle collective.

Segré and Silberberg (1961) carried out experiments that analyzed the radial particle location in the tube. Their setup consisted of a straight vertical tube with particles of the same density as the fluid. At sufficiently high velocities, further down the tube, they observed a tubular pinch effect, where particles arrange in a certain radius in the tube. They found that the emergence of the effect is among others proportional to the particle-to-tube radius. Hence, the pinch effect might lead to a size-dependent particle RT. The Segré–Silberberg effect cannot explain the (same) behavior in the horizontal setup in the present dissertation. Here, gravity plays an important role because the particle density is considerably higher than that of the fluid, consequently, the particles sediment quickly. Whereas in a vertical tube, the particles accumulate at a certain tube radius in the cross section, which causes the RT effects.

A comparison of the RT of glass beads in a mix of size fractions and in separate experiments in Figure 3.2 shows that the RT is not affected when small and large glass beads are mixed.

Now, the sixth question is addressed. Considering the wall material, for transient flow, the RTs are similar in the glass and in the silicone tube (compare Figure 3.2a,c with Figure 3.2b,d). For laminar flow, the glass beads are slightly slower in the glass tube. At both flow rates, larger variations in the RTD are visible in the glass tube. This might be a result of the glass tube connections. Some glass beads may be trapped in the gap before they come free and reenter the main flow, or beads may be disturbed in their flow by the glass tube edges. Apart from these variations, no difference in the qualitative RT profile is observed between the tube materials.

From a practical perspective, the fabrication and geometrical stability of a long tube of a fixed bent geometry may be challenging. Flexible silicone tubes may be moved unintentionally, but silicone is cheap, very flexible in geometry, and less fragile than glass. Singh et al. (2013) use polyvinyl chloride for the tubing of a CFI. This material has a limited flexibility after fabrication, but it is transparent, stable, and cheap and can therefore also be considered as suitable wall material. They mention that during fabrication of polyvinyl chloride tubes, rough walls should be prevented. This holds for all wall materials. In general, smooth walls should be applied to prevent fouling. Bent glass tubes are fragile, but glass might be advantageous when inert tubing is required for food, biochemistry or pharmaceutical applications. Further, glass is transparent, which allows crystal observation and a wide temperature operating regime. Another option are metal tubes because metal constructions are less fragile and sensitive to deformation. Kazi et al. (2012) compared the deposition of calcium sulphate on different metals and found that fouling increases with the surface roughness and with the thermal conductivity of the metal, where stainless steel has shown the least fouling. For microbial biofilms, Hyde

et al. (1997) observed that stainless steel developed the most tenacious biofilms among their materials. Removal became easier from stainless steel to polypropylene, glass, and new fluorinated polymers. This is confirmed by the studies of Ferguson et al. (2013). They found stronger fouling on the stainless steel construction of their probes than on the quartz vessel walls. In a preliminary setup of the present study, blocking was frequently observed and may have been caused by metal temperature sensors that were introduced by T-type connectors. One reason may be that the metal sensors acted as cold bridges.

Care is necessary when implementing connectors. They should not have a larger diameter than the tubes, to prevent sedimentation and fouling. Connectors of smaller diameters are unproblematic because they are short and their overall effect on the RT is negligible. In any case, dead zones in front of, or behind, connectors should be prevented. Especially for glass constructions, connections are difficult to produce with a constant diameter everywhere. Sections of varying connector or tube diameters may appear or be used intentionally. When wider tubes are used, higher fluid mass flow rates are required to stay in the same laminar region.

The observations and discussions are summarized to respond to the last question. Overall, the RTD is very broad in the laminar region, and still rather broad in the transient region. For laminar flow, the small glass beads stay six to nine times longer in the tube than the large ones. For transient flow, they stay up to four times longer in the tube. Thus, mixing in the straight tube setup is far from plug flow. The current setup and operation conditions are not suited for crystallization experiments, because the RTD is very broad. A further increase of the fluid flow rate towards turbulent flow rates might improve the mixing but would decrease the mean particle RT. Longer tubes are required for higher RT, but the tube length is limited for practical reasons, for example limited space, and an increase in pressure loss. For materials with strong growth rates, which lead to significant growth in the time scale of seconds, sufficient crystallization would be possible. Another option to extend the tube, in spite of limited space, is a bent geometry. A well-defined compact crystallizer may be realized by helical coils. Further, helical coils may also improve the mixing, and by that means, narrow the RTD of the particles as discussed in Section 2.5.

4 Residence Time and Crystallization Experiments in the HCT

Figure 2.4 in Chapter 2 has shown that a complex flow profile with secondary flow develops in HCTs. These simulations were carried out for the fluid phase. In the present chapter, the influence of the profile on solid crystals is investigated by experiments. This chapter demonstrates that crystal growth can be realized in the novel HCT crystallizer. The aim is to grow crystals of a narrow size distribution by cooling crystallization. Narrow product CSDs may be desired for downstream processing in process chains, for example for solid-liquid separation during filtration, and for an improved flowability of the product.

The same questions are answered as in Chapter 3. Additional questions regarding the RTD and crystal growth are given below.

The new questions to be answered in this chapter are:

1. How well does the fluid approach PF?
2. How does the upward or downward flow direction affect the RTD?
3. How does cooling affect crystal growth?
4. Does the seed mass affect the concentration during crystal growth?
5. Do nucleation, aggregation, breakage or growth rate dispersion occur?
6. Is the product CSD narrow?

Before the results of crystal growth experiments are shown, the appearing phenomena are investigated separately. The HCT is characterized in view of fluid RTD, crystal RTD, and potential for crystal growth. Practical advice is given for the implementation of an HCT crystallizer, and for crystallization experiments in the HCT.

4.1 Experimental Materials and Size Estimation

Potash Alum

Potassium aluminium sulphate dodecahydrate ($KAl(SO_4)_2 \cdot 12H_2O$) with the trivial name potash alum (Merck CAS No. 7784-24-9, purity $\geq 99\,\%$) was used for all experiments. For the solution, potash alum was dissolved in deionized water (LaboStar 2-UV, Evoqua). The initial CSD was analyzed in 86 wt % ethanol. Potash alum is nearly insoluble in ethanol (Mullin and Sipek, 1981). Hence, it is used to measure the seed CSD in the tube because a change of the CSD might affect the RTD.

Imaging

Potash alum crystals have a compact shape. Their description by one size coordinate, for example a sphere equivalent diameter, should be sufficient to describe the size of potash alum. The sphere equivalent diameter can be calculated from the projection of a crystal in an image, by estimating the diameter of a circle of the same projection area. The estimated size coordinate can be applied to calculate the crystal volume. To improve the accuracy of the estimation of the crystal volume, the 3D crystal shape is reconstructed from 2D projections as depicted in Figure 4.1, assuming that all crystals are perfectly symmetric octahedra. Potash alum predominantly crystallizes as an octahedron, where the faces have a {111} Miller index, under the chosen conditions (Buckley, 1930). Faces corresponding to the cube {100} and the rhombic-dodecahedron {110} may also appear, but only to a slight extent. Hence, the crystal shape of potash alum can be characterized by the perpendicular distance h from the crystal center to an octahedral face as illustrated in Figure 4.1.

The same imaging algorithms are applied, as was explained in Chapter 3.1. The images are binarized by background subtraction. For grayscale videos with a frame rate of 10 images per second, a thresholding is necessary for the binarization. Additional steps appear for shape reconstruction. The boundary of the identified objects is extracted. The objects are quantified and their 3D shape is estimated via a database comparison as described by Borchert et al. (2014). The database was generated with octahedral crystals. An object is categorized as aggregate when its solidity is below 0.9, where the solidity is the ratio of the projection area of an object to the area of the convex hull of the object (Ferreira and Rasband, 2012). An object that is not classified as aggregate is classified as bubble when its elliptic eccentricity (Zeidler, 2013) is smaller than 0.3, otherwise it is categorized as primary crystal. Small objects that consist only of a few pixels cannot be reliably assigned to one of these categories, instead they are classified as nuclei when their sphere equivalent diameter d_p is below 50 µm.

When the perpendicular distance h is used as size coordinate, the univariate description of potash alum can easily be extended for bivariate or multivariate substances where two or more different face types are present. In the shape estimation algorithms, the database has to be replaced for the corresponding substance.

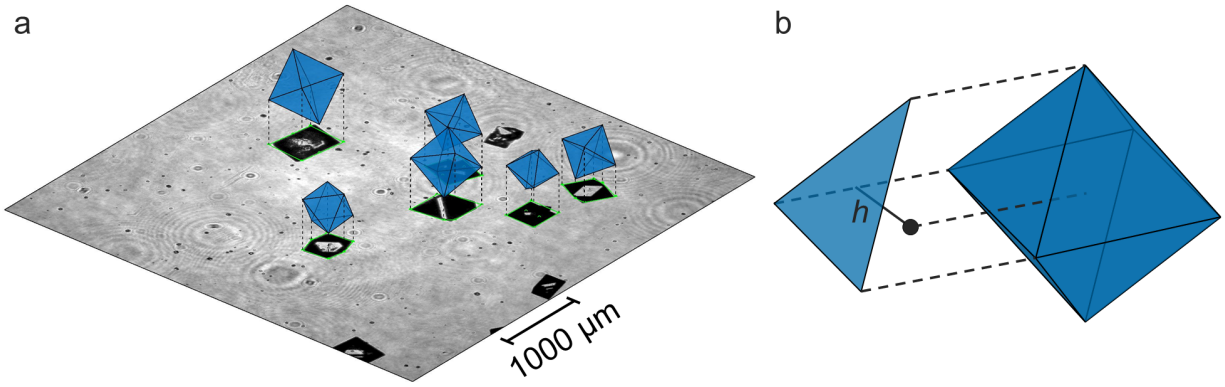

Figure 4.1: (a) Potash alum crystal projections; (b) an ideal octahedral potash alum crystal with its perpendicular face distance h.

Seed Crystal Generation

For the crystallization experiments in the HCT, similar material parameters are chosen as in the straight tube. In both cases, the particle density is larger than that of the fluid. Here, the particle-to-fluid density ratio is 1.6 whereas it was 2.5 for the glass beads in the straight tube. As in the straight tube experiments, the crystal size is in the µm range. The seed crystals were sieved for 60 min to 75 min with a vibratory sieve shaker (AS 200 control, Retsch). Less than 1×10^{-4} kg of crystals were seeded at once. The chosen mesh sizes were 150 µm, 200 µm, 212 µm, 300 µm and 400 µm. The resulting fractions are labeled A to D in Figure 4.2. The initial size fractions were measured in preliminary experiments in the antisolvent ethanol. Additional small crystals are observed at perpendicular face distances below 50 µm. Hence, they are categorized as nuclei in the postprocessing image algorithms when they are smaller than 50 µm.

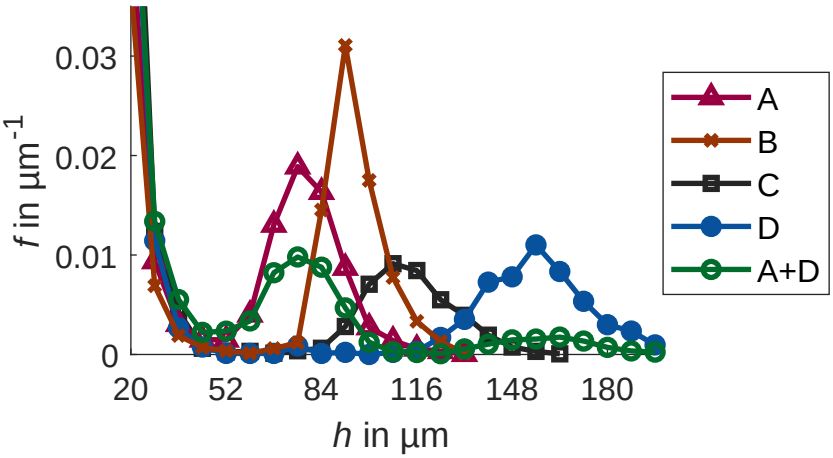

Figure 4.2: Number density distribution f over crystal size h of potash alum seed crystal fractions of varying sieve size, measured in the antisolvent ethanol for separate fractions of increasing mesh sizes and for a mix of the smallest and the largest fraction. The particle number density is calculated for bins of 8 µm width in h. Mean bin sizes are shown for selected size classes for visibility.

Source: Adapted with permission from Wiedmeyer et al. (2017a). Copyright 2017 American Chemical Society.

Sieving may cause defects in a crystals' surface and structure. The sieved material is not perfectly spherical and deviations from the mesh size limit are anticipated. Defects may cause growth rate dispersion. Small abraded crystals may attach to the surface of larger crystals during sieving and cause initial breeding in experiments. Deviations in the initial CSD may occur because the bulk crystal material may be heterogeneously distributed in the storage container.

Saturation Concentration

Supersaturation and supercooling are expressed using the driving force for crystallization. In this study, the "solution concentration" (Mullin, 2001) is formulated as a mass fraction. The mass fraction w is expressed as the ratio between the mass of dissolved hydrate m_{hyd} and the mass of added water $m_{\mathrm{w,added}}$ via

$$w = \frac{m_{\mathrm{hyd}}}{m_{\mathrm{w,added}}} \tag{4.1}$$

which can be easily calculated from the solution which was prepared for the experiments. At a given temperature T, w_{sat} is the equilibrium saturation. The applied empirical correlation (Kovačević et al., 2017) for the saturation concentration w_{sat} in kg of dissolved hydrate to kg of added water is

$$w_{\text{sat}} = 0.180 \times 10^{-3} T^2 - 0.102726 T + 14.7607 \tag{4.2}$$

where T is the temperature in K. The correlation in Eq. (4.2) is based on measurements from 293 K to 323 K. Some experiments that are presented in this chapter are simulated in Chapter 6. For the simulations, various kinetics from literature are tested. For the kinetics that were parameterized by Temmel et al. (2016) also their solubility is used, which is

$$w_{\text{sat}} = 4.86 \times 10^{-8} \vartheta^4 - 2.43 \times 10^{-6} \vartheta^3 + 7.76 \times 10^{-5} \vartheta^2 + 2.3 \times 10^{-3} \vartheta + 0.0506 \tag{4.3}$$

where ϑ is the temperature in °C.

The absolute supersaturation, which is also called relative supersaturation, is

$$\sigma = \frac{w - w_{\text{sat}}}{w_{\text{sat}}} \tag{4.4}$$

4.2 Experimental Setups and Procedures

4.2.1 Setups

For the HCT setup, a geometry similar to that of the straight tube is chosen. The inner tube diameter is identical or similar with 0.005 m to 0.006 m. The tubes of the HCT incline only slightly because of coiling and are still nearly horizontal. Hence, the pitch, which was introduced in Figure 2.5, is low. The tube length can be increased for crystal growth because there are no spatial limitations, but it is kept in a comparable range and it is approximately one and a half times the straight tube length. All peripheral tubes consist of polysiloxane such as also applied for one of the straight tubes.

A schematic of the experimental setup is depicted in Figure 4.3. The solution for the experiments is prepared in a 5 L-vessel (position 1), which is equipped with a jacket for heating, with a diagonal four-blade stirrer operated at a speed of 200 rpm, which corresponds to a tip speed of 0.73 m s^{-1}, and with a platinum resistance thermometer (PT100).

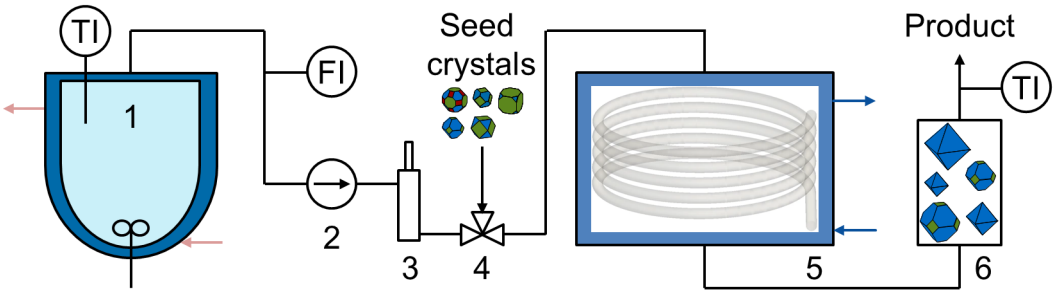

Figure 4.3: Piping and instrumentation diagram of the HCT crystallizer setup with temperature sensors (TI) and mass flow rate sensor (FI): 1 reservoir for solution, 2 gear pump, 3 debubbler, 4 three-way cock, 5 HCT, 6 cuvette of the flow-through microscope.

A gear pump (4030-280-DM, Scherzinger Pump Technology) sucks in the solution that passes a Coriolis type mass flow sensor (CORI-FLOW, Bronkhorst, position 2). The pump is followed by a degasifier (position 3), which is typically filled with a volume of $3 \times 10^{-5}\,\mathrm{m}^3$ solution to remove air bubbles. A three-way valve (position 4) serves to add the seed crystals. The suspension enters the HCT (position 5). The product suspension that leaves the HCT passes the cuvette of a video flow-through microscope (position 6). The microscope serves to measure the RT of the crystals and their dimensions to reconstruct the CSD. Behind the cuvette, there is a type K thermocouple. The limiting deviation of the type K thermocouple is $\pm 1.5\,\mathrm{K}$, whereas that of the aforementioned platinum resistance thermometer is $\pm 0.5\,\mathrm{K}$. Throughout this study, temperatures are given with higher accuracy to illustrate relative differences in temperature.

In a pilot setup, several type K thermocouples were introduced into the HCT with T-shaped tube connectors. This construction led to frequent blocking of the setup. The metallic sensors probably became cold bridges where material crystallized. Hence, in the setup shown in Fig 4.3, temperature sensors were only applied in the reservoir and near the tube outlet, where potential large crystals would not be trapped and grow within the setup. Similarly, the concentration measurement along the tube is difficult. Consequently, only small suspension densities were applied, to avoid strong changes in the concentration along the tube.

For the HCT (position 5), three configurations were investigated, which are depicted in Figure 4.4. The setup in part a of Figure 4.4 has a compact design and the smallest height. The HCT in part b serves to compare upward and downward flow. Both HCT setups are composed of silicone tubes whereas the HCT in part c consists of glass, to compare wall effects. All configurations have a vertical coil axis and can be operated with upward or downward flow. In upward flow, the inlet is at the bottom of the vertical HCT. Hence, a change in flow mode leads to changes in the lengths of the tubes connecting the HCT to the adjacent experimental equipment. The relevant lengths are given in Table 4.1.

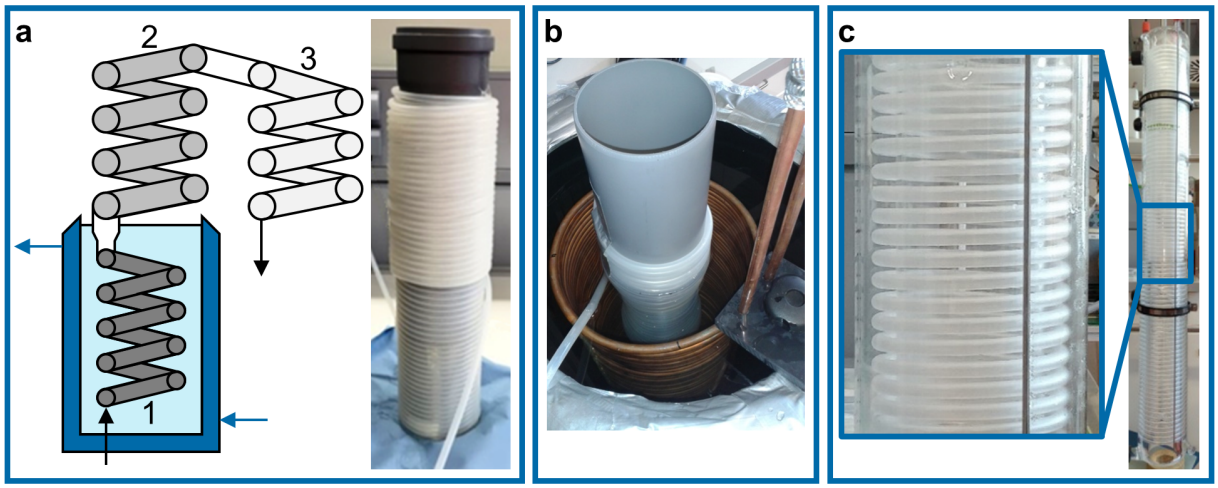

Figure 4.4: Different setups for the HCT in Figure 4.3. (a) Setup with silicone tubing coiled up and down (Wiedmeyer et al., 2017b); (b) setup with silicone tubing coiled up in a cooling bath (Wiedmeyer et al., 2017a); (c) photograph of the jacketed glass HCT with enlarged view.

Source: (a) Reprinted with permission from Wiedmeyer et al. (2017b). Copyright 2017 Wiley-VCH. Modification: parts of the figure were moved, printed in color; (b) reprinted with permission from Wiedmeyer et al. (2017a). Copyright 2017 American Chemical Society.

The first HCT configuration is illustrated in Figure 4.4a. For this configuration, the degasifier (position 3) had not yet been installed. Experiments in Section 4.3.1 led to the recommendation of using a degasifier. Consequently, it was introduced for the other configurations. The tube in this setup can be divided in three parts. The first part is coiled upward around a cylindrical pipe from its bottom. This part is inside a cooling bath during the process. The second part is attached to the first tube with a tube connector. It is further coiled upward until the top of the cylinder is reached. The tube is then again coiled down on top of the coiled tubes of the second part, which creates the third tube part. The tube material is polysiloxane.

The second HCT configuration is created by a single tube that is coiled upward on a cylindrical pipe. The tube material is again polysiloxane. The cylindrical pipe is immersed in a barrel. The barrel with a volume of 200 L is filled with water, such that the whole HCT is submerged in the water. The barrel is isolated with rock wool and aluminum, and with floating pellets on the water surface. Inside the barrel there is a copper helix with a diameter of 0.24 m, which serves as cooling coil. The cylindrical pipe, on which the crystallizer tubes are located, is perforated to improve the heat exchange. Air bubbles enter the water barrel from the bottom, to increase the mixing of the cooling water, and to supply a homogeneous temperature profile in all heights of the barrel. During operation, the temperature difference in the barrel is 1 K with a higher temperature at the top.

The third HCT configuration is a jacketed glass helix (Gebr. Rettberg GmbH). Including the jacket, the glass setup has a height of 1.2 m whereby the HCT has a height of 1.13 m. Three platinum resistance thermometers (PT100) are located in a 120° distance in the jacket. They are located in three different heights −0.01 m, 0.53 m, and 1.02 m, where the center of the lowermost coil at the inlet is used as reference height, and is assumed to have a height of 0 m. The cooling water in the jacket is supplied from the bottom and leaves the jacket at the top. The peripheral tubes are connected to the glass construction by a glass adapter with olive tubing connectors (Gebr. Rettberg GmbH).

The values of the geometric measures of the three configurations according to Figure 2.5 are given in Table 4.1. The values indicate that the setups are of similar dimension, and they are the basis for dimensionless numbers that are typically used to characterize HCT setups. The dimensionless numbers are given in Section 4.2.3, and may serve for a comparison to HCTs at a different scale.

4.2.2 Procedures

A batch-wise operation is suited to characterize the setup in terms of crystal RT. Hence, all experiments were performed in batch mode. First, the fluid RT and its dispersion were investigated. Second, the RT of the dispersed phase was measured and, third, growth experiments were conducted. Continuously seeded experiments were not performed. In order to seed continuously, a change in the experimental setup is required, and wet seeding should be applied instead of dry seeding. The RTD should not be affected significantly by a switch to continuous seeding, but the increase in crystal size during crystal growth may change depending on the fluid to crystal residence time ratio. Later on, in Chapter 6, a model of the process is developed and the performed batch-seeded experiments are simulated. Additionally, continuously seeded processes are predicted via simulations.

Table 4.1: Dimensions of the coiled tubes in the setups shown in Figure 4.4. The tube length l is measured from position 4 to position 6 in Figure 4.3. The coil diameter d_c is measured at the tube center. For Figure 4.4a, dimensions are given for the three successive tube sections (Wiedmeyer et al., 2017b).

	Figure 4.4a			Figure 4.4b	Figure 4.4c
Dimension	Section 1	Section 2	Section 3		
$l_{4-5,up}$ in m		0.9		2.0	1.2
$l_{4-5,down}$ in m		-		1.3	1.2
l_c in m	7.1	13	10.4	29	32
$l_{5-6,up}$ in m		1.6		2.8	1.4
$l_{5-6,down}$ in m		-		3.8	1.4
d in m	0.005	0.006	0.006	0.006	0.006
d_c in m	0.118	0.119	0.127	0.115	0.114
w in m	0.0015	0.0015	0.0015	0.0015	0.0015
p in m	0.008	0.009	0.009	0.009	0.013
height in m	0.15	0.31	0.23	0.73	1.13

Fluid Phase Experiments

The average mass flow rates of the low and high pump rate were determined by weighing measurements for 30 s to 120 s. The fluid flow in the HCT deviates from PF, due to hydrodynamic dispersion. Hence, deviations from the average RT appear for the fluid elements. The resulting fluid RT distributions were measured by flow tracer experiments in the absence of particles.

Here, the tracer was a pulse of potash alum solution. The setup in Figure 4.3 was modified, such that the reservoir at position 1 was filled with water and that the inlet was equipped with a three-way valve to connect a second reservoir containing the tracer solution. During the tracer test, water was continuously pumped through the system. For the test, the inlet was switched for the initial 15 s from water to a potash alum solution. A conductivity probe (FYA641LFP1, Ahlborn) was located at position 6 where the size of the product crystals would usually be measured. This position is named "outlet". The conductivity probe had a small probe volume of $2.7 \times 10^{-6}\,\mathrm{m}^3$, which increases the RT of fluid elements in the probe, and slightly broadens the measured tracer signal. Furthermore, the measured axial dispersion resulting from the growth section of the tube between positions 4 and 6 is increased by the first tube section between positions 1 and 4, and again the real axial dispersion is actually smaller than the measured one. The offset RT was measured in additional conductivity measurements at position 4. This position is referred to as the "inlet". The distance from the tube inlet in the vessel at position 1 to the seed crystal valve at position 4 was measured. This distance was added when the average fluid RT τ_f was determined from Coriolis-type mass flow measurements. The experiments were conducted representatively for upward and downward flow in the HCT of setup b. In the upward experiments, the degasifier had not yet been installed.

The water and solution temperature varied between 295 K and 300 K but were corrected for by the automatic temperature compensation of the conductivity probe. The solution was prepared at least one day before the measurements, to provide sufficient time for dissolution and re-cooling to room temperature. The initial mass fraction w of the tracer was (0.07 ± 0.01) kg of hydrate/kg of added water where the conductivity κ is at the

upper end of the measurement range of the conductivity probe ($0.001\,\mathrm{S\,m^{-1}}$ to $2\,\mathrm{S\,m^{-1}}$) with a value of $(1.7 \pm 0.1)\,\mathrm{S\,m^{-1}}$. A change in the conductivity of the solution was caused by the tracer. The correlation between conductivity and mass fraction was measured in additional experiments in the same temperature range. The resulting second-order polynomial least squares fit for the conductivity κ in $\mathrm{S\,m^{-1}}$ with a variance of $0.004\,\mathrm{S^2\,m^{-2}}$ is

$$\kappa = 3.6w - 150w^2$$

where w is given in kilograms of hydrate per kilograms of added water.

Particle Phase Experiments

In the previous experiments to characterize the RT of the liquid phase, the fluid was a potash alum solution in water at a low concentration at room temperature. To measure the RT of the crystal phase, a potash alum solution of similar concentration and temperature as in the following growth experiments is used to create comparable conditions. The growth experiments will be performed in a temperature range of 303 K to 313 K. For this range, the density and the dynamic viscosity of the potash alum solution are only 10 % and 29 % higher than that of water, and hence, comparable to the experiments described in the previous section. To avoid growth and dissolution, the RT experiments are performed at saturation concentration at isothermal conditions. Apart from the applied temperature profile, the experimental procedures for the RT measurements and for the growth experiments of the crystal phase are the same. As in the characterization experiments for the fluid RT, low and high mass flow rates are applied. For each setup, RT and growth experiments are shown. An overview of the experiments is given in Table 4.2.

For a growth experiment, 5 L of solution were prepared in the reservoir (position 1), heated until all crystals were dissolved and cooled to 1 K to 2 K above the saturation temperature, to keep all crystals dissolved. Before each set of experiments, the HCT was cleaned with water. Although the water in the HCT was removed with pressurized air, some water remained in the tubes. The water amounted to a few percent of the reservoir content. When the prepared solution was pumped from the vessel through the system, the initial concentration reduced slightly because of the remaining water. Hence, three samples were taken from the reservoir during each experiment and air dried for several days to measure the actual concentration of the solution. The saturation temperature was between 38 °C and 40 °C. The saturation temperature is illustrated schematically by the starting point of the trajectory on the right-hand side in Figure 4.5. The solution was sucked by the pump (position 2 as depicted in Figure 4.3) at one of two different flow rates called “low” and “high”. The corresponding mass flow rates were $(7.5 \pm 0.3)\,\mathrm{g\,s^{-1}}$ and $(10.9 \pm 0.3)\,\mathrm{g\,s^{-1}}$. For practical reasons, the product suspension was recycled into the storage vessel (position 1). As there was only a small amount of crystals in the experiments, the influence on the concentration in the reservoir was negligible.

Before the start of an experiment, the solution was pumped through the system until the temperature in the reservoir and behind the HCT were in steady state. While the solution was pumped to the three-way valve (position 4), it cooled down slightly, as shown schematically in Figure 4.5, by the movement of the trajectory at a constant concentration to lower temperatures. An experiment started when dry seed crystals were added within less than 10 s. The seed mass was measured prior to its addition, and it was in the range of $1 \times 10^{-4}\,\mathrm{kg}$ to $3 \times 10^{-4}\,\mathrm{kg}$. For seed addition, the third nozzle of the valve was turned upward, filled with seed crystals, sealed with a plug, and it was opened to be flushed for

Table 4.2: Overview of experiments for which the RT distributions are shown visually in Section 4.3. Seed fractions according to Figure 4.2. All crystal RT figures are based on several experiments over the whole range of seed size fractions except for setup c at downward flow and a low mass flow rate. ϑ_{sat} and σ_{out} refer to the initial conditions where σ_{out} applies at the outlet before crystallization. Arabic letters in brackets indicate the part of the figure.

Type of experiment	Setup	Seed fraction	Experimental details (no. of experiments, mass flow rate, continuous phase characteristics, flow direction, no. of observed crystals)	Figure
fluid RT	b	-	low down; low up; high down; high up	4.6
crystal RT	a	several	(a) low, 5389; (b) high, 3292	4.8
crystal RT	b	several	(a) low, up, 4278; (b) high, up, 3807; (c) low, down, 1921; (d) high, down, 3035	4.9
crystal RT	c	(c) B; (a,b,d) several	(a) low, up, 3502; (b) high, up, 5719; (c) low, down, 112; (d) high, down, 1029	4.10
crystal growth	c	A	all up, ϑ_{sat} =40 °C; (a) low, σ_{out} =4 %, 148; (b) low, σ_{out} =4 %, 169; (c) high, σ_{out} =2 %, 1117; (d) high, σ_{out} =4 %, 1312	4.11
crystal growth	a	A	all low, ϑ_{sat} =40 °C; (a) σ_{out} =4 %, 1185; (b) σ_{out} =14 %, 1788; (c) σ_{out} =19 %, 2208	4.12
crystal growth	b	A+D	all low, up, ϑ_{sat} =41 °C; (a) σ_{out} =1 %, 859; (b) σ_{out} =10 %, 941; (c) σ_{out} =14 %, 827	4.13

the seed addition. Afterwards, the third nozzle was closed again and rinsed with water. The volume of the nozzle was $1.1 \times 10^{-6}\,m^3$. The plug took up $0.3 \times 10^{-6}\,m^3$ of the nozzle volume. During seeding, air could enter the system, but the nozzle volume amounted only to approximately 0.1 % of the HCT volume.

The suspension cooled down in the HCT (position 5). In the HCT, the concentration of the continuous phase decreased by crystal growth. The point of time when the seed crystals passed the flow-through microscope (position 6) after seed addition at the three-way valve was the RT τ_p of the crystals. The outlet suspension temperature was measured directly behind the cuvette of the flow-through microscope. At the HCT outlet, the suspension temperature reached its lowest value. The jacket temperature of the HCT should not fall below a minimum value to keep the suspension in the metastable zone during the whole process and to prevent nucleation. Barrett and Glennon (2002) identified the metastable zone of potash alum to be 4 K to 8 K wide. Hence, the suspension at the HCT outlet was at most 5 K colder than the saturation temperature.

The pulsation of the gear pump affects the RTD of the fluid. A high pulsation causes axial backmixing. The pulsation can be compared to that of a similar gear pump with a higher displacement (4030-450, Scherzinger Pump Technology). For water at 12.5 Hz

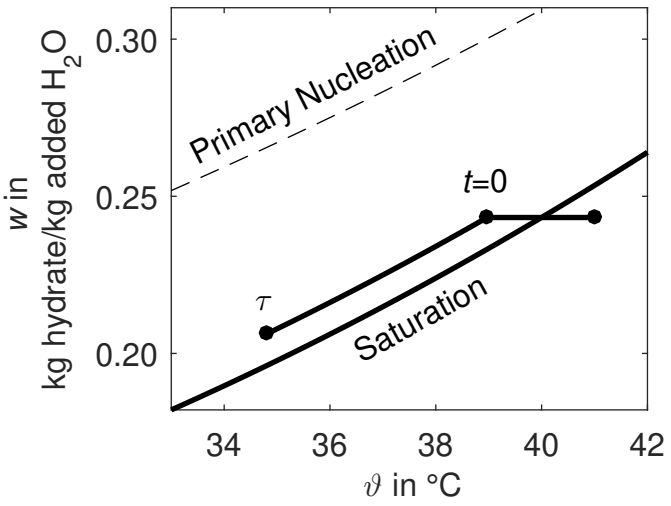

Figure 4.5: Scheme of the metastable zone width of potash alum. The central area is the metastable supersaturated zone where growth of crystals occurs, but primary nucleation is unlikely (Mullin, 2001). The inset of primary nucleation is adapted from Barrett and Glennon (2002) for a cooling rate of 0.7 K/min and illustrated by the upper supersolubility curve. An exemplary process route is depicted starting in the undersaturated region with a saturation concentration of 40 °C, cooling to 39 °C, addition of seed crystals and further cooling to 35 °C.

and 2×10^5 Pa, the peak amplitude in the 4030-450 model was 4×10^4 Pa. In further measurements at 2×10^5 Pa and 5×10^5 Pa, the peak amplitude was 20 % of the mean pressure. For these conditions, the pump speed was three times higher than that which was applied in the present dissertation with the 4030-280 model. For a decrease in pump speed, the pulsation increases. Hence, a considerable pulsation can be expected at the operation point in this study.

4.2.3 Dimensionless Quantities

Dimensionless numbers to classify an HCT setup and its flow were introduced in Section 2.6. The Reynolds number is based on material parameters. These parameters depend on the concentration and temperature of the solution. The fluid density of a potash alum water solution varies with the saturation temperature and the current temperature. Following Kubota et al. (1985), for a saturation temperature of 313.15 K and a process temperature from 309.15 K to 313.15 K, the fluid density ρ_f is from 1111 kg m^{-3} to 1094 kg m^{-3}. For a saturation temperature and current temperature of 313.15 K, the dynamic viscosity of the fluid η_f is 1.118×10^{-3} kg m^{-1} s^{-1} following Mullin et al. (1965) and 1.110×10^{-3} kg m^{-1} s^{-1} following Kubota et al. (1985). When the process temperature sinks to 309.15 K for a constant saturation temperature, the viscosity is 1.210×10^{-3} kg m^{-1} s^{-1} following Kubota et al. (1985). For the calculations, a constant intermediate value of 1.150×10^{-3} kg m^{-1} s^{-1} is assumed for the dynamic viscosity η_f, and a constant value of 1100 kg m^{-3} for the fluid density ρ_f. The resulting dimensionless numbers are listed in Table 4.3 for setup a and in Table 4.4 for the other two setups.

An increase in the mass flow rate leads to an increase in Reynolds number and Dean number and to a decrease in the torsion parameter. On the one hand, high Reynolds

Table 4.3: Dimensionless numbers for the setup in Figure 4.4a for the three tube sections and the given density, dynamic viscosity and mass flow rates of $7.5\,\mathrm{g\,s^{-1}}$ and $10.9\,\mathrm{g\,s^{-1}}$.

Symbol	Low mass flow rate			High mass flow rate		
	Section 1	Section 2	Section 3	Section 1	Section 2	Section 3
λ	24	20	21	24	20	21
P	0.0216	0.0241	0.0226	0.0216	0.0241	0.0226
Re	1661	1384	1384	2414	2011	2011
De	342	311	301	497	452	437
$t_c \times 10^4$	0.13	0.17	0.16	0.09	0.12	0.11

Table 4.4: Dimensionless numbers for the setup in Figure 4.4b,c for the given density, dynamic viscosity and low and high mass flow rates of $7.5\,\mathrm{g\,s^{-1}}$ and $10.9\,\mathrm{g\,s^{-1}}$.

Symbol	Setup in part b		Setup in part c	
	Low	High	Low	High
λ	19		19	
P	0.025		0.035	
Re	1384	2011	1384	2011
De	317	460	318	461
$t_c \times 10^4$	0.18	0.12	0.26	0.18

numbers are desired to achieve a good mixing. On the other hand, low Reynolds numbers decrease the necessary tube length to realize a desired minimum RT and to reach a required growth. For the low mass flow rate, the Reynolds number is 1384 for all tubes of 6 mm diameter and 1661 for the first section in the HCT setup a of 5 mm diameter. For the high mass flow rate, the Reynolds numbers are 2011 and 2414. Several correlations for the critical Reynolds number were given in Section 2.6. Among the correlations that were cited in the review of Vashisth et al. (2008), the lowest critical Reynolds number is reached with the correlation of Kubair and Varrier (1961), which was stated in Eq. (2.1). The lowest value is reached in the first section of the first setup, and it amounts to $Re_{\mathrm{critical}} = 4629$. Hence, all Reynolds numbers are in the laminar region. The tube of larger diameter is the main part in all of the setups. Thus, hereafter, only the corresponding Reynolds number is mentioned when differentiating between the two flow modes low and high.

For all setups, the curvature ratio λ is between 19 and 24. These ratios are similar to those in the setups of Redlinger-Pohn et al. (2016b); Vashisth and Nigam (2009). The dimensionless pitch is between 0.022 and 0.035. For the upper limit, the dimensionless pitch confirms the lower limit of the investigated values of the pitch in the setup of Vashisth and Nigam (2009). They found that a more complex asymmetrical flow profile develops for larger values of the dimensionless pitch. The Dean number is between 301 and 342 at the low Reynolds number and between 437 and 497 at the higher one. It is a measure for the strength of the secondary flow. Here, the values are above those of Klutz et al. (2015), in the range of those of Tiwari et al. (2006) and below those of Redlinger-Pohn et al. (2016b). The torsion is between 0.13×10^{-4} and 0.26×10^{-4} at the low Reynolds number and between 0.09×10^{-4} and 0.18×10^{-4} at the higher one. Following Saxena and Nigam (1984), the torsion has no significant effect on the RTD below a torsion of 10^{-3}. Another dimensionless expression is the particle diameter to tube diameter ratio. For

particles of a sphere equivalent diameter in the range of 50 µm to 500 µm, in a tube of a diameter of 0.005 m or 0.006 m, the ratio is between 0.8 % and 10 %. High ratios would increase the pressure gradient in the tube (Michaelides, 2006).

4.3 Experimental Results

4.3.1 Fluid Residence Time

The experimental setup and procedures to measure the fluid RT were described in Section 4.2.2. The results are depicted in Figure 4.6. As expected, the RT and the width of the RTD increase with decreasing Reynolds numbers in Figure 4.6. The average fluid RT from weighing and Coriolis mass flow measurements is located at the beginning of the tracer RT curves, but the average τ_f has still to be increased by the delay of the inlet signal. Then, the average τ_f may approach the peak of the tracer and it may still be located slightly before the peak of the tracer response. Comparing the inlet and outlet RTDs, the RTDs widen until they reach the outlet and the peak heights decrease. Consequently, there is axial fluid dispersion, which leads to deviations from PF, which is stronger for lower Reynolds numbers. There is an exception for the high mass flow rate in upward flow, where the peak height stays approximately constant. This exception can be explained by the missing degasifier. All curves belonging to the upward flow display fluctuations that were caused by air bubbles. The fluctuations increase with the Reynolds number, because the pump draws more air at higher pump speeds. As a result, the degasifier was installed for experiments in the next sections. For the inlet measurement at the high flow rate, strong fluctuations can be seen when the peak of the RTD is approached. At the same time, the inlet RTD is narrow. Hence, the peak of the inlet measurement is too low. Further comparing upward and downward flow highlights that the first tracer elements reach the inlet and outlet position at the same time. Nevertheless, the RTD curves at upward flow are narrower than those at downward flow. This behavior can be explained by the degasifier, in which a small volume of fluid collects and mixes. It is installed in downward flow and leads to a broadening of the RTD. The Coriolis average RTs for upward flow are higher and, thus, the mass flow in upward flow is slightly lower. This can be explained by an increased pressure loss in upward flow. The difference is small, and does not lead to a visible effect.

In setup b, the results for upward and downward flow were similar. Hence, considering the other setups, a small variation of the pitch should not have an impact on the fluid RT. Also, the other dimensions of the setups, such as tube and coil diameter and tube length, are similar and the same flow rates were applied. Consequently, the main difference is the wall material in setup c. It is not expected to significantly affect the liquid flow for the used material and flow rates.

Summing up, the fluid RTDs are similar for upward and downward flow. There is considerable axial dispersion for the lower Reynolds numbers and a small but still measurable axial dispersion for the higher Reynolds numbers. A degasifier should be installed, especially for high flow rates, to avoid air bubbles, and thus to reduce flow disturbances and axial dispersion.

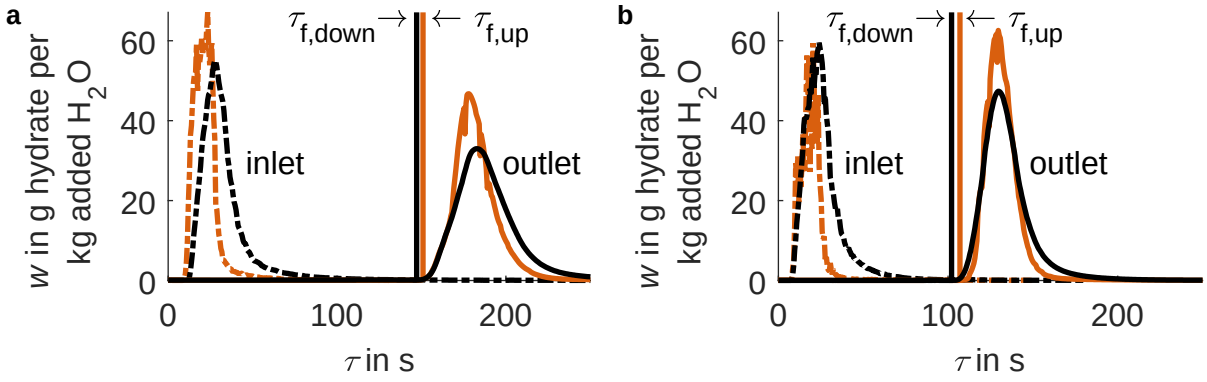

Figure 4.6: Tracer measurements indicating the fluid RT in the HCT setup in Figure 4.4b for low and high mass flow rates: (a) $Re_{\mathrm{up/down}} = 1534/1627$; (b) $Re_{\mathrm{up/down}} = 2163/2294$. Average RT as determined by the Coriolis-type mass flow sensor (vertical lines). Inlet signal, as measured at the seed addition position 4, and outlet signal, as measured at the cuvette position 6 in Figure 4.3.

Source: Adapted with permission from Wiedmeyer et al. (2017a). Copyright 2017 American Chemical Society.

4.3.2 Crystal Residence Time

This section characterizes the HCT in view of its crystal RTD before crystal growth is analyzed in the subsequent section. The results in this section serve to derive the potential of the HCT for crystal growth.

Hence, the structure of this section is as follows. First, it is verified that the saturation temperatures were met and that the CSDs remained constant in the experiments. Next, the experimental results are stated. The questions that were mentioned in the beginning of Chapter 4 and that relate to the RTD are answered, by stating which results were anticipated and, thirdly, the experimental results are discussed. Last, practical advice is derived for future experiments.

It is validated whether isothermal conditions were successfully realized by comparing the outlet CSDs from the isothermal experiments to the inlet CSDs for the crystal size fractions that were measured in ethanol. Figure 4.7 indicates that the outlet distributions are in the same crystal size range as the inlet distributions and that isothermal conditions were successfully reached. For the antisolvent and isothermal experiments that are shown in Figure 4.7, the ratio of the total number of aggregates to the total number of candidates was calculated for comparison to the growth experiments in the next section. Within each seed fraction, the aggregate to primary crystal ratio decreases with crystal size. As listed in Table 4.5, for the larger size fractions C and D, the aggregate ratios are especially

Table 4.5: Ratio of total number of aggregates to total number of candidates for the experiments in Figure 4.7 for all crystals with a sphere equivalent diameter between 50 µm to 500 µm. The aggregate ratios from the isothermal experiments were averaged.

Experiment type	Seed fraction				
	A	B	C	D	A+D
Ethanol	0.2	0.5	2.9	6.0	0.8
Isothermal	1.9	2.0	1.7	1.8	1.6

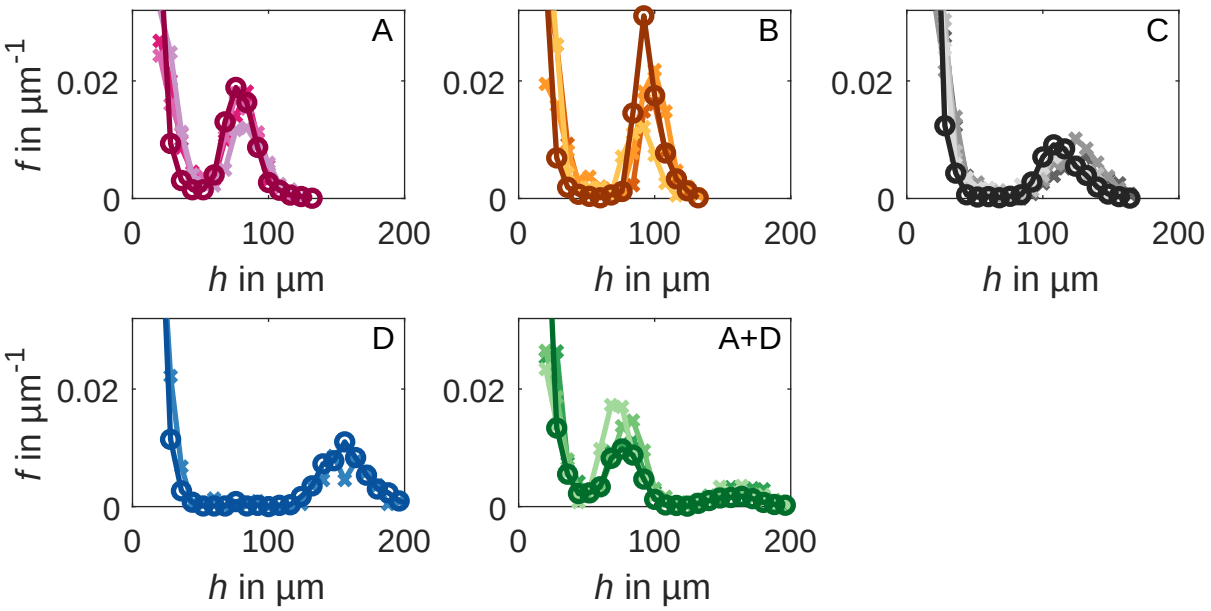

Figure 4.7: Number density distribution of potash alum seed crystal fractions of varying sieve size. Comparison of distributions measured in the antisolvent ethanol (darkest curve with circle markers) where the curves are identical to those in Figure 4.2 to those measured in isothermal experiments (cross markers, different colors for different experiments). The subfigure labels A, B, C, D, and A+D refer to the seed size fractions as labeled in Figure 4.2.

Source: Adapted with permission from Wiedmeyer et al. (2017a). Copyright 2017 American Chemical Society.

high for crystal sizes below 170 µm and 250 µm and lead to high ratios for the ethanol experiments. In the isothermal experiments, the ratios are approximately two for all size fractions. Some small dust crystals may aggregate in the isothermal experiments to form small aggregates. Nevertheless, the aggregation rate is low enough, such that the overall number distributions remain qualitatively identical to the antisolvent distributions.

The RTDs were determined with a kernel density estimator as explained by Wiedmeyer et al. (2017a). The experimental results for the three different HCT setups are shown in Figures 4.8, 4.9, and 4.10.

Comparing the crystal RT τ_p to the mean fluid RT τ_f in Figures 4.8b, 4.9b,d, and 4.10b,d, the crystal RT is in average one to three times higher than the fluid RT for the higher Reynolds number. For the lower Reynolds number in Figures 4.8a, 4.9a,c, and 4.10a,c, the deviation is larger and the crystals are in average three to six times slower than the fluid. When the liquid phase is faster than the dispersed phase, the crystals are fed with fresh solution of higher concentrations for a larger distance. This is advantageous because crystal growth is increased compared with identical RTs, i.e., shorter tube lengths are necessary to reach a desired final crystal size. The deviation in the fluid and crystal RTD may result from the density difference between both phases. Gravitation moves the crystals closer to the bottom tube wall, where the no-slip condition applies and, as a result, the crystals become slower than the fluid. It can be expected that this effect is stronger for a lower Reynolds number, in other words, for a decreasing fluid velocity and for higher crystal to fluid density ratios. Hence, low laminar Reynolds numbers should be avoided to prevent sedimentation.

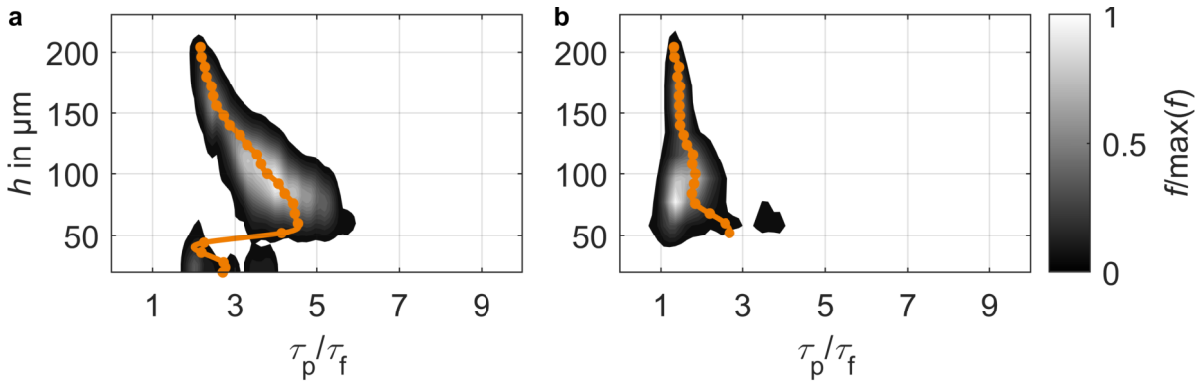

Figure 4.8: Normed number density distribution over RT ratio of crystals for experiments in the setup in Figure 4.4a. Mean RTs (orange markers) are shown for size classes with more than 10 crystals. (a) Low Reynolds number with $\tau_f = 117\,s$; (b) high Reynolds number with $\tau_f = 81\,s$.

Source: Reprinted with permission from Wiedmeyer et al. (2017b). Copyright 2017 Wiley-VCH. Modifications: mean value curves added, smaller crystals considered in the data, x-axis scaled by fluid residence time, limits of y-axis changed, and names of symbols adjusted.

For the fluid, the RTD widens from inlet to outlet, in Figure 4.6, by at least 23 % (high flow rate, downward flow) to maximum 92 % (high flow rate, upward flow). These values are based on the ratio of the width of the outlet to the inlet signal. The width is defined as the time period when a mass loading of at least 0.3 kg hydrate per kg added H_2O was detected. The RT difference between 90 % of the outlet signal and the inlet signal is 9 % to 13 % larger than the average τ_f. The crystal RTDs widen to a larger extent. Comparing the values when 90 % of the crystal mass leave the crystallizer, in Table 4.6, to the corresponding τ_f of 117 s, the RTs more than double and are 2.5 to 5.1 times higher than τ_f. The fluid RT experiments evince that there is axial dispersion, which might increase for the crystals.

Apart from the stretching towards larger RT ratios for the smaller Reynolds number, the RTDs look qualitatively similar for both Reynolds numbers. It can be expected that the distributions are similar because both Reynolds numbers are in the laminar region. The previously mentioned deviations can be anticipated as the mixing improves with an increasing Reynolds number.

There is a dissimilarity in the RT for crystals of varying size although no difference was expected. On the one hand, Section 4.3.1 demonstrated that there is a good mixing of the fluid. On the other hand, the crystals are slower than the fluid, which may be caused by the density difference between fluid and crystals. This may have different consequences for crystals of varying shape, size and thus mass. Similar observations were made by Redlinger-Pohn et al. (2016b) for elongated fibers where the mixing and τ_p increased for smaller fibers and by Sandeep et al. (1997) for buoyant spherical particles in a HCT. There, an increase in particle size led to a slight decrease in mean τ_p and a significant decrease in the minimum τ_p and standard deviation of τ_p. Other particle shapes that are less compact might align with the axial flow and might then travel less rapidly in radial direction, due to their hydrodynamic resistance. There, the size dependency is probably less strong, but it was also observed for elongated fibers (Redlinger-Pohn et al., 2016b). In the present study, the mean RT increased with decreasing crystal size and it reached a maximum between 60 µm and 120 µm. A reason might be that the secondary

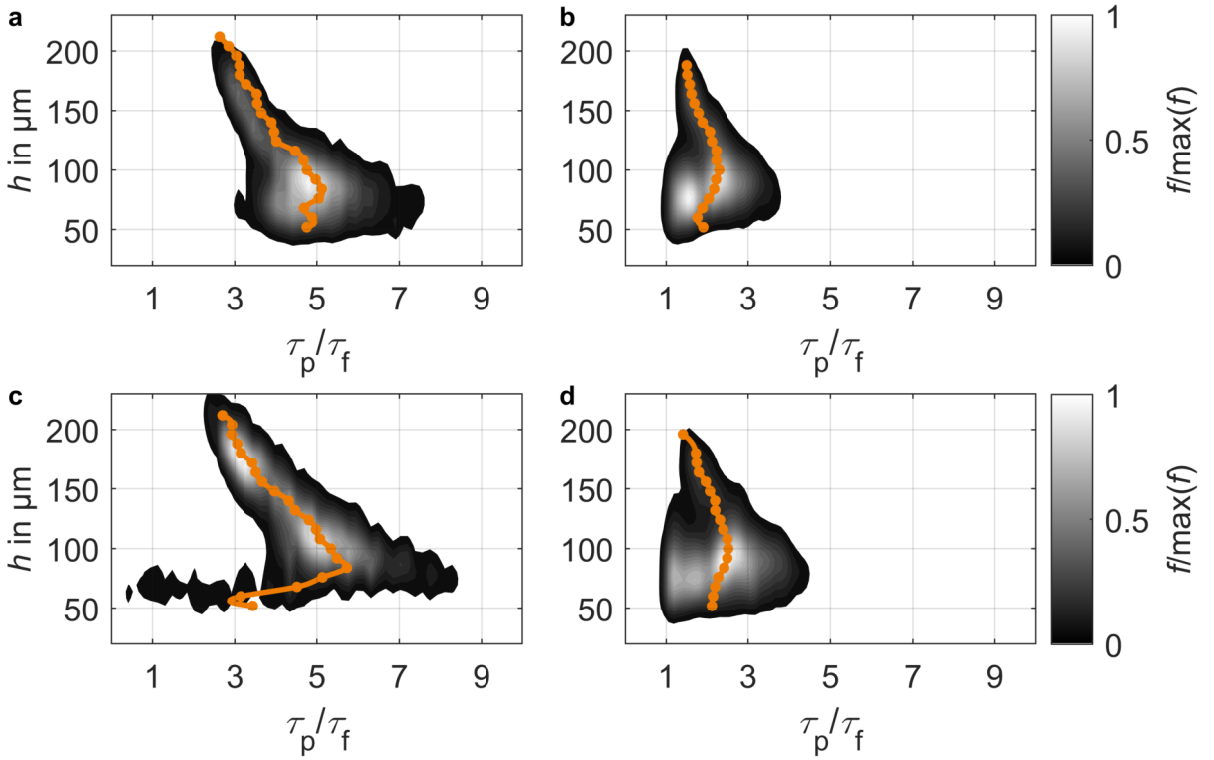

Figure 4.9: Normed number density distribution over RT ratio of crystals for experiments in the setup in Figure 4.4b. Mean RTs (orange markers) are shown for size classes with more than 10 crystals. (a,b) Upward flow; (c,d) downward flow; (a,c) low Reynolds number with $\tau_f = 141\,s$; (b,d) high Reynolds number with $\tau_f = 97\,s$.

Source: Adapted with permission from Wiedmeyer et al. (2017a). Copyright 2017 American Chemical Society.

flow moves the small crystals to regions of lower axial velocity, e.g., directly at the wall. Simulations for spherical particles in a setup of similar dimensionless numbers by Tiwari et al. (2006) demonstrated, indeed, that the particle-settling zone is at the inner bend of the horizontal helical tube. For even smaller sizes, the mean RT decreases again. The smallest crystals might easily follow the fluid flow and, thus, approach the fluid RT. In the figures, the standard deviation in RT exhibits a similar behavior as the mean RT and increases for small crystals. This observation can be confirmed by Tiwari et al. (2006) who observed in simulations that the secondary flow distributes particles in the HCT cross section especially for small particles. Small crystals might follow the secondary flow more easily and a wider RTD might be anticipated for the small crystals. For an increasing Reynolds number, the mixing increases and the RT of the small crystals approaches that of the large ones. Saxena and Nigam (1984) investigated curvatures that are slightly below those in the present dissertation. They found that a narrower RTD can be achieved when the curvature of the setup is increased. The Dean number is proportional to the Reynolds number and inversely proportional to the curvature. Hence, the uniformity of the RT can be improved by increasing the Dean number. This is confirmed by Sandeep et al. (1997); Tiwari et al. (2006) for setups of Dean numbers in the same range. It is expected that the influence of the size-dependent RT on the product CSD is very small in growth experiments for the high Reynolds number, and negligible when the Reynolds number is

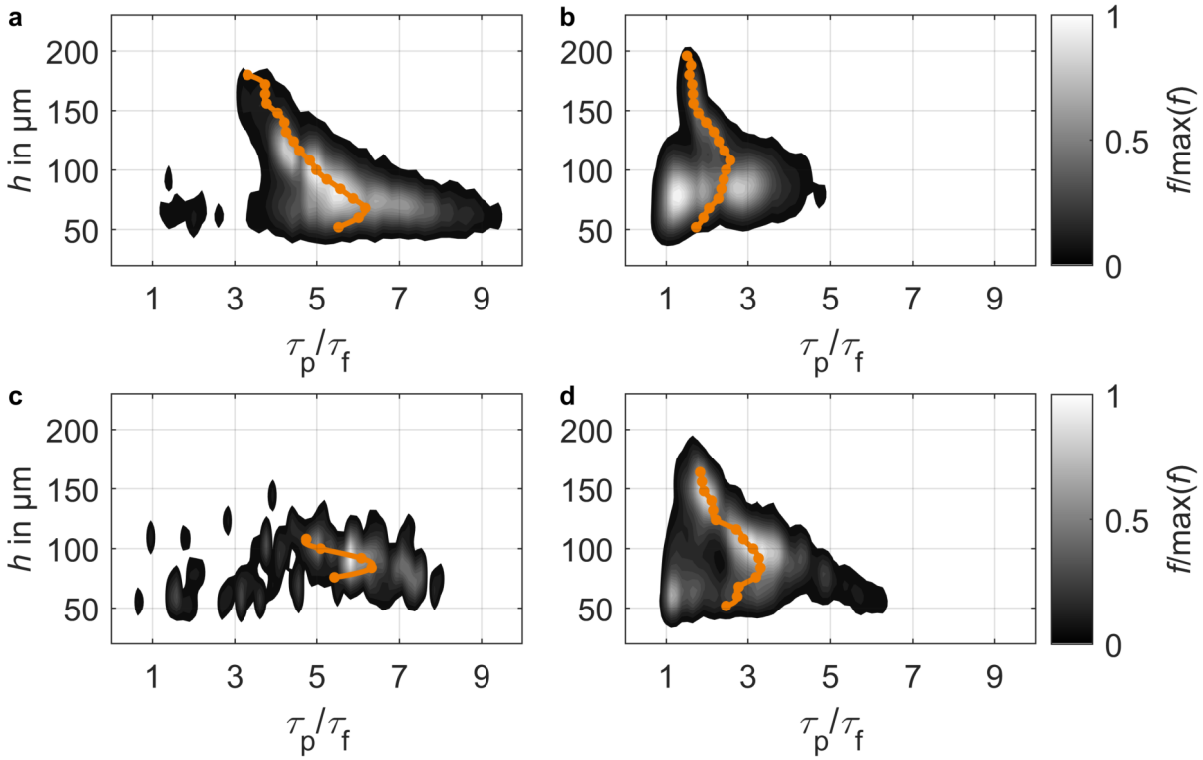

Figure 4.10: Normed number density distribution over RT ratio of crystals for experiments in the setup in Figure 4.4c. Mean RTs (orange markers) are shown for size classes with more than 10 crystals. (a,b) Upward flow; (c,d) downward flow; (a,c) low Reynolds number with $\tau_f = 143\,s$; (b,d) high Reynolds number with $\tau_f = 99\,s$. The RTD for downward flow at the low Reynolds number is based on one experiment with seed size fraction B, all other RTDs are based on several experiments over the whole range of seed size fractions.

further increased to the transient region.

The RT of a mix of size fractions is compared to separate experiments in Table 4.6. In the mixed experiments, the RTD is slightly wider than in the separate experiments. One reason for the difference may be the increase in seed crystal mass for the mixed experiments. The seed crystal mass was $(0.115 \pm 0.003)\,g$ in the separate experiments and $(0.209 \pm 0.006)\,g$ for the mixed experiments. The suspension densities are still low and a mix of different sizes should not increase the viscosity or change other fluid properties. For a higher suspension density, the size-dependent RT effect should be smaller because the larger particles might hinder small ones to pass and inter-particulate forces increase. In this case, the crystal RT is expected to be more homogeneous but larger because of a higher fluid viscosity and more crystal collisions. In the experiments, the small seed size fraction A and the large seed size fraction D were used. Crystals of a selected size that is close to the peak size of each size fraction are considered, in particular, $(80 \pm 5)\,\mu m$ for the small crystals and $(160 \pm 5)\,\mu m$ for the large crystals. Comparing crystals of these sizes for both experiment types, the RT is slightly larger in the mixed experiments. The RT deviation between the separate and the mixed experiments is the same for both size fractions. Hence, the mixing does not affect crystals of varying sizes differently.

The crystallization phenomena may change the CSD during the experiments and distort

Table 4.6: Mean RT in separate and mixed-fraction experiments at a low flow rate in the setup in Figure 4.4a. The fractions are A, D and a mix thereof as depicted in Figure 4.2.

Source: Reprinted with permission from Wiedmeyer et al. (2017b). Copyright 2017 Wiley-VCH.

Mean τ_p in s	w of 10 wt %	h of 155 µm to 165 µm	h of 75 µm to 85 µm	w of 90 wt %
Large fraction	252	276	-	287
Large fraction in mix	244	300	-	318
Small fraction	367	-	485	561
Small fraction in mix	339	-	510	591

the RTD. There is no supersaturation in isothermal experiments, which prevents growth and nucleation, but nuclei result from initial breeding during dry seeding. Breakage is not anticipated because there are neither stirring nor strong shear rates. The suspension densities are low and, hence, aggregation is not expected.

Contrasting the HCTs in parts b and c of Figure 4.4, setup c has slightly higher torsion and pitch, but the Reynolds and Dean numbers and the total tube length are nearly identical. Hence, the RTDs, also, are qualitatively identical in Figures 4.9 and 4.10. The setups differ in the wall material, but glass and silicone are both smooth and no deviation in the RTD should be anticipated. Nevertheless, the hardness of the materials varies, and wall collisions might be different for the two materials. Glass is harder, and reflections might be stronger, which might lead to better mixing but might affect crystals of varying sizes differently. Figures 4.9 and 4.10 indicate a crystal-size-dependent RT in both setups, which is therefore not a result of special properties of one of the wall materials. Chen et al. (2015) compare tubes of different material regarding particle deposition. They also found no wall material difference regarding clogging. Overall, the tube wall material has a low effect on the RTD. The wall material was already discussed for the straight tube in Section 3.2. Compared with the straight glass tube, the glass HCT is integrated in a cooling jacket for stability and protection and can therefore not be changed in geometry after fabrication.

Comparing the upward and the downward flow direction, there is no difference in the mean RT and the RTD in Figures 4.9 and 4.10. The pitch was small in all setups. For a higher pitch, the impact of gravitation might be stronger, and the crystal RT might be larger in upward flow. A different RT behavior is expected for HCTs with horizontally coiled axes. There, all crystals have to move nearly vertically with and against gravitation. Jokiel and Sundmacher (2019) state that sufficient kinetic energy is required to lift particles by the height of a coil, while energy is consumed by friction. Higher Reynolds numbers are necessary to avoid sedimentation, which in turn requires longer tubes to provide similar RTs. Under those conditions, a size-dependent crystal RT is not anticipated because the particles locate in other radial flow regions.

There are no differences in the RTDs of the three setups, which can be expected because all setups are characterized by similar dimensionless numbers. Contrasting the HCT with the straight tube, in both setups, the largest particles are nearly as fast as the fluid, and a decrease in particle size leads, at first, to an increase in the RT, before it decreases again for very small particles. In both setups, particles of varying size are characterized by a similar qualitative behavior with regard to the RT. In the straight tube, at the transient flow rate, the ratio of the particle-to-fluid RT is similar to the values for the high flow rate

in the HCT, but for the laminar flow rate, the ratio is 23 to 28 and hence much larger than that in the HCT. Consequently, in the laminar region, mixing is much better for crystals of smaller density in the HCT, than for heavy glass beads in the straight tube. As anticipated, a large density difference with heavier particles and lower flow rates in the laminar regime lead to faster sinking and higher particle-to-fluid RT ratios. Both, straight tube and HCT have the potential to grow crystals of narrow RTDs. All in all, the HCT should be preferred to the straight tube, due to its compact design. Both configurations can be used in a different context to separate particles by size, when operated in batch mode.

All setups have crystal RTDs in the order of minutes, which is appropriate for growth crystallization experiments. One of the aims of this chapter was to produce crystals of a narrow CSD. Fluid and crystal dispersion were observed, which are expected to widen the CSD in growth experiments, due to resulting RT differences. For the higher flow rate, the mixing is sufficient and the RTD is still narrow. For the lower flow rate, small crystals are significantly slower than large crystals. Consequently, small crystals have higher RTs than large crystals and the small crystals have more time to grow. Hence, the HCT has the potential to narrow the CSD during growth in the laminar flow regime.

4.3.3 Crystal Growth

The aim of this section is to demonstrate that crystal growth can be realized in the HCT, and that crystals of a narrow CSD can be produced in the crystallizer.

In the previous section, isothermal experiments in the HCT were presented for similar operating conditions. Here, the inlet concentration is chosen, such that the solubility is reached at 313 K. The HCT is cooled below this temperature to establish a supersaturation that enables crystal growth.

The product CSDs of growth experiments of varying flow rate are shown in Figure 4.11. The focus is to identify differences in the product CSD due to a flow rate variation. There are two experiments for both, the low and the high mass flow rate. The conditions are identical, except that the supersaturation at the outlet is slightly lower in part c. In this case, a slightly lower growth is expected and observed, compared with part d. For both flow rates, the RTDs agree well. For the low flow rate, the product CSD is readily reproducible. The product density distribution of the small size seed fraction A reaches its highest density at approximately 125 µm for the low flow rate, and at 95 µm for the high flow rate. This confirms what can be anticipated: a larger product size is reached at the low flow rate, as the crystal RT is higher.

In Figure 4.12, the product CSDs are presented for experiments of identical inlet conditions, but increasing outlet supersaturation. As expected, the median crystal size increases with the supersaturation, from initially 85 µm to 96 µm, 132 µm and 137 µm. At the same time, with increasing product crystal size, the median crystal to fluid RT ratio decreases from 3.9 to 3.3, 3.2 and 2.6. The decrease in the RT can be anticipated for enlarging crystals due to their size-dependent velocity in the HCT. In Figure 4.12, the interquartile range related to the crystal number increased from initially 16 µm to 19 µm, 23 µm and 63 µm although the interquartile range related to the crystal volume remained nearly unchanged, with 18 µm at the start and 21 µm, 23 µm and 23 µm after the growth experiments. Hence, there is a considerable broadening of the number distribution in the experiment of the highest supersaturation, while the volume distribution width stays approximately constant for all experiments. The outlier can be explained by the small

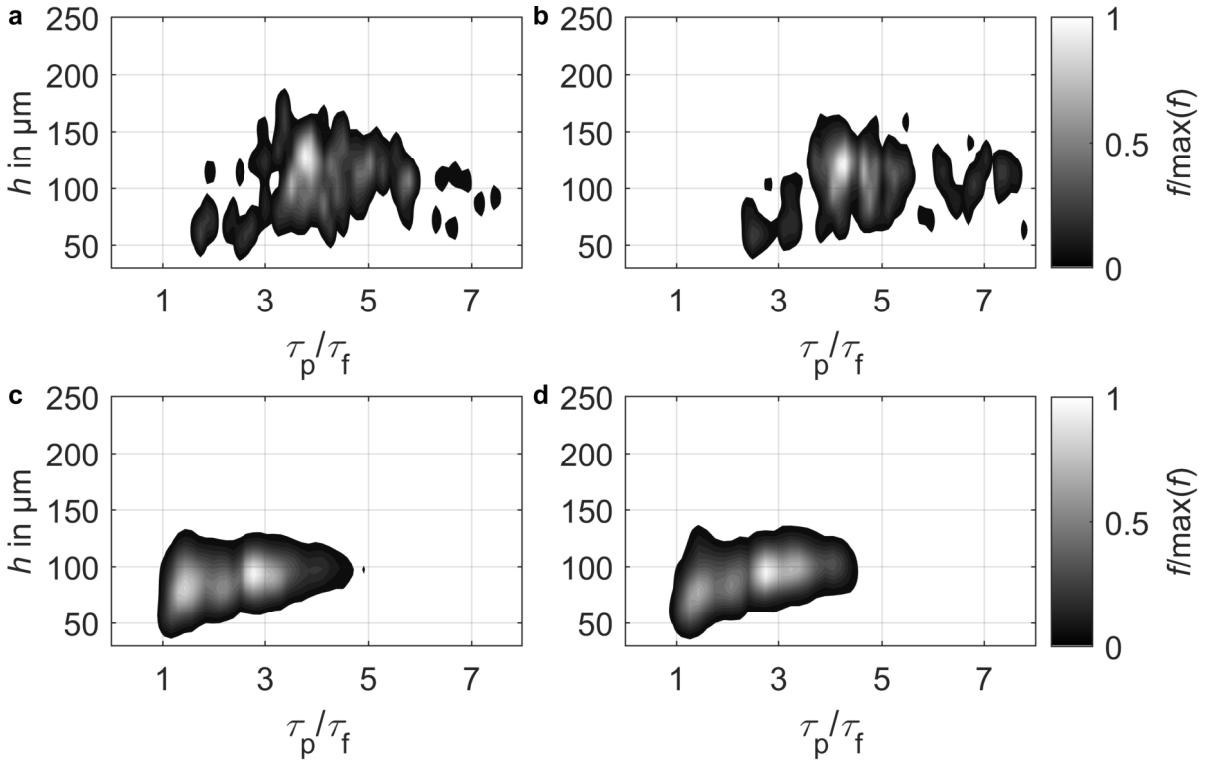

Figure 4.11: Normalized measured number density distribution at the HCT outlet in the setup in Figure 4.4c for upward flow, for the small seed size fraction A, for similar outlet percentage supersaturations: (a,b) both 4 % at the low flow rate; (c,d) 2 % and 4 % and both at the high flow rate.

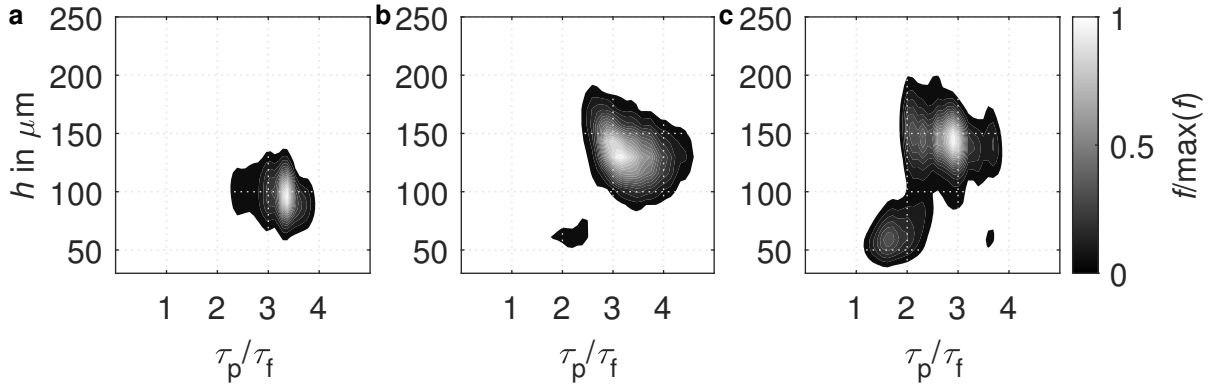

Figure 4.12: Normalized measured number density distribution at the HCT outlet in the setup in Figure 4.4a at a saturation temperature of 313 K for the smallest size fraction A at the low flow rate for increasing outlet percentage supersaturations from (a) to (c): 4 %, 14 % and 19 %.

Source: Reprinted with permission from Wiedmeyer et al. (2017b). Copyright 2017 Wiley-VCH. Modifications: smaller crystals considered in the data, x-axis scaled by fluid residence time, limits of y-axis changed, and names of symbols adjusted.

crystals that are visible in Figure 4.12c.

For the experiment at the highest supersaturation, the first quartile of the crystal number increases from 78 µm to 87 µm, whereas the first decile decreases from 71 µm to 58 µm. The smallest crystals may result from nucleation, and may be able to grow into the analyzed crystal size range at the highest supersaturation. Barrett and Glennon (2002) found primary nucleation of potash alum for a saturation temperature of 313 K at a percentage supersaturation of 18 % and 39 % for cooling rates of $0.003\,\mathrm{K\,s^{-1}}$ and $0.012\,\mathrm{K\,s^{-1}}$. Here, the cooling rate is stronger and the supersaturation of 19 % should be well in the metastable zone of primary nucleation. For secondary nucleation, the metastable zone width is smaller. Here, there is initially no clear solution, but seed crystals are used. Hence, secondary nucleation may be caused by the seeds. To estimate the influence of nucleation, the mass of nuclei in the product is calculated, when also taking into consideration particles from 17 µm to 50 µm. In experiment a, 1.0 % of the mass of crystals was smaller than 26 µm, and 2.7 % were smaller than 50 µm. In experiment b, 1.2 % were smaller than 75 µm. In experiment c, 5.9 % were smaller than 100 µm. Consequently, as observed before, there was considerable nucleation in the experiment at the highest supersaturation. For the other experiments, too, there were small crystals that cannot originate from primary nucleation, but must come from secondary nucleation. Overall, the mass percentage of the small crystals in the product was small, and had only a minor effect on the reduction of the supersaturation. Besenhard et al. (2017) reduce the influence of nuclei on the CSD by growth-dissolution cycles. In their HCT, the cycles are realized by sectional cooling and heating. The nuclei are dissolved in the dissolution cycle, while the desired larger crystals do not dissolve completely. Furthermore, the induction times in the growth cycle are short, which prevents nucleation in the first place. Another crystallization phenomenon, which may be enhanced in growth experiments, is aggregation. The aggregate-to-primary-crystal number ratio averaged over the growth experiments in Figure 4.12 is 0.9. The ratio was 0.2 in the ethanol experiments, and 1.9 in the isothermal experiments in Table 4.5. Therefore, the aggregate ratio after growth is within the range of the no-growth experiments. Consequently, significant aggregation of the seed fractions was not observable in the growth experiments. Breakage is not expected to occur, because the same flow rates and suspension densities as in the isothermal experiments were applied.

Variations in the crystal growth rate are described, using two concepts: growth rate dispersion and size-dependent growth (Garside et al., 2002). Growth rate dispersion was observed for potash alum, e.g., by Girolami and Rousseau (1985), Wang et al. (1990), and Tanneberger et al. (1996). The effect of growth rate dispersion is that a CSD broadens, and its mode decreases, during growth. Hence, the growth rate dispersion should increase the interquartile range in Figure 4.12, whereas the interquartile range related to the crystal volume stays approximately constant during the experiments. This can be explained with the size-dependent crystal RT, which counteracts the broadening of the CSD. Growth rate dispersion can be analyzed, considering bimodal experiments, with a small and a large crystal fraction, as illustrated in Figure 4.13. Growth rate dispersion does not affect the difference between the modes of two separate size fractions, whereas the size-dependent crystal velocity should lead to approaching modes for bimodal distributions. When only crystals with a minimum h of 50 µm are considered, in Figure 4.13, the distance of the mean sizes of the large and small fraction is initially 76 µm, and after growth it is 83 µm, 90 µm and 85 µm, and it remains approximately constant. The reason for the constant mode distance might be nucleation, which lowers the mean size of the small

crystal fraction during growth. Furthermore, Tanneberger et al. (1996) observed smaller growth rates for very small crystals up to a sieve range of 60 µm, compared with larger crystals of up to 500 µm. A sphere equivalent diameter of 60 µm to 500 µm corresponds to a value for the perpendicular face distance h of 25 µm to 211 µm. Their size range matches the size range in the present study. Hence, their observation might explain why the mode distance does not decrease in the present dissertation. Garside et al. (2002) mention three possible causes of size-dependent growth, which are mass transfer limitations, the Gibbs-Thomson or Ostwald-Freundlich effect, and size-dependent surface integration kinetics. They mention that permanent growth rate dispersion may also result from differences in surface-integration.

In the following, the effect of the seed mass on the concentration of the liquid phase during growth is estimated. In all growth experiments, the seed mass was approximately 0.1 g for the small-size seed fraction, and 0.3 g for the seeds from a mix of fractions. On the basis of a seed mass of 0.1 g, where the seeds are of a monodispersed size h at 85 µm, a monodispersed product size h of 140 µm is presumed. In this case, the crystal mass increases to 0.4 g. Provided that the low flow rate is applied, the corresponding crystal RT of 493 s is at its lower limit for the large product crystals and for isothermal experiments. While a total mass of 3.7 kg solution is fed, the fluid mass reduces by only 0.01 % by crystallization, and the reduction is negligible in terms of supersaturation. Locally, there may still be lower concentrations when the mixing is not sufficient. The figures indicate that the crystal-to-fluid RTD ratio exceeds one. The fluid is actually faster than the crystals, and the crystals are constantly fed with fresh solution of the initial concentration. Especially the slow small crystals are fed with fresh solution, which again offers a potential to approach the size of the large crystals during growth. Hence, the applied seed crystal mass does not affect growth by a reduction in the concentration of the fluid phase. For experiments with continuous seeding, the suspension density has to be limited, when a desired minimum mean crystal size shall be reached at a fixed tube length. Furthermore, in practice, the supersaturation should remain in the metastable zone, and seeded operation should be chosen to avoid wall fouling and nucleation.

One aim of this chapter was to grow crystals with a narrow CSD. The interquartile range regarding the crystal number increased during growth. This increase is caused by secondary nuclei, which result from seeding and were observed at the lower size bound. Nevertheless, the interquartile range regarding the crystal volume increased only slightly, from 18 µm at the start to (22 ± 1) µm, whereas the crystal median size increased from 85 µm to 96 µm, 132 µm and 137 µm, for experiments of an increasing supersaturation in the HCT setup a. On the one hand, potash alum is prone to growth rate dispersion, which widens the CSD. Insufficient mixing and broad RTDs lead, also, to an increase of the CSD width. On the other hand, the size-dependent crystal velocity can narrow the CSD. The experiments have shown that the effects balance out, and that the width of the CSD with regard to the crystal volume remained constant during crystal growth.

4.4 Summary of the Chapter

Three different HCTs with different wall material, flow mode, and cooling strategies but of similar dimensionless numbers were implemented and investigated experimentally. The wall material, flow direction of the suspension and cooling strategy did not lead to qualitative deviations in the RTD and CSD, between the setups. The mixing of the fluid in the HCTs deviated from PF for laminar inlet flow rates, and, here, axial dispersion

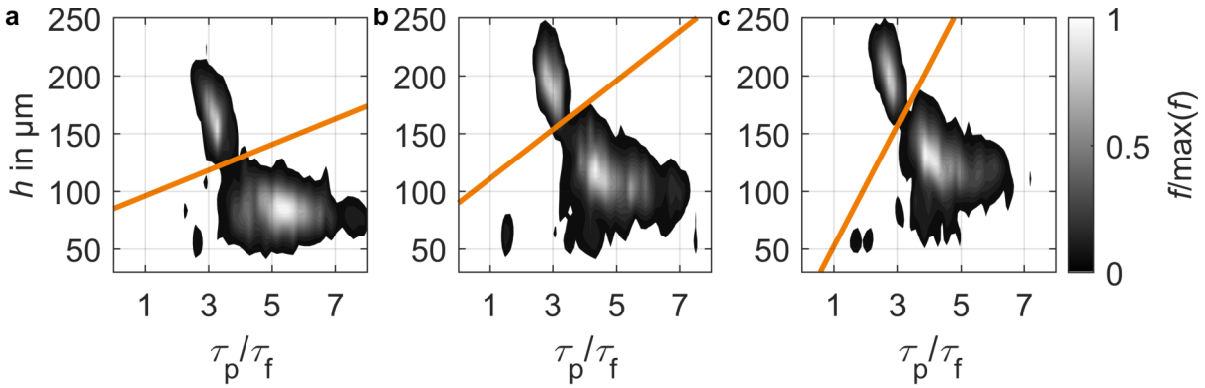

Figure 4.13: Normalized measured number density distribution at the HCT outlet in the setup in Figure 4.4b for the mix of a small seed size fraction A and a large seed size fraction D. The fractions are separated by an orange line for which the slope was adjusted by visual inspection. Experiments at the low flow rate for increasing outlet percentage supersaturations from (a) to (c): 1 %, 10 % and 14 %.

Source: Adapted with permission from Wiedmeyer et al. (2017a). Copyright 2017 American Chemical Society.

occurs. The crystal RT was larger than the fluid RT, but it approached the fluid RT for the higher laminar flow rate. All RTs were in the order of minutes. Large crystals were faster than small crystals for the chosen conditions, where the crystals have a higher density than the fluid. A size-dependent velocity was observed in the HCTs of small pitch and for heavy spherical glass beads in a straight horizontal tube. During crystallization, small crystals had a larger RT in the crystallizer and thus more time to grow. Hence, there was a potential to narrow the CSD during growth. The narrowing was balanced by an imperfect mixing and by growth rate dispersion. Aggregation and breakage were not observed, but secondary nucleation was observed for a high supersaturation. Secondary nucleation affected the number distribution, but not the volume distribution. All in all, the CSD stayed approximately constant during growth in the setup. Potash alum crystals were grown successfully by cooling crystallization. A size-dependent RT was observed in the horizontal straight tube experiments, in the HCT experiments, and in literature, but has not yet been explained. The next chapter seeks to explain the size dependency based on a single particle force model.

Outlook to Size and Shape Distributions

Potash alum crystals were modeled here as octahedra. The shape of an octahedron can be described with one size coordinate. For other substances, it may be necessary to consider multiple internal size coordinates to describe the crystal shape. A multivariate CSSD results. For example, needle-forming compounds, like potassium dihydrogen phosphate (KDP), can be described with a bivariate size coordinate vector (Borchert et al., 2014). In this case, the width of the product CSSD is not only influenced by the mixing and the RTD of the crystals, but can also be influenced by choosing an appropriate supersaturation. A shape modification can be achieved during crystal growth, if the face-specific crystal growth rates are different. When the difference varies with the supersaturation, the attainable region in the internal coordinate space increases further. The attainable region can be further increased when growth and dissolution cycles are combined, presuming that

the dissolution rates deviate from the negative growth rates as for KDP (Eisenschmidt et al., 2015). For KDP, the CSSD was changed successfully by Eisenschmidt et al. (2016), in batch experiments. For multivariate crystals of higher dimension, a stereo-microscope may be necessary for shape estimation, and crystals may be approximated by polytopes (Schorsch et al., 2012, 2014). Batch experiments can, in theory, be transferred to plug flow experiments when the time coordinate is realized along space in a tube. For univariate distributions, Besenhard et al. (2017) narrowed a CSD by dissolution of fine particles in growth and dissolution cycles for a segmented flow in an HCT crystallizer.

5 Model and Simulations of a Single Particle in a Straight Tube

A size-dependent RT was observed in the tubular experiments in Chapters 3 and 4. This chapter shall explain the observation. The straight horizontal setup is modeled and simulated as representative for both tubular setups, as it is less complex from a modeling perspective.

In literature, a size-dependent RT was observed and explained for buoyant particles in a slightly different setup with a vertical tube. Segré and Silberberg (1961) experimentally measured a tubular pinch effect, which means that particles are located in a thin annular region. Cheng et al. (2005) ascribe the Segré–Silberberg effect to the combination of the nonlinear influence of inertia, wall effects, velocity profile curvature, and shear force.

Matas et al. (2004) mention the same reasons for horizontal configurations. Their theoretical results of simulations in a channel are based on the asymptotic theory that is limited to small Re_p and to particles that do not move close to the wall. For slightly non-neutrally buoyant particles, they state that, in addition, Saffman's lift force is relevant to explain the migration of particles. They have also observed the effect in experiments in a horizontal tube.

Baptista et al. (1996b) evaluated experiments with non-neutrally buoyant spheres in a straight, nearly horizontal tube, with a replicated full factorial design at two levels. They found that particle density and fluid velocity affect the normalized linear velocity the most, and that particle diameter as well as tube inclination are still significant. The mean particle RT increased with particle density, and decreased with flow rate and particle diameter. They concluded that larger particles experience a higher drag force. In their report, the particle-to-tube diameter ratio was approximately one third for small particles and almost equal to one half for large particles. Here, the ratio is much smaller. The largest particles have a diameter equal to 8 % of the tube diameter.

A size dependency was also observed in coiled tubes. Redlinger-Pohn et al. (2016b) performed experiments and computational fluid dynamics (CFD)-discrete element method (DEM) simulations with fibers of suspension mass concentrations in the range of 0.25 % to 0.5 % in a coiled tube, which is coiled around a vertical axis. The tube is usually used as a tube flow fractionator. They also found that longer fibers had a shorter mean RT. They state two possible reasons: first, a change in the effective density of flocculating fibers, and second, a difference in alignment of the fibers, with the fluid where longer fibers align better with the axial stream. Both reasons do not apply to glass beads.

For transportation, tubes shall be as short as possible. For heat exchange, very short tubes are usually also sufficient. In contrast, for cooling crystallization, large RTs and long tubes may be desired. Considering straight tubes, simulations and experiments were often conducted in short tubes from 1 m to 2 m length (Cheng et al., 2005; Segré and Silberberg, 1961; Baptista et al., 1996b). Matas et al. (2004) performed experiments in a 2.6 m tube, and simulations in a channel of 5 m length, which corresponds to 15 % of the duct length to diameter ratio, compared with the present dissertation. They show

in simulations that non-neutrally buoyant particles accumulate at the lower wall, where the particles get closer to the lower wall with an increasing pipe length to diameter ratio. Matas et al. (2004) state that particles assemble at a single point of the cross-section near the tube bottom for infinitely large ratio. Longer straight tubes and HCTs, which are of length similar to the ones in the present dissertation, were used by Chakrabandhu and Singh (2006). They investigated the influence of different flow rates and food particle concentrations. Because of the use for food processing, their tube had a larger particle-to-tube diameter ratio of 26 %, and their particles were nearly neutrally-buoyant.

The mentioned investigations focused on measuring RT, and identifying the main parameters affecting it. Simulations of coiled tubes apply advanced flow models with multidimensional equations and extensive force models (Tiwari et al., 2006; Redlinger-Pohn et al., 2016b). They focus on the prediction of the distribution of particles along the tube radius and axis, which results from the complex secondary motion of the fluid. It is not the aim of the present study to simulate the particle RT with perfect agreement between simulation and experiment. This could be done better with the aforementioned advanced numerical methods and extended models. However, this level of complexity might not be necessary to explain the cause of a size-dependent RT, which was also observed in straight tubes. The aim is to identify the dominating forces causing the effect from first principles. The forces are the basis of a single particle linear momentum balance model, which is developed in the following.

The questions to be answered in this chapter are:

1. Does a single particle model, which is based on a momentum balance, reproduce size-dependent RTs for the parameter range that corresponds to the experiments?

2. What are the dominant forces that cause the size-dependent particle RT?

3. How to choose material and process parameters, in particular collision coefficients, particle density, fluid velocity, and tube length, to induce or avoid a size-dependent particle RT?

4. What parameter adaptions and model extensions might improve the agreement between model and experimental results?

5.1 Model

The particle movement is modeled in Cartesian coordinates $\mathbf{r} = \begin{pmatrix} x \\ y \\ z \end{pmatrix}$. It is assumed that the origin is in the middle of the tube inlet, as illustrated in Figure 5.1. For the fluid, a Hagen-Poiseuille flow is assumed

$$v_{\mathrm{f},z} = v_{\mathrm{f,max}} \left(1 - \frac{x^2 + y^2}{R^2} \right) \tag{5.1}$$

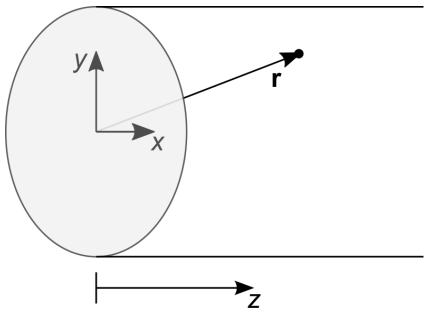

Figure 5.1: Schematic of the straight tube with Cartesian coordinates. The particle is located at the circle marker at position **r**.

where $v_{\mathrm{f},z}$ is the fluid velocity in the z-direction, $v_{\mathrm{f,max}}$ is its maximum, and R is the tube radius. The change in the particle position **r** equals the particle velocity vector

$$\frac{\mathrm{d}}{\mathrm{d}t}\begin{pmatrix} x \\ y \\ z \end{pmatrix} = \begin{pmatrix} v_{\mathrm{p},x} \\ v_{\mathrm{p},y} \\ v_{\mathrm{p},z} \end{pmatrix} = \mathbf{v}_{\mathrm{p}} \tag{5.2}$$

The change in the particle velocity $\mathbf{v}_{\mathrm{p}}$ is described by

$$\frac{\mathrm{d}}{\mathrm{d}t}\begin{pmatrix} v_{\mathrm{p},x} \\ v_{\mathrm{p},y} \\ v_{\mathrm{p},z} \end{pmatrix} = \begin{pmatrix} a_{\mathrm{p},x} \\ a_{\mathrm{p},y} \\ a_{\mathrm{p},z} \end{pmatrix} = \mathbf{a}_{\mathrm{p}} \tag{5.3}$$

where $\mathbf{a}_{\mathrm{p}}$ is the vector of the acceleration of a particle and $a_{\mathrm{p},x/y/z}$ are its components.

The motion of a sphere falling in a quiescent fluid can be modeled by the Basset-Boussinesq-Oseen equation, as stated by Crowe et al. (2012); Groll (2015). Maxey and Riley (1983) derived an equation of motion for a sphere in nonuniform unsteady flow. They include the body force due to gravity, undisturbed flow, steady state drag, virtual (also added or apparent) mass term, and the Basset (also history) term (as cited in Crowe et al. (2012)). Their correlation is valid for Stokes flow, that is, for small Reynolds numbers $Re \ll 1$ (Michaelides et al., 2017). Crowe et al. (2012) rewrite the equation and additionally consider Saffman lift and Magnus lift. Zhu et al. (2007) review the particle-fluid interaction forces, and the corresponding models that are typically used in discrete particle simulations. They state drag force, pressure gradient force, virtual mass force, Basset force, Saffman force, and Magnus force. Here, a simplified model is applied. The drag force $\mathbf{F}_{\mathrm{D}}$, the gravity and buoyancy force $\mathbf{F}_{\mathrm{GB}}$, and the Saffman force $\mathbf{F}_{\mathrm{S}}$ are considered in the momentum balance

$$\frac{\mathrm{d}\mathbf{v}_{\mathrm{p}}}{\mathrm{d}t} = \frac{1}{m_{\mathrm{p}}}\left(\mathbf{F}_{\mathrm{D}} + \mathbf{F}_{\mathrm{GB}} + \mathbf{F}_{\mathrm{S}}\right) \tag{5.4}$$

where it is assumed that the particle has a constant mass m_{p}. The neglected forces are further discussed in Section 5.6.

Drag Force

In general, the drag force $\mathbf{F}_{\mathrm{D}}$ is defined over the cross sectional area of a particle, perpendicular to the relative flow direction. For a sphere, the drag force is

$$\mathbf{F}_{\mathrm{D}} = 3\pi\eta_{\mathrm{f}} d_{\mathrm{p}} \mathbf{v}_{\mathrm{rel}} f_{\mathrm{D}} \tag{5.5}$$

where η_f is the dynamic viscosity of the fluid and the correction factor of the Stokes drag force f_D is

$$f_\mathrm{D} = \frac{Re_\mathrm{p} c_\mathrm{D} f_\mathrm{G}}{24} \tag{5.6}$$

where c_D is the drag coefficient, f_G is the Goldman correction factor, and the relative linear velocity is

$$\mathbf{v}_\mathrm{rel} = \mathbf{v}_\mathrm{f} - \mathbf{v}_\mathrm{p}$$

For Hagen-Poiseuille flow, the relative velocity is

$$\mathbf{v}_\mathrm{f} - \mathbf{v}_\mathrm{p} = \begin{pmatrix} 0 - v_{\mathrm{p},x} \\ 0 - v_{\mathrm{p},y} \\ v_{\mathrm{f},z} - v_{\mathrm{p},z} \end{pmatrix}$$

and the magnitude of the relative velocity is

$$|\mathbf{v}_\mathrm{f} - \mathbf{v}_\mathrm{p}| = \sqrt{v_{\mathrm{p},x}^2 + v_{\mathrm{p},y}^2 + \left(v_{\mathrm{f},z} - v_{\mathrm{p},z}\right)^2}$$

The particle Reynolds number is the ratio of inertial to viscous forces

$$Re_\mathrm{p} = \frac{\rho_\mathrm{f} d_\mathrm{p} \left|\mathbf{v}_\mathrm{f} - \mathbf{v}_\mathrm{p}\right|}{\eta_\mathrm{f}} \tag{5.7}$$

For low Reynolds numbers $Re_\mathrm{p} < 1$, Stoke's law applies and the drag force becomes

$$\mathbf{F}_\mathrm{D} = 3\pi\eta_\mathrm{f} d_\mathrm{p} \left(\mathbf{v}_\mathrm{f} - \mathbf{v}_\mathrm{p}\right) f_\mathrm{G}$$

In the range $1 < Re_\mathrm{p} < 800$, a drag coefficient, which is calculated following Schiller and Naumann (1933), is valid and the drag force becomes

$$\mathbf{F}_\mathrm{D} = 3\pi\eta_\mathrm{f} d_\mathrm{p} \left(\mathbf{v}_\mathrm{f} - \mathbf{v}_\mathrm{p}\right) \left(1 + 0.15 Re_\mathrm{p}^{0.687}\right) f_\mathrm{G} \tag{5.8}$$

For smaller Re_p, Eq. (5.8) approaches Stoke's law. Hence, Eq. (5.8) is applied for all Re_p.

The drag coefficient increases if a particle moves near a wall, which can be considered by a correction factor f_G, which is depicted in Figure 5.2 for small wall distances. The distance δ between tube wall and sphere hull in the cross-section of the tube is

$$\delta = R - \frac{d_\mathrm{p}}{2} - \sqrt{x^2 + y^2}$$

In case of a sphere moving parallel to a wall, for large gap width and for the Stokes regime, Goldman et al. (1967), Schäffer et al. (2007) and Happel and Brenner (1983) use an expression by Faxén

$$f_\mathrm{G,parallel} = \left(1 - \frac{9}{16}\left(\frac{d_\mathrm{p}}{2\delta + d_\mathrm{p}}\right) + \frac{1}{8}\left(\frac{d_\mathrm{p}}{2\delta + d_\mathrm{p}}\right)^3 - \frac{45}{256}\left(\frac{d_\mathrm{p}}{2\delta + d_\mathrm{p}}\right)^4 - \frac{1}{16}\left(\frac{d_\mathrm{p}}{2\delta + d_\mathrm{p}}\right)^5\right)^{-1}$$

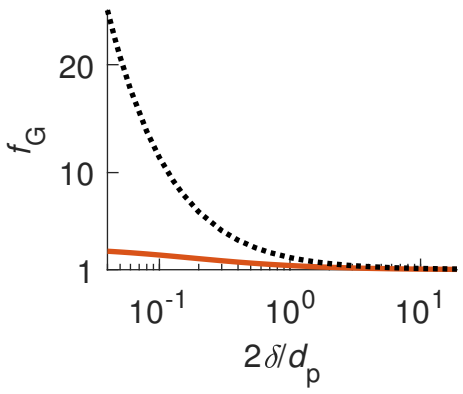

Figure 5.2: Goldman correction factor of the drag force over the ratio of gap width to particle radius for a particle moving parallel (orange solid, Eq. (5.1)) and normal (black dotted, Eq. (5.1)) to a wall.

Faxén's expression is employed for $\frac{2\delta}{d_\mathrm{p}} \leq 100$. For larger values of $\frac{2\delta}{d_\mathrm{p}}$, $f_{\mathrm{G,parallel}} < 1.01$ and no correction is applied, that is, $f_{\mathrm{G,parallel}}$ is set to one. The correlation is applied for movement parallel to a wall, which is in this case parallel to the axial direction z. For $f_{\mathrm{G,n}}$ in the normal direction, there is an exact solution by Brenner (1961). Schäffer et al. (2007) derived a 12th order approximation, which deviates less than 0.3 % from Brenner's exact formula over the whole range of δ. To reduce the numerical effort a 5th order approximation of this correlation

$$f_{\mathrm{G,n}} = \left(1 - \frac{9}{8}\left(\frac{d_\mathrm{p}}{2\delta + d_\mathrm{p}}\right) + \frac{1}{2}\left(\frac{d_\mathrm{p}}{2\delta + d_\mathrm{p}}\right)^3 - \frac{57}{100}\left(\frac{d_\mathrm{p}}{2\delta + d_\mathrm{p}}\right)^4 - \frac{1}{5}\left(\frac{d_\mathrm{p}}{2\delta + d_\mathrm{p}}\right)^5\right)^{-1}$$

is used for $\frac{2\delta}{d_\mathrm{p}} \leq 100$, whereas for larger values $f_{\mathrm{G,n}}$ is set to one. The correlation is applied in the x- and y-direction.

Gravity and Buoyancy Force

The sum of the force induced by gravity and buoyancy $\mathbf{F}_{\mathrm{GB}}$ acts only in vertical y-direction and it is

$$F_{\mathrm{GB},y} = (\rho_\mathrm{f} - \rho_\mathrm{p})\, V_\mathrm{p} g \tag{5.9}$$

where g is the magnitude of the gravity of Earth, and V_p is the volume of a particle.

Saffman Lift Force

The Saffman lift force $\mathbf{F}_\mathrm{S}$ is given by Zhu et al. (2007) in a general formulation, and for Hagen-Poiseuille flow it becomes

$$\mathbf{F}_\mathrm{S} = -1.615 d_\mathrm{p}^2 \sqrt{\frac{2 v_{\mathrm{f,max}} \eta_\mathrm{f} \rho_\mathrm{f}}{R^2 \sqrt{x^2 + y^2}}} \begin{pmatrix} x\,(v_{\mathrm{f},x} - v_{\mathrm{p},x}) \\ y\,(v_{\mathrm{f},x} - v_{\mathrm{p},x}) \\ x v_{\mathrm{p},x} + y v_{\mathrm{p},y} \end{pmatrix} f_\mathrm{S}$$

In the center of the cross section of the tube, there is zero division, which should be avoided. Consequently, $\mathbf{F}_\mathrm{S}$ is set to zero at the tube center. Furthermore, there is no Saffman force when there is neither particle movement in the circular cross-section nor relative velocity in the x-coordinate. Crowe et al. (2012); Sommerfeld (2013) propose

to use the correlation of Mei (1992) to describe the Saffman force for higher Reynolds numbers where a correction factor is used. The correction factor for $Re_\mathrm{p} \leq 40$ is

$$f_\mathrm{S} = \left(1 - 0.3314\sqrt{\beta_{Re}}\right) \exp\left(-\frac{Re_\mathrm{p}}{10}\right) + 0.3314\sqrt{\beta_{Re}}$$

and for $Re_\mathrm{p} \geq 40$, here applied for $Re_\mathrm{p} > 40$, it is

$$f_\mathrm{S} = 0.0524\sqrt{\beta_{Re} Re_\mathrm{p}}$$

where the dimensionless shear rate β_{Re} is

$$\beta_{Re} = 0.5\frac{Re_\mathrm{s}}{Re_\mathrm{p}}$$

where zero division occurs for $Re_\mathrm{p} \leq 40$ when $|\mathbf{v}_\mathrm{f} - \mathbf{v}_\mathrm{p}| = 0$, which means that the particle does not move in the cross section, that is to say, $v_{\mathrm{p},y} = 0$ and $v_{\mathrm{p},x} = 0$, and simultaneously the particle velocity equals the fluid velocity in z-direction $v_{\mathrm{f},z} - v_{\mathrm{p},z} = 0$. Thus, $\mathbf{F}_\mathrm{S}$ is set to zero if $|\mathbf{v}_\mathrm{f} - \mathbf{v}_\mathrm{p}| = 0$ for $Re_\mathrm{p} \leq 40$. For Hagen-Poiseuille flow, the shear Reynolds number (Crowe et al., 2012; Sommerfeld, 2013) is

$$Re_\mathrm{s} = d_\mathrm{p}^2 \frac{\rho_\mathrm{f}}{\eta_\mathrm{f}} \sqrt{\left(\frac{\partial v_{\mathrm{f},z}}{\partial x}\right)^2 + \left(\frac{\partial v_{\mathrm{f},z}}{\partial y}\right)^2}$$

5.2 Model Assumptions

The assumptions, which were applied in the derivation of the model in Section 5.1, are given below. It is discussed how the simulation results might be affected, if the assumptions were dropped. The relative importance of the assumptions is estimated.

a) The particle mass is constant. This assumption applies for glass beads that are not brittle.

b) Particles are spherical. This assumption is reasonable because the manufacturer (Sigmund Lindner) states that the roundness, which is defined as ratio of minimal to maximal diameter, is at least 0.95.

c) The tube is horizontal. This is the case for the main part of the tube, where the last 0.5 m show an inclination of 53°. An inclination of the tube can be included in Eq. (5.9). The force should be divided into a y- and a z-component, by considering the cosine and sine of the angle of inclination. Looking at the tube, sedimentation was not observed in the inclined part.

d) Several forces were neglected in the momentum balance compared with the Basset-Boussinesq-Oseen equation. An overview of correlations and coefficients for transient flow in the Stokes regime, and for small and high Reynolds numbers is given by Michaelides et al. (2017). They state that unsteady forces should be included when the characteristic time of the fluid and the particle response time are of the same order. This is the case here for larger particles as explained in Section 5.4.1. Another force is the Magnus force, which is discussed in Section 5.6.1.

The rolling resistance force was disregarded. Related friction coefficients can be found for example for dry glass beads on steel (Mader-Arndt et al., 2017), but may vary strongly under wet conditions. The results may not be transferable to angular crystals. Friction results, also, in a pressure gradient along the tube. The pressure-induced buoyancy force can be formulated following Groll (2015) as

$$F_{\mathrm{GB},z} = -V_{\mathrm{p}} \Delta p$$

Estimates of the pressure drop in axial direction caused by the fluid are given in the following. According to Glück (1988), the pressure drop, which originates from tubular friction, is

$$\Delta p = \lambda_{\mathrm{friction}} \frac{l \rho_{\mathrm{f}}}{4R} \frac{v_{\mathrm{f,max}}^2}{4}$$

where $\lambda_{\mathrm{friction}}$ is the friction factor. For laminar flow, Glück (1988) derives the friction factor

$$\lambda_{\mathrm{friction}} = \frac{64}{Re}$$

For the straight tube at $v_{\mathrm{f,low}}$, a pressure drop Δp =1×10^4 Pa results when the parameters, which will be introduced in Section 5.4, are applied. For turbulent flow, empirical friction factors are available. Following Kast et al. (2013), the Blasius friction factor for $3000 < Re < 10^5$ is

$$\lambda_{\mathrm{friction}} = 0.316 Re^{-0.25}$$

and at $v_{\mathrm{f,high}}$ in the straight tube, the pressure drops by 2.8×10^4 Pa. As $v_{\mathrm{f,high}}$ is in the transient flow regime, Eq. (5.2) leads to undervaluation and the turbulent correlation should be used for estimation. In coiled tubes, higher losses are caused by the secondary motion of the fluid towards the wall. An additional pressure loss due to friction is induced by the particles. Correlations for this additional term are given by Muschelknautz (2013).

e) There is no particle rotation. Section 5.6.1 examines this assumption.

f) The fluid follows a Hagen-Poiseuille profile. This is a typical assumption for laminar straight tubes. The fluid velocity $v_{\mathrm{f,low}}$ is laminar, and for the HCT, both fluid velocities are in the laminar regime. The fluid velocity $v_{\mathrm{f,high}}$ in the straight tube is not yet turbulent but in the transient region. Deviations from the Hagen-Poiseuille flow may occur. The fluid profile may further be disturbed at the tube connectors in the glass tube. The experimental results in Figure 3.2 confirm this, because there are larger deviations in the glass tube, but the mean RTs for glass and silicone tubes still agree well.

On the experimental side, air bubbles are difficult to distinguish via imaging from spherical glass beads, which are distributed in size. Blind experiments may be used to estimate their number and size. Preferably, bubbles should be avoided a priori. At large values of v_{f}, a debubbler may be used. In the experiments, the system was operated under pressure, and not via suction. Water was initially not completely degassed. It was pumped through the pipe for several minutes at higher flow rates, to flush the system and to remove air bubbles. Experiments were started when no air bubbles were visible at the outlet. Small air bubbles in the straight tube may change the fluid velocity locally, and disturb the particle trajectories, or may attach

to glass beads. Air bubbles may reduce the RT, by lifting particles in regions of higher velocity in the cross section of the tube. For glass beads and crystals of high density, the effect on the RT is expected to be small as they sediment again quickly. Resulting changes in the glass bead model properties, such as size or density, may be expected to affect the RT similarly for both fluid velocities. This would not improve the agreement between simulations and experiments for both velocities.

To account for a change in the fluid velocity profile in the single particle model, the Hagen-Poiseuille profile may be varied, or a random force may be added to represent disturbances of the fluid flow, similar to diffusion. With implemented disturbances, it is expected that the simulated particle RT reduces, especially for small particles. The maximum RT in Figure 5.4 would decrease, which would lead to a smaller difference to the experimental results. Alternatively, a direct numerical simulation may be applied, including a two-way-coupling and a resolution of the boundary layer of the spheres.

g) A single particle was modeled. Hence, it was assumed that there are no particle-particle interaction effects, and the fluid is not influenced by the particles. In experiments and simulations with particle clouds, particles may move faster in the shadow of other particles, and because of additional random movement. Baptista et al. (1996a) studied particles of larger particle-to-tube diameter ratio, smaller density difference, and larger suspension density compared with the present study. They found experimentally that the mean residence of clouds increases, compared with single particles at low particle concentrations of 1 vol%. When particles of various sizes are mixed, the mean RT reduces in most cases. Legrand et al. (2007) also consider density effects of non-neutrally buoyant particles. Again, the particles are of larger particle-to-tube diameter ratio and smaller density difference, and there is a high suspension density compared with this dissertation. They found that for horizontal ducts, high particle concentrations are necessary to form a uniform bed. At low particle concentrations, as applied here, the flow regime dominates the suspension behavior. Regarding the mixing of particles, further quite recent studies are available for neutrally buoyant particles, especially in food industries and biological physics (Chakrabandhu and Singh, 2006; Prohm et al., 2012; Rusconi et al., 2014; Gao et al., 2019; Schaaf et al., 2019).

5.3 Implementation

To avoid numerical issues due to frequent wall collisions, the model is implemented via a forward simulation scheme, the first-order Euler method, to be precise. A Taylor series approximation is used to calculate the particle position $\mathbf{r}$ following Eq. (5.2) and the particle velocity v_p following Eq. (5.3). The implemented approach is

$$\mathbf{a}_\mathrm{p}\left(n_t\right) = \frac{\mathbf{F}\left(n_t\right)}{m} \tag{5.10}$$

$$\mathbf{r}\left(n_t+1\right) = \mathbf{r}\left(n_t\right) + \mathbf{v}_\mathrm{p}\left(n_t\right)\Delta t\left(n_t\right) \tag{5.11}$$

$$\mathbf{v}_\mathrm{p}\left(n_t+1\right) = \mathbf{v}_\mathrm{p}\left(n_t\right) + \mathbf{a}_\mathrm{p}\left(n_t\right)\Delta t\left(n_t\right) \tag{5.12}$$

where n_t is the index of the current time step. The next time step results from

$$t\left(n_t+1\right) = t\left(n_t\right) + \Delta t\left(n_t\right)$$

The implemented equation system is similar to the implementation of a spiral air classifier by Sommerfeld (2013). The resulting force $\mathbf{F}$ contains the single forces mentioned in the momentum balance in Eq. (5.4).

When a particle touches the wall during a time step, the particle is reflected. The boundary of a particle impacts a wall when

$$\sqrt{x^2 + y^2} = R - \frac{d_\mathrm{p}}{2}$$

After collision, the particle moves with a new velocity for the remainder of the time step. In forward implementation, it may happen that a particle leaves the tube in the radial direction within a time step. Then, the point of wall contact, the corresponding wall impact velocity v_p^b and the elapsed time must be identified. A detailed description of the corresponding algorithms is given in Appendix B where the velocity after collision $\mathbf{v}_\mathrm{p,elastic}^\mathrm{a}$ is calculated for a perfectly elastic wall reflection.

To account for wall elasticity, the particle wall collision model of Groll (2015) is applied to $\mathbf{v}_\mathrm{p,elastic}^\mathrm{a}$. It gives correlations for the velocities after collision for a movement parallel and normal to a plane. The velocities in the cross section after an elastic collision are formulated according to the normal velocity

$$v_{\mathrm{p},x}^\mathrm{a} = e_\mathrm{c} v_{\mathrm{p},x,\mathrm{elastic}}^\mathrm{a} \tag{5.13a}$$

$$v_{\mathrm{p},y}^\mathrm{a} = e_\mathrm{c} v_{\mathrm{p},y,\mathrm{elastic}}^\mathrm{a} \tag{5.13b}$$

and the axial velocity is calculated according to Groll's parallel velocity

$$v_{\mathrm{p},z}^\mathrm{a} \left(\frac{v_{\mathrm{p},z}^\mathrm{b}}{-v_\mathrm{p,n}^\mathrm{b}} > \mu_\mathrm{c} \left(1 - e_\mathrm{c}\right) \right) = v_{\mathrm{p},z}^\mathrm{b} + \mu_\mathrm{c} \left(1 - e_\mathrm{c}\right) v_\mathrm{p,n}^\mathrm{b} \tag{5.13c}$$

where μ_c is the collision friction coefficient, where e_c is the collision elasticity coefficient, which varies between zero and one, and where the normal velocity before collision

$$v_\mathrm{p,n}^\mathrm{b} = -\cos\left(\beta\right) \sqrt{{v_{\mathrm{p},x}^\mathrm{b}}^2 + {v_{\mathrm{p},y}^\mathrm{b}}^2} \tag{5.14}$$

is negative. In Eq. (5.14), β is the angle between the radial orientation and the velocity vector in the circular cross section, as illustrated in Figure B.1. The right-hand side of Eq. (5.13c) may vanish or become negative after collision when $\frac{v_{\mathrm{p},z}^\mathrm{b}}{-v_\mathrm{p,n}^\mathrm{b}} \leq \mu_\mathrm{c} \left(1 - e_\mathrm{c}\right)$. In this case, the axial velocity remains unchanged

$$v_{\mathrm{p},z}^\mathrm{a} \left(\frac{v_{\mathrm{p},z}^\mathrm{b}}{-v_\mathrm{p,n}^\mathrm{b}} \leq \mu_\mathrm{c} \left(1 - e_\mathrm{c}\right) \right) = v_{\mathrm{p},z}^\mathrm{b}$$

For particles with a diameter below 100 µm and time steps Δt smaller than 1×10^{-5} s, memory issues appeared when preallocating the forward implementation. Results including particles smaller than 100 µm were calculated with an explicit fifth-order Runge-Kutta "ode45" solver (MATLAB). Nevertheless, this fifth-order solver was not applied for all simulations. The forward implementation is advantageous for particles that do not start at the origin and, hence, collide with the wall at a position with a non-zero x-coordinate, as further explained in Appendix A.

5.4 Process and Model Parameters

The applied simulation parameters are listed in Table 5.1. Two different pump speeds, called "low" and "high", were applied in the experiments. Measured mass flow rates were used to calculate corresponding average fluid velocities. The velocities $v_{\mathrm{f,max}}$ were calculated from these average velocities assuming a Hagen-Poiseuille flow profile. Initially, the particles start with zero velocity at the tube origin.

Table 5.1: Geometrical parameters, process parameters, and material parameters.

Symbol	Value	Unit
e_{c}	0.94	–
μ_{c}	0.325	–
g	9.81	$\mathrm{m\,s^{-2}}$
l	20.5	m
R	2.5×10^{-3}	m
$v_{\mathrm{f,max,low}}$	0.734	$\mathrm{m\,s^{-1}}$
$v_{\mathrm{f,max,high}}$	1.122	$\mathrm{m\,s^{-1}}$
η_{f}	1002×10^{-6}	$\mathrm{kg\,m^{-1}\,s^{-1}}$
ρ_{f}	998	$\mathrm{kg\,m^{-3}}$
ρ_{p}	2500	$\mathrm{kg\,m^{-3}}$

For a particle that reaches the upper limit of typical crystal sizes of 400 µm, and for a large relative velocity, which is obtained when a particle is initially at rest in the tube center, Re_{p} in Eq. (5.7) reaches 292 and 447 for $v_{\mathrm{f,max,low}}$ and $v_{\mathrm{f,max,high}}$. These values are well inside the validity region of Eq. (5.8).

5.4.1 Stokes Number

The Stokes number St, which is related to the particle velocity, describes how well a particle can follow the fluid when the fluid flow field changes. It is defined as

$$St = \frac{\tau_{\mathrm{p}}}{\tau_{\mathrm{f}}}$$

where τ_{f} is a time characteristic of the flow field and τ_{p} is the relaxation time or momentum response time. The momentum balance in Eq. (5.4) describes the movement of a particle. Disregarding body forces for particles of a high density compared with the fluid, Crowe (2006) assumes that the Stoke drag force determines the particle motion. Applying only the drag force, which was defined in Eq. (5.5), in the momentum balance in Eq. (5.4), the equation becomes

$$\frac{\mathrm{d}\mathbf{v}_{\mathrm{p}}}{\mathrm{d}t} = \frac{18\eta_{\mathrm{f}}}{{d_{\mathrm{p}}}^2\rho_{\mathrm{p}}} f_{\mathrm{D}} \left(\mathbf{v}_{\mathrm{f}} - \mathbf{v}_{\mathrm{p}}\right)$$

Provided that the correction factor of the Stokes drag force f_{D} is one, the Stokes τ_{p} is achieved. The first factor on the right-hand side is the reciprocal of τ_{p}

$$\tau_{\mathrm{p}} = \frac{{d_{\mathrm{p}}}^2\rho_{\mathrm{p}}}{18\eta_{\mathrm{f}}}$$

In general,

$$\frac{\mathrm{d}\mathbf{v}_{\mathrm{p}}}{\mathrm{d}t} = \frac{f_{\mathrm{D}}}{\tau_{\mathrm{p}}} \left(\mathbf{v}_{\mathrm{f}} - \mathbf{v}_{\mathrm{p}}\right) \tag{5.15}$$

as stated for example by Sommerfeld (2013). Following Eq. (5.15), τ_p is the time a particle needs to accelerate from rest to 63 % of the fluid velocity (Crowe et al., 2012) after a step-wise change in the relative velocity.

The characteristic time of the fluid τ_f is the ratio of a characteristic length to the relevant fluid velocity. Following Michaelides et al. (2017), the characteristic length can be the diameter d_p of spherical particles, which is often assumed for turbulent flows (Crowe, 2006). According to Kleinstreuer (2017), the tube diameter may be the key length supposing steady laminar particle suspension flow in a pipe, while, for a moving environment, it may be the tube length. Tsai and Pui (1990) apply the tube radius of bends as characteristic dimension and the average velocity as characteristic velocity. Here, the average fluid velocity and tube diameter are considered as characteristic, and the following correlation is applied

$$\tau_\mathrm{f} = \frac{4R}{v_\mathrm{f,max}}$$

For particles of a diameter of 20 µm, 50 µm, 100 µm and 400 µm, St in the Stokes regime is 0.004, 0.03, 0.1 and 1.6 for $v_\mathrm{f,low}$, and 0.006, 0.04, 0.2 and 2.5 for $v_\mathrm{f,high}$.

For $St \ll 1$, τ_p is much smaller than τ_f, and a particle responds quickly to changes in the fluid velocity. The particle velocity approaches the fluid velocity (Crowe et al., 2012). This is the case for particles of a size below approximately 50 µm. For $St \gg 1$, a particle does not respond or responds only slowly to changes in the fluid velocity. In this case, the particle movement is dominated by the convective flow and gravity following Kleinstreuer (2017). Here, even the largest particles do not reach these values, and they are still affected by the fluid through drag.

5.4.2 Variation of the Initial Particle Position

In the experiments, the glass bead fraction was distributed in the cross section of the tube. Therefore, in the single particle simulations, five different initial particle positions are compared, as depicted in Figure 5.3c. As visible in Figure 5.3a, an exemplary simulation at $v_\mathrm{f,max,low}$ reveals that, for a fixed particle size from 100 µm to 400 µm, and for different initial positions, the RTs deviate less than 1 % from the RT at the tube origin. Comparing initial positions in the upper half of the tube to the origin, as may be expected, the time until the first wall collision is longer, as illustrated in Figure 5.3b. For initial positions at the same vertical height like the origin, the first wall contact happens earlier. The difference is below 1 s, which is negligible compared to the overall RT. Hereafter, only the origin is considered as initial position. Hence, no horizontal particle movement in x-direction can be observed.

5.4.3 Variation of the Wall Collision Coefficients

In this section, the sensitivity of the RT to variations in the wall collision coefficients μ_c and e_c is discussed. The RT is determined by $v_{\mathrm{p},z}$, which depends on the collision coefficients according to Eq. (5.13c). In Eq. (5.13c), the second term is always negative or zero. After wall collision, the largest reduction in $v_{\mathrm{p},z}$ occurs when e_c is zero, in other words inelastic, and μ_c is large.

Typical values for the coefficients were listed in Table 5.1 and were taken from Groll (2015) for glass particles. The coefficients vary over a large range, not only depending on

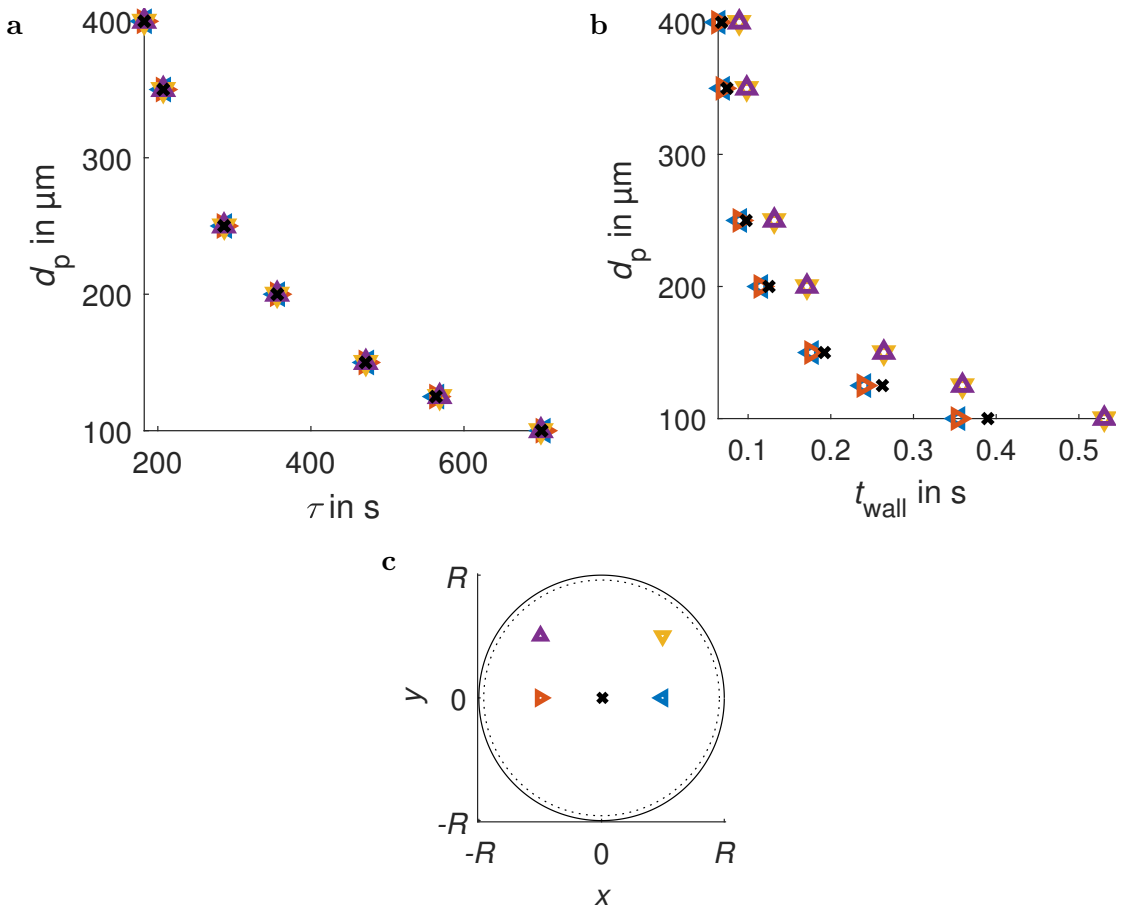

Figure 5.3: (a) RT and (b) time until first wall contact for particles of different size and initial position for $v_{f,max,low}$ and no initial particle velocity; (c) schematic of the cross section of the straight tube with initial particle positions (triangles or x-mark), tube wall (solid line), and position of particle center at wall contact (dotted line).

the material itself, but also on the surface roughness, which may change with material age. A typical value for the friction coefficient for soft glass on soft glass in air is one (Buckley, 1981). Lide (2004) gives a similar maximum value between glass and glass of 0.94 for the static coefficient of friction, and of 0.4 for the dynamic coefficient. For a rubber hemisphere sliding on glass, the sliding friction coefficient for dry conditions is about 2, for wet conditions it is about 0.8, and for elasto-hydrodynamic lubrication it is below 0.2 (Roberts and Richardson, 1981). Between polystyrene and polystyrene, a maximum value of 0.5 is reached for the static coefficient of friction (Lide, 2004). In general, the collision friction coefficient may also exceed one, but for the substances used here, and wet conditions, a limiting value of one is assumed.

Different combinations of values for the collision coefficients e_c and μ_c can be assumed as limiting cases. That is to say, $e_c = 0$ and $\mu_c = 1$ for perfectly elastic collisions, $e_c = 0.94$ and $\mu_c = 0$ for no friction collisions, $e_c = 0$ and $\mu_c = 1$ for inelastic high friction collisions, and $e_c = 0.94$ and $\mu_c = 0.325$ for typical collisions. For all these combinations of e_c and μ_c, simulations were performed with particles of 100 µm to 400 µm diameter. In all these cases, the second term in Eq. (5.13c) attributed to less than 1 % of the sum of the equation. The ratio $\left|\frac{v_{p,n}}{v_{p,z}}\right|$ was also smaller than 1 %. Therefore, the direct effect of the

collision coefficients on the horizontal velocity in Eq. (5.13c) is negligible.

The elasticity coefficient influences the cross-sectional velocity in Eqs. (5.13a) and (5.13b). It might be expected that perfect elasticity leads to higher bounces after collision and extends the overall RT, but this effect is, also, negligible. The RTs are shortened by less than 1 % from that for the selected coefficients in case of perfectly elastic collisions or no friction conditions. For the opposite limiting case of inelastic collisions and high friction, it may be expected that particles do not reflect from the wall but stay near the wall in regions of small fluid velocities, immediately after first wall contact. In this case, the RT increases by 12 % for 400 µm particles and by 5 % for 100 µm particles at $v_{\mathrm{f,max,high}}$, and, at $v_{\mathrm{f,max,low}}$, by 22 % for 400 µm particles and by 8 % for 400 µm particles.

5.5 Simulation Results

In this section, the simulated particle RTs are shown for different particle sizes and for both average fluid velocities, and they are compared to experiments. In the simulations, a decrease in particle size leads to an increase in RT for large particles of a size from 400 µm to 30 µm (see Figure 5.4). The opposite trend is observed for smaller particles. Very small particles of 5 µm diameter approach $v_{\mathrm{f,max}}$, which is the fluid velocity at the center of the cross section of the tube. The center is also the initial position of the particles. The RT of the largest particles approaches the average fluid velocity, where the RT of particles of 400 µm size is still three times as much as the average fluid RT. These qualitative trends appear for both average fluid velocities. Quantitatively, larger RTs are observed at $v_{\mathrm{f,low}}$, as expected. At $v_{\mathrm{f,low}}$, the maximum RT is observed between 12 µm and 20 µm as visible in Figure 5.4a, and, at $v_{\mathrm{f,high}}$, it is reached between 14 µm and 30 µm. In this range, the RTs were calculated for particles of 12 µm, 14 µm, 20 µm and 30 µm diameter.

Comparing experiments to simulations, the curves in Figure 5.4 are qualitatively similar and the RT of the glass beads also reaches a maximum. The glass bead size at which the maximum is reached is larger in the experiments. It is between 92 µm and 116 µm at $v_{\mathrm{f,low}}$ and between 108 µm and 132 µm at $v_{\mathrm{f,high}}$. The simulations overestimate the maximum RT. Considering the large particles, at $v_{\mathrm{f,high}}$, the particle RT is overestimated, whereas at $v_{\mathrm{f,low}}$, the RT is underestimated.

In all curves in Figure 5.4, a maximum RT was observed at intermediate sizes and very large and small crystals approached the fluid RT. In the following, this section discusses what kind of particle movement leads to this behavior, while the next sections investigate the forces causing this trend.

Particle trajectories near the tube inlet are shown in Figure 5.5a. They indicate that the overall residence time is a sum of the duration of a first phase, in which a particle approaches the wall and, a second phase, in which a particle travels directly along the wall. Comparing particles of large size with particles of smaller size, large particles sink to the wall more quickly. Large particles spend less time in the first phase and travel for a smaller axial distance near the tube center. In the straight tube, Hagen-Poiseuille flow was assumed and the axial fluid velocity decreases from tube center to tube wall. At the wall, the center of gravity of the larger particles is further away from the wall where higher fluid velocities prevail. Hence, in the second phase, large particles travel with higher velocities than small particles (see Figure 5.5b). For both, large and small size particles in the size range that was considered in the experiments, the first phase is short, which means below a few seconds, and the overall residence time is determined by the duration of the second phase. In the second phase, large particles are faster and their

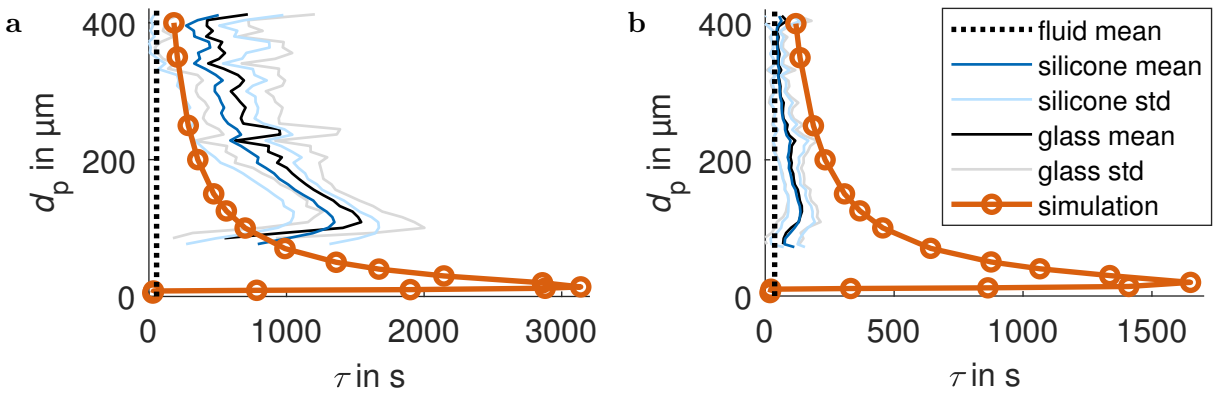

Figure 5.4: Simulated particle RT (orange with circle markers) and experimental RT of glass beads (dark blue and black, solid curves) with standard deviation (bright blue and gray, solid). Straight tubes consisting of silicone (dark and bright blue, solid) or glass (black and gray, solid). Shown for different average fluid RTs (black, dotted, vertical): (a) $v_{f,low}$ and (b) $v_{f,high}$. For each tube material, the experimental results are averaged over all beads that were observed in all experiments in Figure 3.2. The beads were classified in bins of 8 µm width in sphere diameter d_p to calculate the average and standard deviation of the RT for each bin.

residence time is lower. This explains the experimental observations. The simulations indicate, in Figure 5.4, that, for even smaller particles, below the experimental sizes, the residence time decreases further. When the particles are sufficiently small, they do not reach the second phase or, in other words, the wall before leaving the tube. This is confirmed by the Stokes number of these very small particles, which suggests that they follow the fluid flow easily. Particles that are 8 µm in size or smaller for $v_{f,low}$, and 10 µm in size or smaller for $v_{f,high}$ do not touch the lower wall before leaving the tube. The RT of a particle of 8 µm diameter is 33 s for $v_{f,low}$, and 19 s for $v_{f,high}$. The ratio of the RTs is similar to the inverse of the average fluid velocities. This is comprehensible, since the force of gravity is identical in both cases, but the distance, which a particle travels in a

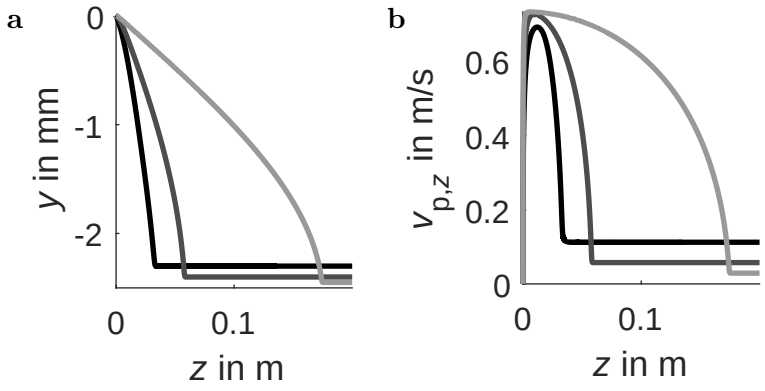

Figure 5.5: Simulated particle movement along the tube axis z for particles starting with zero velocity at the tube origin in a fluid at $v_{f,low}$. Particles with a d_p of 400 µm (black), 200 µm (gray), and 100 µm (bright gray). (a) Trajectory in the yz-plane; (b) axial particle velocity.

certain time, changes because of the difference in the velocity field.

Although the tube length was not varied in the simulations, some conclusions can still be derived. All particles that have a diameter of at least 50 µm reach the lower tube wall within 1.5 s and within an axial distance z =1 m at both fluid velocities. Their traveled distance until wall contact is short. They reach a constant $v_{\mathrm{p},z}$ quickly. For those large particles the RT should increase approximately linearly with tube length. For smaller particles, the increase will exceed the linear one because the particles need a significant time to sink to vertical positions of lower fluid velocity.

The results confirm the findings of Matas et al. (2004) for smaller density differences, smaller tube length to diameter ratios, and similar pipe to particle diameter ratios, for particles of a diameter of 100 µm to 400 µm. The particles that were heavier than the fluid assembled at the bottom of their ducts.

5.5.1 Effect of the Saffman Force and the Correction Factors

In this section, the effect of the Saffman force and of the Saffman and Goldman correction factors on the particle RT and on the particle movement is investigated. First, it analyzes what effect f_{G} in Eq. (5.8) has, compared to setting it to one. When the Goldman correction is not considered for the drag coefficient, the particle bounces much higher after the first wall collision than in the full model, where f_{G} is applied, as visible in Figure 5.6a. It bounces up by less than 0.01 % of the tube radius when f_{G} is used, and by less than 4.4 % when f_{G} is set to one. For smaller particles, the bounce is even lower. The Goldman correlation leads to an increased drag coefficient, and to an increased drag force near the wall. When a particle approaches the lower wall during sinking, it experiences attenuation and its absolute velocity decreases as shown in the beginning of the orange curve in Figure 5.6b,c. When the Goldman correction is applied, the time and traveled distance until first wall contact increase. Nevertheless, the influence on the overall RT is negligible. For both models, $v_{\mathrm{p},z}$ already reaches a similar value after approximately 0.1 s, in Figure 5.6c. The figure also illustrates that the axial velocity in the z-coordinate is not increased after a wall contact, but the decrease in $v_{\mathrm{p},z}$ indicates it is only slowed down slightly. For particles in the range of 50 µm to 400 µm, the deviation in the RT between the two models increases with a decrease in the particle size. For the smallest particle, the deviation is 0.1 % at both fluid velocities.

Compared to the full model, when the Saffman correction is set to one, the difference in RT is below 0.02 % for all investigated particle sizes. When the Saffman force is completely disregarded, the deviation is also very small, and still below 0.1 % at both fluid velocities. Overall, the inclusion of the Saffman force and the Saffman and Goldman correction factors does not have a significant influence on the RT. The simulated RT is mainly determined by gravitation and drag force. This confirms the importance of the interplay of drag force and velocity profile curvature, which was already highlighted by Matas et al. (2004) for their horizontal tube. They further suspected an effect of the Saffman's lift force for non-neutrally buoyant particles, which was, by contrast, negligible here.

The following sections analyze how different simulation parameters affect the particle RTs.

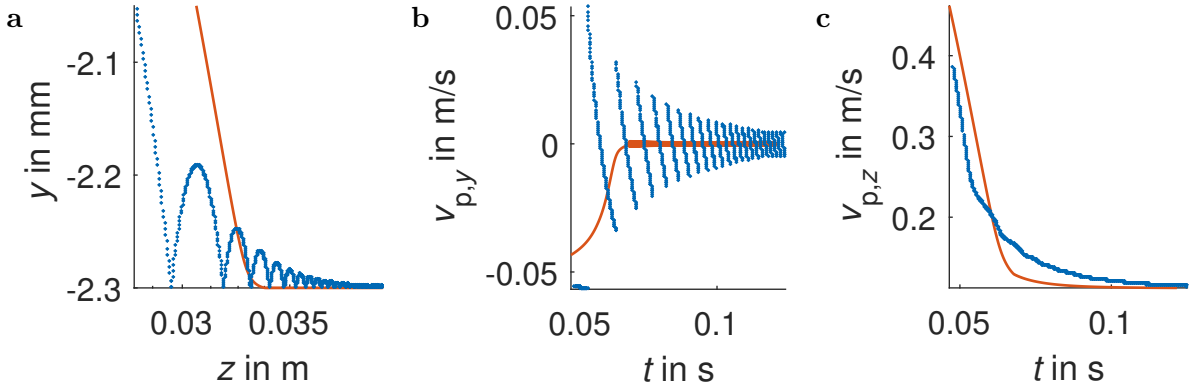

Figure 5.6: Movement of a particle of 400 µm diameter starting at the tube origin at $v_{f,low}$ for the full model (orange, solid) and for the model without Goldman correction of the drag force (blue, markers): (a) vertical cross section of the tube at $x = 0$ for a range of z close to the location of the first wall contact; (b) vertical velocity and (c) horizontal velocity for the same time range as in part a of this figure.

5.5.2 Variation of the Fluid Velocity

The values for $v_{f,max}$ in Table 5.1 were calculated from mass flow measurements based on the tube geometry. The measurements were taken during running experiments; hence, the values should be rather accurate. Predictions for further fluid velocities are shown in Figure 5.7. As expected, the fluid velocity has a negative effect on the particle RT.

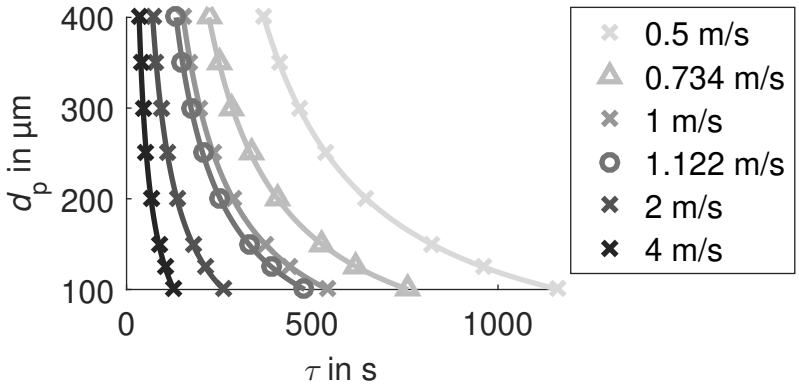

Figure 5.7: Simulated particle RTs for different $v_{f,max}$ of the Hagen-Poiseuille profile, as illustrated in the legend. Maximum fluid velocities decrease from dark to bright gray.

When the maximum fluid velocity is halved, the particle RT is increased by a factor of approximately two, for all particle sizes in Figure 5.7. The factor of increase is a little higher for larger particles and small values of $v_{f,max}$. To be more precise, when $v_{f,max}$ is decreased from $1\,\mathrm{m\,s^{-1}}$ to $0.5\,\mathrm{m\,s^{-1}}$ for a particle of 400 µm diameter, the RT increases by a factor of 2.42. For $v_{f,max}$ decreasing from $4\,\mathrm{m\,s^{-1}}$ to $2\,\mathrm{m\,s^{-1}}$ for a particle of 100 µm diameter, the RT increases by a factor of 2.05. Hence, the change in particle RT is nearly inversely proportional to the change in $v_{f,max}$ in the considered range of particle sizes and fluid velocities. This is the case because the considered, rather large, particles move near the wall for almost their entire RT. Close to the wall, the fluid velocity may be approximated linearly.

The particle-to-fluid RT ratio becomes smaller, the higher the fluid velocity. For example, for large particles with a d_p of 400 µm, the ratio is 3.3 at $v_{f,max}$ =4 m s^{-1} whereas it is 4.5 at 0.5 m s^{-1} and at a d_p of 100 µm, the ratio is 12.4 at $v_{f,max}$ =4 m s^{-1} whereas it is 14.2 at 0.5 m s^{-1}. On the one hand, the smallest difference in RT and the best mixing is observed at higher fluid velocities. On the other hand, a size-dependent particle RT is observed at all fluid velocities with a $v_{f,max}$ from 0.5 m s^{-1} to 4 m s^{-1}, such that the fluid velocity should be selected on the basis of the required time for crystal growth, assuming that the tube length is fixed.

5.5.3 Variation of the Particle Density

The model can be applied for predictions of the RT of further substances. In this case, a different particle-to-fluid density ratio may apply. Predictions for further particle densities at fixed fluid density and viscosity are depicted in Figure 5.8. Similar effects are observed

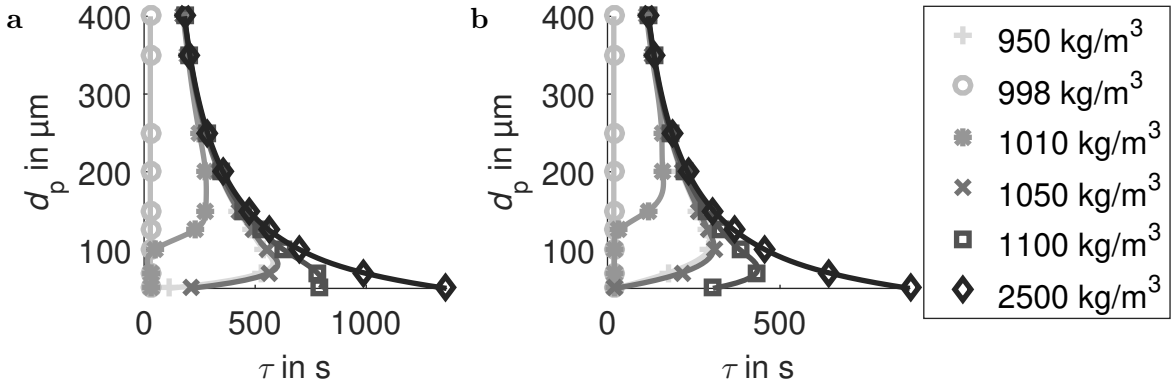

Figure 5.8: Simulated particle size over RT for varying particle density ρ_p at fixed fluid density and viscosity: (a) $v_{f,low}$ and (b) $v_{f,high}$. The legend in part b of the figure applies for both parts and shows ρ_p. The ode45 MATLAB solver was used to calculate all RTs.

when ρ_f is varied at a fixed ρ_p. For the given setup, the values for ρ_f and ρ_p in the model may deviate slightly from the assumed values, due to temperature variations or due to deviations in the fabrication of the glass beads. Small differences do not significantly influence the RT. Even if larger differences appeared, a variation of the particle density would not improve the agreement of the simulated data with the experiments.

In crystallization most density ratios are in the depicted range. For example, for potash alum in water, the density difference and, hence, the particle RTs are between the two curves for the largest densities in Figure 5.8. For other substances and solvents, the dynamic viscosity may change significantly. In this case, the kinematic viscosity could be taken into account, instead of the particle density. During crystallization, the change in the fluid density should be negligible in most applications.

A limiting case occurs when the fluid and particle density are identical, in particular, when ρ is 998 kg m^{-3} in Figure 5.8. The particles are neutrally buoyant and no vertical movement is caused by gravitational force. When a particle starts from the center of the circular cross-section of the tube, or in other words x and y are zero, the particle remains at a radius of zero and it moves with the maximal fluid velocity $v_{f,max}$. Hence, the lowest RT is reached, compared with other density ratios in Figure 5.8. When the density ratio increases, the particle size at which the maximum RT is reached decreases,

and the limiting size of the small particles at which the fluid RT is reached decreases. The RT of larger particles remains nearly unchanged. A deviation of ρ_p from ρ_f by the same absolute value above and below the original ρ_p leads to the same RT. The same qualitative behavior is observed for $v_\mathrm{f,low}$ and for $v_\mathrm{f,high}$.

A crystal population is initially distributed in the cross section of the tube. For a density ratio approaching zero and perfect Hagen-Poiseuille flow in a straight tube, neutrally buoyant particles remain at their initial radial position. Very heterogeneous RTs result, which depend more on the initial position than on the particle size.

In a HCT, radial forces appear and the dependence on the initial position disappears. Particles move to different radial locations, depending on their size, and remain there. These radial positions may depend on the density difference. The dependence is probably nonlinear, because of the complex radial fluid velocity profile. The radial positions are correlated with different axial velocities and particle RTs.

The simulations agree qualitatively with literature. Baptista et al. (1996b) reported a settling effect, where denser particles move closer to the tube wall when the fluid velocity is lower. Simulations by Matas et al. (2004) confirmed the particle movement towards the lower part of the tube. For a particle density deviating less than 0.1 % from the fluid density, they found that particles moved towards the tube bottom for low Reynolds numbers of $Re = 170$, but not for higher Reynolds numbers of $Re = 390$. For a slight increase of the particle-to-fluid density difference to 0.2 %, they could not observe the difference with Reynolds number anymore, and the particles assembled mainly at the tube bottom in both cases.

5.6 Model Extensions

The applied model assumptions were listed in Section 5.2. The influence of unsteady forces seemed to be significant, but exceeds the scope of this study. The discussion also suggested that the rotation of the particles may cause a significant lift. In the following, the effect of the lift force on the particle RT is estimated. It is calculated which angular velocities are required to change the simulation results and it is assessed whether that change would improve the agreement between experiments and simulations in Figure 5.4. Furthermore, the application of the model and the simulation results to an HCT are reviewed.

5.6.1 Limits of the Angular Velocity

The change in the angular particle velocity can be modeled by an angular momentum balance. Such a balance describes the torque acting on a particle resulting from friction forces, when a particle rotates with an angular velocity relative to the surrounding fluid. The torque can change by interaction with the fluid, or by collisions, for example with the wall. For Stokes flow, Happel and Brenner (1983) describe the torque of a sphere. Redlinger-Pohn et al. (2016a) use a splitting technique of the coupling forces and torques in an open-source CFD-DEM implementation of fibers. They state the implemented Newton's equation of the rotational motion. A wall reflection model is proposed by Crowe et al. (2012), which describes the limit of rolling and sliding, after a particle reaches a flat wall. Their conditions and coefficients for elastic collisions differ from a reflection model proposed by Groll (2015). The implementation of the wall reflection model, including directions of the linear and angular velocity, becomes complex when transferring it to

a tubular wall. If a particle is not reflected upon collision, wall friction may have a major effect on the sliding or rolling behavior of particles. When the tube walls become rough or the particles become angular, as is the case for crystals, the results may not be transferable. An angular momentum balance is not implemented, because it would require a reliable wall collision model.

Rolling and sliding on a wet tube wall might not strongly affect the axial particle velocity directly, but may lead to large deviations in the Magnus lift force. A rotating particle carries along some part of the surrounding fluid. Because of the relative particle movement, the entrained fluid moves with or against the fluid, at the outer sides of the particle. In Figure 5.9a, the entrained fluid at the upper part of the particle moves against the surrounding fluid, and pressure increases locally. At the lower part, the entrained fluid flows with the bulk fluid, and the local pressure is reduced. A lift force towards the lower pressure, that is to say, towards the bottom, results. When the particle turns the other way around, the particle is lifted upward as shown in part b of the figure. The resulting force acts perpendicular to the relative linear velocity of the particle, and to the axis of the relative angular velocity.

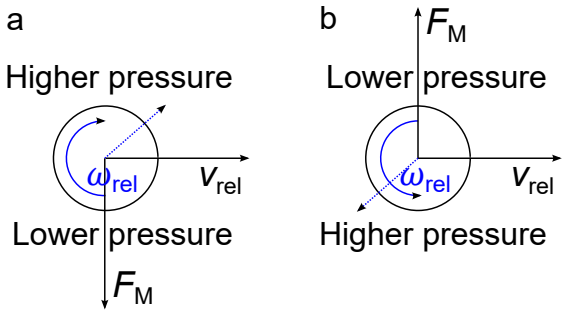

Figure 5.9: Direction of the Magnus force for a spherical particle in dependence of its relative linear velocity and its relative angular velocity.

Following Rubinow and Keller (1961), the Magnus force is based on the cross product of the relative rotational velocity and the relative linear velocity

$$\mathbf{F}_\mathrm{M} = \frac{\pi}{8} d_\mathrm{p}^3 \rho_\mathrm{f} f_\mathrm{M} \boldsymbol{\omega}_\mathrm{rel} \times \mathbf{v}_\mathrm{rel} \tag{5.16}$$

where the relative angular velocity is

$$\boldsymbol{\omega}_\mathrm{rel} = \frac{1}{2} \nabla \times \mathbf{v}_\mathrm{f} - \boldsymbol{\omega}_\mathrm{p}$$

and where $\boldsymbol{\omega}_\mathrm{p}$ is the angular velocity of the particle. Another typical form of the Magnus force equation can be derived when the angular fluid velocity is disregarded as typically assumed in stagnant fluid (Crowe et al., 2012). For Hagen-Poiseuille flow, Eq. (5.16) becomes

$$\mathbf{F}_\mathrm{M} = \frac{\pi}{8} d_\mathrm{p}^3 \rho_\mathrm{f} f_\mathrm{M} \begin{pmatrix} -v_{\mathrm{p},y}\omega_{\mathrm{p},z} + (v_{\mathrm{p},z} - v_{\mathrm{f},z}) \left(\frac{1}{2} \frac{\partial v_{\mathrm{f},z}}{\partial x} + \omega_{\mathrm{p},y} \right) \\ v_{\mathrm{p},x}\omega_{\mathrm{p},z} + (v_{\mathrm{p},z} - v_{\mathrm{f},z}) \left(\frac{1}{2} \frac{\partial v_{\mathrm{f},z}}{\partial y} - \omega_{\mathrm{p},x} \right) \\ v_{\mathrm{p},y} \left(\omega_{\mathrm{p},x} - \frac{1}{2} \frac{\partial v_{\mathrm{f},z}}{\partial y} \right) + v_{\mathrm{p},x} \left(-\frac{1}{2} \frac{\partial v_{\mathrm{f},z}}{\partial x} - \omega_{\mathrm{p},y} \right) \end{pmatrix} \tag{5.17}$$

In Eqs. (5.16) and (5.17), f_M is the correction factor of the Magnus lift force for higher Reynolds numbers. Rubinow and Keller (1961) derived the equation for small Reynolds

numbers, where f_M is one. Sommerfeld (2013); Michaelides et al. (2017) suggest to use an expression for the correction factor f_M of the Magnus force at higher Reynolds numbers that was derived by Oesterlé and Dinh (1998)

$$f_\mathrm{M} = 0.45\frac{Re_\mathrm{p}}{Re_\mathrm{r}} + \left(1 - 0.45\frac{Re_\mathrm{p}}{Re_\mathrm{r}}\right)\exp\left(-0.057 Re_\mathrm{r}^{0.4} Re_\mathrm{p}^{0.3}\right) \tag{5.18}$$

where the Reynolds number of rotation is

$$Re_\mathrm{r} = \frac{\rho_\mathrm{f} d_\mathrm{p}^2 \left|\frac{1}{2}\nabla \times \mathbf{v}_\mathrm{f} - \boldsymbol{\omega}_\mathrm{p}\right|}{\eta_\mathrm{f}}$$

The expression is based on their own measurements, for Re_p up to a value of 140. Following their comparison with experiments from literature, the correlation is applicable for values up to 2000. The correction factor from Eq. (5.18) is shown in Figure 5.10. As expected, for small Re_p, f_M approaches one, and the correlation by Rubinow and

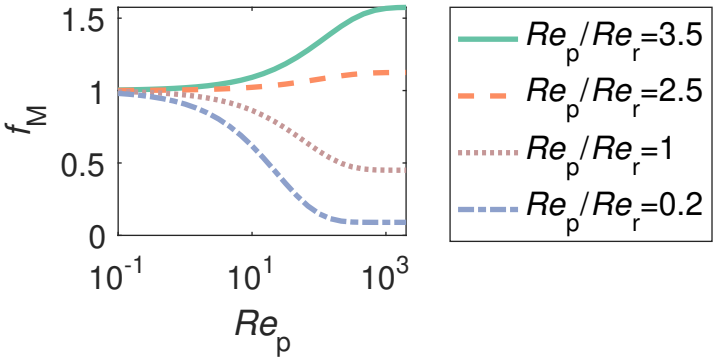

Figure 5.10: Magnus force correction factor f_M for different ratios of the particle Reynolds number Re_p to the rotational Reynolds number Re_r and for varying Re_p at $v_\mathrm{f,low}$.

Keller (1961) is fulfilled. In the transient and turbulent regime, different reported experiments determining the lift coefficient in dependence of the angular velocity do not agree, according to Crowe et al. (2012).

The Magnus force is implemented in the linear momentum balance. The particle movement is simulated, including the Magnus force for different constant angular particle velocities. It is assumed that particles touch the tube wall close to the tube bottom, and that this collision causes, mainly, a rotation around the x-axis. The results are shown in Figure 5.11. Figure 5.11a shows that the particle RT is affected significantly, as soon as the constant angular velocities around the x-axis exceed an absolute value of 1000 rad s^{-1}. The threshold of the angular velocity is similar for both particle sizes. When the Magnus force is included, the particles need more time to reach the tube bottom, due to the lift, and travel a larger distance before they reach the tube bottom, as illustrated in Figure 5.11b,c. As soon as particles collide with the lower wall, their angular velocity becomes negative, and the left part of Figure 5.11 applies.

As discussed above, the angular velocity of a particle can change when a torque is acting. Following Sommerfeld (2013), the torque depends on the density of the fluid, the particle diameter, and on the Reynolds number of rotation, which again depends on the dynamic viscosity of the fluid. These are also the parameters on which the Magnus force depends. Baptista et al. (1996b) performed experiments in straight tubes. The parameters

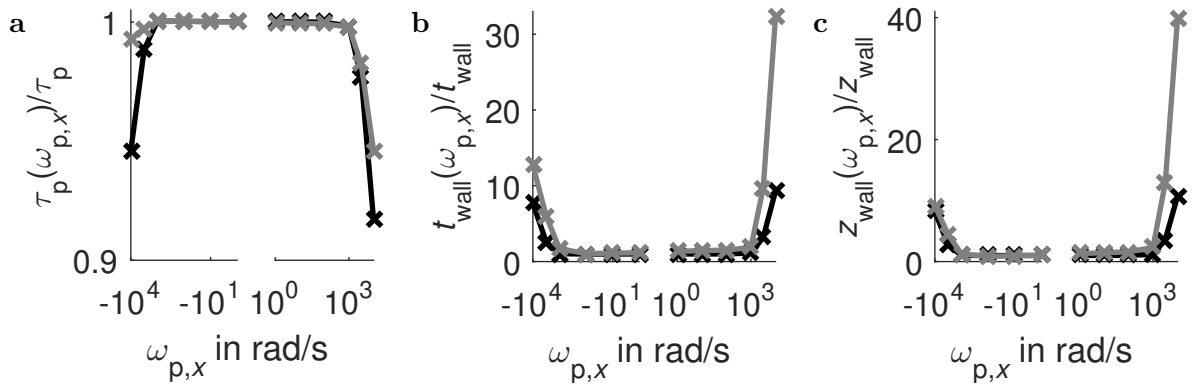

Figure 5.11: Simulation results for the particle movement including the Magnus force relative to simulations without the Magnus force for varying constant angular velocity $\omega_{\mathrm{p},x}$ illustrated on a logarithmic scale. Particles of a diameter of 100 µm (black) and 400 µm (gray) start at the tube origin with zero linear velocity and zero angular velocity around the y, z-axes at $v_{\mathrm{f,low}}$: (a) RT; (b) time of the first wall contact; (c) axial location of the first wall contact.

that affected the particle rotational velocity most significantly in their investigations were particle diameter, fluid viscosity, and particle density. While a particle moves towards the tube bottom, it travels through a fluid velocity gradient, which may change its angular velocity. At the very latest, when a particle collides with the tube wall, its angular velocity will change. A constant angular velocity is probably far from reality for most initial values of the angular velocities. Nevertheless, the effect of different constant angular velocities was simulated, to identify what speed the particle rotation has to reach, to have a bearing on the particle RT in the tube.

On the one hand, the Magnus force increases with the cross-sectional area of a particle. On the other hand, according to Sommerfeld and Kussin (2003), the angular velocity caused by a wall collision is inversely proportional to the particle diameter. They state that near a wall, the angular velocities are higher for smaller particles. Baptista et al. (1996b) also found that larger particles slide more than smaller particles.

Sommerfeld and Kussin (2003) simulated particles in a similar size range, but of large Stokes numbers, in a relatively wide horizontal channel. In a smooth tube, they observed angular velocities as low as $-10\,000\,\mathrm{rad\,s^{-1}}$, as simulated here. In rough tubes they observed angular velocities in the range of $-20\,000\,\mathrm{rad\,s^{-1}}$ to $15\,000\,\mathrm{rad\,s^{-1}}$, depending on the vertical location of the particles and on the mass loading.

In this range of angular velocities, the Magnus force had a significant effect on the RT in this study. The effect was relatively larger for particles of a diameter of approximately 100 µm, compared with 400 µm. Especially in the intermediate particle size range, the simulations without the Magnus force overestimated the RT (see Figure 5.4). It can be expected that the addition of an angular momentum balance and the Magnus lift force improves the agreement in the RT between experiments and simulation.

5.6.2 Extensions for the HCT

In this chapter, a straight tube was modeled and simulated. The same forces may cause particle-size-dependent RTDs in an HCT. In HCTs, too, different axial velocities exist at different positions in the circular-cross section. For HCTs, Tiwari et al. (2006) observed

that particles locate near the inner bend of the tubes. Further, the radial particle location changes with the Dean number, where the Dean number again depends on the particle size.

For an HCT, the fluid velocity profile is more complex, and a large radial velocity component develops. The fluid velocity profile was simulated by Wiedmeyer et al. (2017a). To extend the model that was developed in this chapter to HCTs, the velocity profile can be averaged over a certain range of the axial coordinate z, or it can be represented by the cross-sectional profile at a selected z. Wiedmeyer et al. (2017a) simulated the fluid flow in two coils. The selected axial position should be far from inlet and outlet. There, the selected location was at half the axial length of the second coil. A time average of such a simulated fluid velocity profile could be applied in an HCT model.

When a cylindrical coordinate system is applied, additional body forces, in particular the centrifugal force and the Coriolis force, must be considered (Sommerfeld, 2013).

Tiwari et al. (2006) simulate a two-phase flow, in full three-dimensional helical curved conduits, with a flow computer code. They state that the drag is usually dominant for particles of a size below 100 µm in dilute flows. Next to the drag force, they identify two main forces. In axial direction, they model the virtual mass force, and in radial direction they consider the lift force. According to them, for very small particles, of a size below 20 µm, the virtual mass force is negligible, compared with the drag force for fully developed laminar flow.

Following Crowe et al. (2012), the drag coefficient in Eq. (5.6) depends, inter alia, on particle shape, roughness of the surface, and compressibility and rarefaction of the fluid. Spherical particles were assumed, which is reasonable for glass beads. If the model had to be adjusted for octahedral potash alum crystals in the HCT, correlations are available. Gurel et al. (1955) performed experiments with octahedra and derived the settling velocity and an empirical correlation for the resistance of motion. Haider and Levenspiel (1989) give a correlation for non-spherical particles, based on the particle sphericity. Hölzer and Sommerfeld (2008) review several correlations for non-spherical drag coefficients, and compare them to experimental data. They propose to use the correlation of Haider and Levenspiel (1989) for octahedra. When the correlation for c_D by Haider and Levenspiel (1989) for octahedra is used, instead of the applied one by Schiller and Naumann (1933) for spheres, the drag coefficient increases by 55 % for the upper limit of $Re_\mathrm{p} = 447$, which was calculated in Section 5.4, and by 4 % for $Re_\mathrm{p} = 0.1$ in the Stokes regime. The order of deviation agrees with the order of deviation from experimental data, for the correlations that were reviewed by Hölzer and Sommerfeld (2008). The accuracy is especially good for the Stokes regime. This is the case if the particle velocity is close to fluid velocity. As this is assumed for most of the process time, the correlation of Schiller and Naumann (1933) in Eq. (5.8) would be appropriate for potash alum crystals.

One of the aims of the present study was to identify and parameterize a setup that can grow crystals of a narrow size. To avoid a broadening of the CSD of a crystal population during the process, a narrow particle RTD is often advantageous. A uniform particle RT can also be achieved by other means, for instance when the fluid velocity is increased, when the particle size range is narrow, or by a change in the experimental setup. Besenhard et al. (2014b) experimentally realized a slug flow operation mode to employ a constant crystal RT. Saxena and Nigam (1984); Klutz et al. (2015); Hohmann et al. (2016a) implemented a CFI that consists of bent HCTs to improve mixing and to approach plug flow.

5.7 Summary of the Chapter

The movement of a single particle was modeled in a straight tube, to improve the physical understanding of the size dependency of the particle RT. A momentum balance model reproduced size-dependent RTs. The dominant forces causing the size dependency were the gravity and buoyancy force and the drag force in combination with the Hagen-Poiseuille fluid velocity profile. The Saffman lift force had only a minor effect on the RT.

One aim of this chapter was to understand how parameters enhance or impede a size dependency of the particle RT. The collision coefficients and, hence, the wall material have a minor effect on the RT. This is supported by the experiments, where similar results were observed in glass and silicone pipes. The effect of the applied particle material was also estimated by the density difference between particle and fluid. Buoyant particles follow the flow, as expected. Nevertheless, their RTD is not uniform, but depends on their radial starting position in Hagen-Poiseuille flow, for a straight tube. For an HCT, it is expected that the RTs are rather uniform for neutrally-buoyant particles independently of their initial position. In HCTs, there is a radial motion that leads to an accumulation of particles at similar radial positions. As soon as the particles are non-neutrally buoyant, the RT of the largest particles is independent of a density difference. The RT of intermediate-size and small particles increases with the density difference. From a density ratio of 1.5 on, the increase in the RT becomes minor. Another parameter, which is related to the operation, is the average fluid velocity. When the average fluid velocity was doubled, the particle RT nearly halved. The decrease in the RT was stronger for intermediate-size particles, than for the largest particles. This means that the RT becomes more uniform with an increase in the average fluid velocity.

Qualitatively, the simulations agreed with the experiments where large and very small particles have small RTs, and intermediate-size particles have large RTs. Quantitatively, the RT of particles of intermediate size was overestimated in the simulations. For the large particles, the simulations underestimated the RT at a low fluid flow rate, but overestimated the RT at a high fluid flow rate. For a better agreement between experiments and simulations, model adaptions have been proposed. The addition of an angular momentum balance seemed promising for single particle simulations. In the experiments, a whole particle population was used. Experiments have shown some small change in the RT, depending on the type of the particle distribution for dilute suspensions. To extend this dissertation, particle populations could be studied with advanced numerical methods considering two-way or even four-way coupling in a CFD simulation. It seems that this is still missing in literature, for non-neutrally buoyant particle populations, in circular channels of similar dimensions, especially for a range of a particle-to-tube diameter of 1 % to 10 %.

6 Model and Simulations of a Crystal Population in an HCT

In Chapter 5, the movement of a single particle was derived from first principles. Here, a phenomenological model is derived to describe the movement and crystallization of a whole population in the HCT.

The model provides insight into the HCT along the tube, while experimental measurements are limited to certain tube positions. Model simulations can be used for process design. Downstream processes, product quality, and yield are influenced by the product CSD and also by the product crystal mass. Hence, the simulation results are evaluated regarding these criteria. The criteria are influenced by parameters, inlet and boundary conditions, e.g., flow rates, size-dependent crystal RT, seed distribution, and temperature. Their effect is estimated from simulations. Furthermore, simulations allow to make predictions for conditions that were not tested experimentally. Conditions that are closer to industrial applications are identified and limits can be tested, for example for higher suspension densities, for continuous crystallization with continuous seeding, and for a dynamic start up.

The questions to be answered in this chapter are:

1. Is a simplified model for the particle velocity, where all crystals have an identical velocity, sufficient to predict the product CSD?
2. Which geometry and process parameters lead to large product crystals, narrow CSDs, a high product mass, and a high yield? In particular:
   a) How much should the tube be extended?
   b) When should lower and higher flow rates be preferred, respectively?
   c) How does the seed mass and the width of the seed distribution affect crystal growth?
   d) How does cooling affect crystal growth?
3. What can be expected for continuous seeding?

The structure of this chapter is as follows. Relevant crystallization phenomena and parameter ranges are identified from the experiments in Chapter 4. A population balance equation (PBE) system is developed and discretized via the finite volume method (FVM). The resulting model and its empirical relationships are parameterized on the basis of these experiments and literature. For that purpose, the dispersion coefficient of the fluid phase is determined, a correlation for the size-dependent crystal velocity is derived from no-growth conditions at selected flow rates, and an appropriate growth kinetic for potash alum is identified from literature. Next, growth simulations are shown and validated by experiments. Finally, results of continuous crystallization processes are predicted as mentioned above.

6.1 Population Balance Equation System

In the HCT, crystals are distributed in a multidimensional space. The independent variables are the time t, the external spatial coordinate vector $\mathbf{r}$, and the internal property coordinate vector $\mathbf{h}$. In the model, which is developed in this chapter, the movement of the crystals along the axial coordinate z of the vector $\mathbf{r}$ is investigated. The internal property coordinate vector $\mathbf{h}$ comprises the perpendicular distances of the different types of faces of a crystal from the crystal center, as depicted in Figure 4.1. For potash alum, only one internal coordinate h is considered, but the framework of equations can be analogously applied for multivariate substances.

One aim of this chapter is to predict the dynamic evolution of the CSD in the HCT. It can be modeled with a PBE. The dimension of the PBE is increased compared with the continuous phase balances due to the internal coordinate. The method of moments (Hulburt and Katz, 1964) can be used to reduce the dimension of the PBE and the complexity of the solution. There are constraints under which moment equations can be obtained and problems appear when the equations are unclosed (Ramkrishna, 2000). The equations do not close when the growth rate is nonlinearly dependent on the crystal size (Ramkrishna, 2000; Myerson, 2002) or when destruction of fine particles appears (Myerson, 2002). The reduction is often applied when information on average particle number, size, their variance, and skewness are sufficient. If the internal coordinates appear in the equations of motion, the method of moments is no longer exact (Hulburt and Katz, 1964). Here, the method of moments is not applied, but the PBE is used to describe the evolution of the entire CSD.

The model couples a PBE for the dispersed phase and mass balance equations for the continuous phase. The PBE includes spatial convection and growth. Aggregation and breakage are not considered in the source term as they were negligible in the experiments, which were shown in Section 4.3.3. Nucleation is also neglected as the nuclei were distinguishable by their size from grown seed crystals and nucleation was limited for experiments at low supersaturation in Section 4.3.3. Furthermore, nucleation is not supposed to influence the supersaturation to a large extent. The structure of the terms for the convection in the external coordinate space and for the growth and dissolution term in the internal coordinate space are identical. Growth rate dispersion is not taken into account, but could be modeled as hydrodynamic dispersion in the h-coordinate. The general multivariate formulation of the PBE is

$$\frac{\partial f}{\partial t} + \nabla_{\mathbf{h}} \cdot (\mathbf{G} f) + \nabla_{\mathbf{r}} \cdot (\mathbf{v}_{\mathrm{p}} f) = 0$$

where $f(\mathbf{h}, \mathbf{r}, t)$ is the crystal number density, $\mathbf{G}(\mathbf{r}, t)$ is the growth or dissolution rate, and $\mathbf{v}_{\mathrm{p}}(\mathbf{h})$ is the crystal velocity. For size-independent growth of univariate potash alum and a location-independent particle velocity along the length z of the HCT, the PBE becomes

$$\frac{\partial f}{\partial t} + G\frac{\partial f}{\partial h} + v_{\mathrm{p}}\frac{\partial f}{\partial z} = 0 \tag{6.1}$$

Initially, there are no crystals in the HCT for continuous seeding

$$f_{\mathrm{conti}}(h, z, t = 0) = 0 \tag{6.2a}$$

whereas there are initially crystals for batch seeding, and at the tube inlet $z_{\min}$, the initial condition is nonzero

$$f_{\text{batch}}(h, z > z_{\min}, t = 0) = 0 \tag{6.2b}$$
$$f_{\text{batch}}(h, z_{\min}, t = 0) = f_{\text{in}} \tag{6.2c}$$

In the external coordinate space, the Dirichlet boundary condition at the inlet for continuous seeding is

$$f_{\text{conti}}(h, z_{\min}, t) = f_{\text{in}} \tag{6.3a}$$

For a batch-wise addition of seeds, initially, the same condition applies, but no crystals are fed for $t > 0$

$$f_{\text{batch}}(h, z_{\min}, t_0) = f_{\text{in}} \tag{6.3b}$$
$$f_{\text{batch}}(h, z_{\min}, t > 0) = 0 \tag{6.3c}$$

The following condition applies in the internal coordinate space at the lower bound for growth conditions

$$f(h_{\min}, z, t) = 0 \tag{6.4a}$$

In case of dissolution, the following boundary condition applies

$$f(h_{\max}, z, t) = 0 \tag{6.4b}$$

assuming that all crystals are of size $h_{\min} \leq h \leq h_{\max}$.

For the applied conditions, potash alum crystallizes as dodecahydrate. Hence, two mass balances are required for the continuous phase, in particular, one for the anhydrous potash alum and one for water. The fluid phase is transported in z by convection and dispersion. The continuous and dispersed phases are coupled by growth and dissolution. The term corresponding to the mass transfer is

$$\frac{\mathrm{d}m_{\text{p}}}{\mathrm{d}t} = \int_{h_{\min}}^{h_{\max}} \frac{\mathrm{d}m_{\text{crystal}}}{\mathrm{d}t} f \,\mathrm{d}h$$

where m_{crystal} is the mass of a single crystal. Applying the crystal density and volume, the equation becomes

$$\begin{aligned}\frac{\mathrm{d}m_{\text{p}}}{\mathrm{d}t} &= \int_{h_{\min}}^{h_{\max}} \rho_{\text{p}} \frac{\mathrm{d}\left(k_V h^3\right)}{\mathrm{d}t} f \,\mathrm{d}h \\ &= k_V \rho_{\text{p}} \int_{h_{\min}}^{h_{\max}} 3h^2 \frac{\mathrm{d}h}{\mathrm{d}t} f \,\mathrm{d}h \\ &= 3 k_V \rho_{\text{p}} \int_{h_{\min}}^{h_{\max}} h^2 G f \,\mathrm{d}h\end{aligned}$$

The term has to be divided into a part for the anhydrate in solution and a part for the water in solution. In case of growth, an increase in crystal mass reduces the mass in the

continuous phase and for dissolution it is vice versa. Hence, the term is modeled as a sink. The resulting continuous phase mass balance equations are

$$\frac{\partial m_{\mathrm{f,anh}}}{\partial t} = -v_{\mathrm{f}}\frac{\partial m_{\mathrm{f,anh}}}{\partial z} + D\frac{\partial^2 m_{\mathrm{f,anh}}}{\partial z^2} - 3\chi_{\mathrm{anh}}k_V\rho_{\mathrm{p}}\int_{h_{\min}}^{h_{\max}} Gh^2 f \,\mathrm{d}h \tag{6.5}$$

$$\frac{\partial m_{\mathrm{f,w}}}{\partial t} = -v_{\mathrm{f}}\frac{\partial m_{\mathrm{f,w}}}{\partial z} + D\frac{\partial^2 m_{\mathrm{f,w}}}{\partial z^2} - 3\left(1-\chi_{\mathrm{anh}}\right)k_V\rho_{\mathrm{p}}\int_{h_{\min}}^{h_{\max}} Gh^2 f \,\mathrm{d}h \tag{6.6}$$

where $m_{\mathrm{f,anh}}$ is the mass of the anhydrate and $m_{\mathrm{f,w}}$ is the total mass of water in the fluid phase, v_{f} is the average velocity of the fluid phase, D is the dispersion coefficient of the fluid phase assuming that water and potash alum can be characterized by the same coefficient, χ_{anh} is the molar mass ratio of the anhydrate ($\mathrm{KAl(SO_4)_2}$) in the crystalline phase ($\mathrm{KAl(SO_4)_2 \cdot 12H_2O}$)

$$\chi_{\mathrm{anh}} = \frac{M_{\mathrm{anh}}}{M_{\mathrm{hyd}}}$$

and k_V is the volume shape factor of the perpendicular face distance of an octahedral potash alum crystal

$$k_V = 4\sqrt{3}$$

The volume shape factor k_V can be derived from the edge length of an octahedron which is $\sqrt{6}h$ or from the radius of a sphere with equivalent volume where the radius is $(3\sqrt{3}/\pi)^{1/3}h$. At the HCT inlet, the following Dirichlet boundary conditions apply

$$m_{\mathrm{f,anh}}\left(z = z_{\min}, t\right) = m_{\mathrm{f,anh,in}} \tag{6.7a}$$

$$m_{\mathrm{f,w}}\left(z = z_{\min}, t\right) = m_{\mathrm{f,w,in}} \tag{6.7b}$$

Initially, the mass of anhydrate and water in the HCT is

$$m_{\mathrm{f,anh}}\left(z, t = 0\right) = m_{\mathrm{f,anh,0}} \tag{6.8a}$$

$$m_{\mathrm{f,w}}\left(z, t = 0\right) = m_{\mathrm{f,w,0}} \tag{6.8b}$$

6.2 Discretization of the PBE System

To solve the PBE system, the FVM is applied to Eqs. (6.1), (6.5), and (6.6), as suggested by Patankar (1980), in order to derive a semi-discrete PBE system. In the FVM, the partial differential equations (PDEs) are evaluated at discrete points on a mesh. These discrete points are surrounded by finite control volumes. The differential equations are integrated over each control volume. Between the mesh points, the variables are approximated by piecewise defined profiles. Fluxes entering one control volume leave an adjacent control volume. Hence, the FVM is conservative, but numerical diffusion occurs. Here, both the internal and external coordinate are discretized as displayed in Figure 6.1 where i is the index of the N_{i} control volumes in h and j is the index of the N_{j} control volumes in z. The nodes of the control volumes are located at integer values of the indices. For each coordinate, the interval widths, which are called Δz or Δh, and the corresponding distances between the midpoints of the control volumes are identical. The internal coordinate is discretized on the domain $\left[h_{1/2} = h_{\min}, h_{N_i+1/2} = h_{\max}\right]$ where the

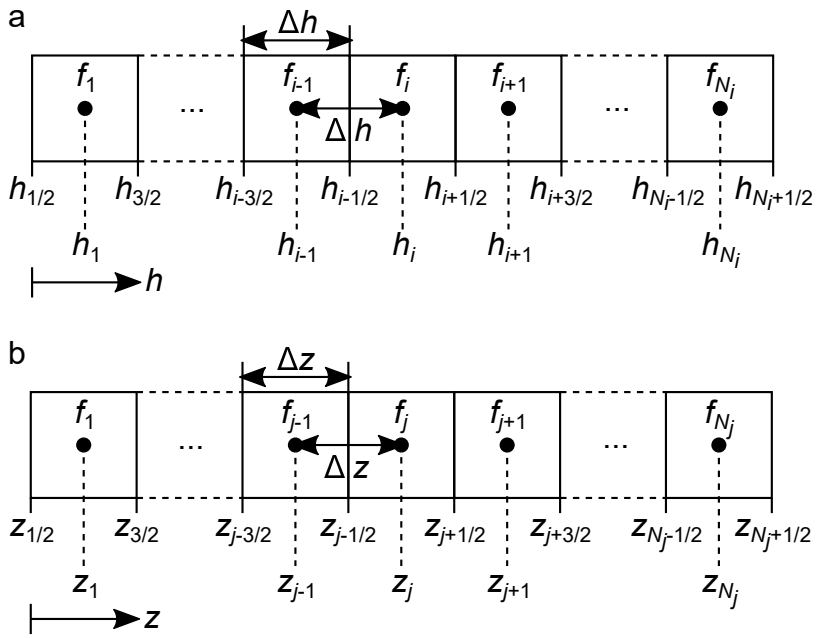

Figure 6.1: Discretization of f with control volumes of equal size and equidistant discrete points. (a) Internal property coordinate space; (b) external property coordinate space.

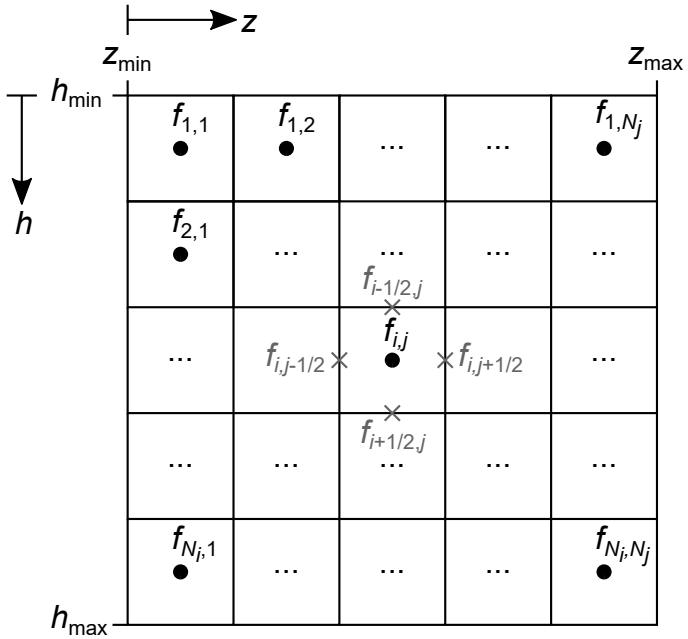

Figure 6.2: Discretization of f in the internal and external property coordinate space with the notation of f on the discretization grid.

limits should be chosen, such that all crystals remain in this size range during the whole process. The interval boundaries are located at $h_{i\pm1/2}$ for all intervals $i = 1, \ldots, N_\mathrm{i}$ and analogously for the external coordinate. The external coordinate is discretized on the domain $\left[z_{1/2} = z_{\min}, z_{N_j+1/2} = z_{\max}\right]$ where $z_{\min} = 0\,\mathrm{m}$ is the HCT inlet and $z_{\max} = l$ is the HCT outlet. The resulting ordinary differential equation (ODE) system on this domain

is

$$\frac{\mathrm{d}f_{i,j}}{\mathrm{d}t} = -\frac{G_j\left(f_{i+1/2,j} - f_{i-1/2,j}\right)}{\Delta h} - \frac{v_{\mathrm{p},i}\left(f_{i,j+1/2} - f_{i,j-1/2}\right)}{\Delta z} \tag{6.9}$$

where G_j is the growth rate in the control volume j of the tube and $v_{\mathrm{p},i}$ is the velocity of a crystal of size h_i. To evaluate Eq. (6.9), the values of f are required on the grid in one coordinate and in the control volume center in the other coordinate as depicted in Figure 6.2.

The Mass Balance Eqs. (6.5) and (6.6) are discretized via FVM, analogously to the crystal number density f, in the z-coordinate, as depicted in Figure 6.1b. The resulting ODEs are

$$\begin{aligned}\frac{\mathrm{d}m_{\mathrm{f,anh},1}}{\mathrm{d}t} =& - v_{\mathrm{f}}\frac{m_{\mathrm{f,anh},3/2} - m_{\mathrm{f,anh,in}}}{\Delta z} + D\frac{m_{\mathrm{f,anh},2} - 3m_{\mathrm{f,anh},1} + 2m_{\mathrm{f,anh,in}}}{\Delta z^2} \\ & - 3\chi_{\mathrm{anh}}k_V\rho_{\mathrm{p}}\sum_{i=1}^{N_i} G_1 h_i^2 f_{i,1}\Delta h \end{aligned} \tag{6.10a}$$

$$\begin{aligned}\frac{\mathrm{d}m_{\mathrm{f,anh},j}}{\mathrm{d}t} =& - v_{\mathrm{f}}\frac{m_{\mathrm{f,anh},j+1/2} - m_{\mathrm{f,anh},j-1/2}}{\Delta z} + D\frac{m_{\mathrm{f,anh},j+1} - 2m_{\mathrm{f,anh},j} + m_{\mathrm{f,anh},j-1}}{\Delta z^2} \\ & - 3\chi_{\mathrm{anh}}k_V\rho_{\mathrm{p}}\sum_{i=1}^{N_i} G_j h_i^2 f_{i,j}\Delta h, \qquad j = 2,\ 3,\ \ldots,\ (N_j - 1) \end{aligned} \tag{6.10b}$$

$$\begin{aligned}\frac{\mathrm{d}m_{\mathrm{f,anh},N_j}}{\mathrm{d}t} =& - v_{\mathrm{f}}\frac{m_{\mathrm{f,anh},N_j+1/2} - m_{\mathrm{f,anh},N_j-1/2}}{\Delta z} + D\frac{m_{\mathrm{f,anh},N_j-1} - m_{\mathrm{f,anh},N_j}}{\Delta z^2} \\ & - 3\chi_{\mathrm{anh}}k_V\rho_{\mathrm{p}}\sum_{i=1}^{N_i} G_{N_j} h_i^2 f_{i,N_j}\Delta h \end{aligned} \tag{6.10c}$$

$$\begin{aligned}\frac{\mathrm{d}m_{\mathrm{f,w},1}}{\mathrm{d}t} =& - v_{\mathrm{f}}\frac{m_{\mathrm{f,w},3/2} - m_{\mathrm{f,w,in}}}{\Delta z} + D\frac{m_{\mathrm{f,w},2} - 3m_{\mathrm{f,w},1} + 2m_{\mathrm{f,w,in}}}{\Delta z^2} \\ & - 3\left(1 - \chi_{\mathrm{anh}}\right)k_V\rho_{\mathrm{p}}\sum_{i=1}^{N_i} G_1 h_i^2 f_{i,1}\Delta h \end{aligned} \tag{6.11a}$$

$$\begin{aligned}\frac{\mathrm{d}m_{\mathrm{f,w},j}}{\mathrm{d}t} =& - v_{\mathrm{f}}\frac{m_{\mathrm{f,w},j+1/2} - m_{\mathrm{f,w},j-1/2}}{\Delta z} + D\frac{m_{\mathrm{f,w},j+1} - 2m_{\mathrm{f,w},j} + m_{\mathrm{f,w},j-1}}{\Delta z^2} \\ & - 3\left(1 - \chi_{\mathrm{anh}}\right)k_V\rho_{\mathrm{p}}\sum_{i=1}^{N_i} G_j h_i^2 f_{i,j}\Delta h, \qquad j = 2,\ 3,\ \ldots,\ (N_j - 1) \end{aligned} \tag{6.11b}$$

$$\begin{aligned}\frac{\mathrm{d}m_{\mathrm{f,w},N_j}}{\mathrm{d}t} =& - v_{\mathrm{f}}\frac{m_{\mathrm{f,w},N_j+1/2} - m_{\mathrm{f,w},N_j-1/2}}{\Delta z} + D\frac{m_{\mathrm{f,w},N_j-1} - m_{\mathrm{f,w},N_j}}{\Delta z^2} \\ & - 3\left(1 - \chi_{\mathrm{anh}}\right)k_V\rho_{\mathrm{p}}\sum_{i=1}^{N_i} G_{N_j} h_i^2 f_{i,N_j}\Delta h \end{aligned} \tag{6.11c}$$

A detailed derivation of the discretized Eqs (6.9), (6.10), and (6.11) is given in Appendix C.

A slope limiter avoids numerical oscillations for higher-order discretizations of PBEs. Oscillations may occur because of steep gradients, discontinuities, and opposite slopes in the solution (Griffiths, 2016). Here, sharp wave fronts may appear when simulating batch seeding or the start-up of the crystallizer. For sharp gradients, a slope limiter

restricts the derivatives to realistic values and the states are represented by a lower-order resolution scheme. For smooth gradients, the slope limiter does not take effect and the higher-order resolution scheme applies. A slope limiter is applied following Qamar et al. (2006) for convection of f, $m_{\mathrm{f,anh}}$, and $m_{\mathrm{f,w}}$ along z and for growth and dissolution of f in h. The resulting equations are exemplified for f discretized into i finite volumes along the h-coordinate and the equations are analog for the other states and coordinate.

$$\begin{aligned} f_{1/2} &= f\left(h_{\min}\right) \\ f_{3/2} &= f_1 \\ f_{i+1/2} &= f_i + \frac{1}{2}\left(\Phi\left(r_{i+1/2}\right)\right)\left(f_i - f_{i-1}\right), \qquad i = 2, \ldots, N_i - 2 \\ f_{N_i-1/2} &= f_{N_i-1} \\ f_{N_i+1/2} &= f_{N_i} \end{aligned} \tag{6.12}$$

Equation (6.12) results from an upwind scheme and is valid for growth, whereas for dissolution, the downwind scheme is applied, as given in the following

$$\begin{aligned} f_{1/2} &= f_1 \\ f_{3/2} &= f_2 \\ f_{i+1/2} &= f_{i+1} + \frac{1}{2}\left(\Phi\left(r_{i+1/2}\right)\right)\left(f_{i+1} - f_{i+2}\right), \qquad i = 2, \ldots, N_i - 2 \\ f_{N_i-1/2} &= f_{N_i} \\ f_{N_i+1/2} &= f\left(h_{\max}\right) \end{aligned}$$

Following Koren (1993), as cited in Qamar et al. (2006), the slope limiter function $\Phi(r)$ is

$$\Phi\left(r_{i+1/2}\right) = \max\left(0, \min\left(2r_{i+1/2}, \min\left(\frac{1}{3} + \frac{2}{3}r_{i+1/2}, 2\right)\right)\right) \tag{6.13}$$

and r is the ratio of successive gradients on the grid, that is

$$r_{i+1/2} = \frac{f_{i+1} - f_i + \varepsilon}{f_i - f_{i-1} + \varepsilon}$$

where ε is introduced to avoid zero division. Qamar (2008); Sweby (1984) illustrate that the values of the original high order scheme and the limited values for the slope ratio in Eq. (6.13) agree well for $r_{i+1/2} \approx 1$. For dissolution, the ratio of successive gradients becomes

$$r_{i+1/2} = \frac{f_i - f_{i+1} + \varepsilon}{f_{i+1} - f_{i+2} + \varepsilon}$$

For the non-discretized formulation, the initial condition on f was given in Eq. (6.2). The boundary condition in z, $f\left(z_{\min}\right)$, was given in Eq. (6.3). The boundary condition in h, $f\left(h_{\min}\right)$, was given in Eq. (6.4). After discretization, the initial condition for batch-wise seeding becomes

$$\begin{aligned} f_{\mathrm{batch}}\left(h, z_1, t = 0\right) &= f_{i,1}\left(t = 0\right) = f_{\mathrm{in}}, \quad i = 1,\ 2,\ \ldots,\ N_i \\ f_{\mathrm{batch}}\left(h, z > z_1, t = 0\right) &= f_{i,j}\left(t = 0\right) = 0, \qquad i = 1,\ 2,\ \ldots,\ N_i, \quad j = 2,\ \ldots,\ N_j \end{aligned}$$

For continuous seeding, the initial condition is

$$f_{\text{conti}}\left(h, z > z_{1/2}, t = 0\right) = f_{i,j}\left(t = 0\right) = 0, \qquad i = 1,\ 2,\ \ldots,\ N_i, \quad j = 1,\ 2,\ \ldots,\ N_j$$

The boundary condition in z for batch seeding is

$$f_{\text{batch}}\left(h, z_{1/2}, t\right) = f_{i,1/2}\left(t\right) = 0, \qquad i = 1,\ 2,\ \ldots,\ N_i$$

and for continuous seeding, it is

$$f_{\text{conti}}\left(h, z_{1/2}, t\right) = f_{i,1/2}\left(t\right) = \frac{\dot{f}_{\text{in}}\Delta z}{v_{\text{p}}}, \qquad i = 1,\ 2,\ \ldots,\ N_i$$

where $\dot{f}_{\text{in}}$ is given in $\mathrm{kg\,s^{-1}}$. The lower boundary condition in h is

$$f\left(h_{1/2}, z, t\right) = f_{1/2,j}\left(t\right) = 0, \qquad j = 1,\ 2,\ \ldots,\ N_j$$

and for dissolution the upper boundary condition is

$$f\left(h_{N_i+1/2}, z, t\right) = f_{N_i+1/2,j}\left(t\right) = 0, \qquad j = 1,\ 2,\ \ldots,\ N_j$$

After discretization, the boundary condition on the mass of the continuous phase in Eq. (6.7) becomes

$$m_{\text{f,anh}}\left(z_{\min}, t\right) = m_{\text{f,anh},1/2}\left(t\right) = m_{\text{f,anh,in}} \tag{6.15a}$$
$$m_{\text{f,w}}\left(z_{\min}, t\right) = m_{\text{f,w},1/2}\left(t\right) \ = m_{\text{f,w,in}} \tag{6.15b}$$

and the initial condition in Eq. (6.8) becomes

$$m_{\text{f,anh},j}\left(t = 0\right) = m_{\text{f,anh},0}, \qquad j = 1,\ 2,\ \ldots,\ N_j \tag{6.16a}$$
$$m_{\text{f,w},j}\left(t = 0\right) \ = m_{\text{f,w},0}, \qquad j = 1,\ 2,\ \ldots,\ N_j \tag{6.16b}$$

6.3 Model Parameterization

The material, geometry, and numerical parameters that were used for the HCT simulations, if not stated otherwise, are given in Table 6.1. The total tube length l that the crystals pass can be calculated from the lengths of the tube sections from the seeding valve to the flow-through microscope in Table 4.1. For the setup that was depicted in Figure 4.4a the diameter of the last 25 m tube length is assumed for the whole tube, and an average fluid velocity is calculated for this diameter (refer to Table 4.1). The total number of finite volumes N_j in z refers to a tube length $l = 33\,\mathrm{m}$ as in setup a. N_j is adjusted for the other setups to a finite number of control volumes to create a comparable numerical diffusion.

A constant value is assumed for the fluid density ρ_{f}, as discussed in Section 4.2.3. It is used to calculate the average fluid velocities $v_{\text{f,low}}$ and $v_{\text{f,high}}$, applying the mass flow rates that were given in Section 4.2.2, to calculate the initial mass inside the crystallizer, and to calculate the mass at the inlet. The initial mass in each control volume and the mass at the inlet are identical.

For ε, the same value is chosen as by Qamar et al. (2006). The ODEs 6.9, 6.10, and 6.11 are solved with the Runge-Kutta solver ode45 in Matlab. The dispersion coefficient

Table 6.1: Parameters for the simulation of the potash alum system in the HCT.

Symbol	Value	Unit
Material parameters		
χ_{anh}	0.5443	–
ρ_{p}	1757	$\text{kg}\,\text{m}^{-3}$
ρ_{f}	1100	$\text{kg}\,\text{m}^{-3}$
Numerical parameters		
h_{min}	25×10^{-6}	m
h_{max}	275×10^{-6}	m
N_i	25	–
N_j	220 per 33 m tube length	–
ε	10^{-10}	–
Geometry parameters		
d	6×10^{-3}	m
l_{a}	33	m
$l_{\text{b,up}}$	33.8	m
$l_{\text{b,down}}$	34.1	m
Process parameters		
$v_{\text{f,low}}$	0.24	$\text{m}\,\text{s}^{-1}$
$v_{\text{f,high}}$	0.35	$\text{m}\,\text{s}^{-1}$
$m_{\text{seed,small}}$	1×10^{-4}	kg
$m_{\text{seed,mix}}$	3×10^{-4}	kg
$\dot{m}_{\text{seed,low}}$	m_{seed} per second	$\text{kg}\,\text{s}^{-1}$
$\dot{m}_{\text{seed,high}}$	$\dot{m}_{\text{seed,low}} \frac{v_{\text{f,high}}}{v_{\text{f,low}}}$	$\text{kg}\,\text{s}^{-1}$

of the continuous phase, the crystal velocity, and the crystal growth rate are estimated from experiments.

An overview of the process conditions, which are specific for each of the experiments in the subsequent sections, are given in Table 6.2. The size-dependent crystal velocity was measured at average fluid velocities of $v_{\text{f,low}} = 0.24\,\text{m}\,\text{s}^{-1}$ and $v_{\text{f,high}} = 0.35\,\text{m}\,\text{s}^{-1}$. For the experiments that are simulated in the following, v_{f} deviates up to 4 % from these values. The feed masses $m_{\text{f,anh/w,in}}$ and the initial masses $m_{\text{f,anh/w,0}}$ were identical. The seed distributions f_{in} were shown in Figure 4.2. The seed mass m_{seed} was $1 \times 10^{-4}\,\text{kg}$ for the smallest size fraction and $3 \times 10^{-4}\,\text{kg}$ for the mixed size fraction. For the crystal supply rate $\dot{f}_{\text{in}}$ during continuous seeding, it is assumed that f_{in} was supplied once per second.

6.3.1 Dispersion Coefficient

The dispersion coefficient is determined from a comparison of conductivity tracer simulations to experiments, which were described for setup b in Section 4.3.1. Additionally, tracer experiments were conducted in setup a at 309 K and are now compared to simulations.

For the simulations, the total tube length has to be known. The tube length l_{a} of setup a, which was measured from the seed addition position to the outlet, was given in Table 6.1. In the tracer experiments, the tracer passes an additional tube section before the seed addition valve including the pump and, for downward experiments, including the

Table 6.2: Experimental parameters for the experiments in Sections 6.3.2 and 6.3.3. Supersaturation calculated on the basis of Eq. (4.2) for the given initial masses in the continuous phase, which correspond to initial and feed saturation temperatures from T =313 K to 314 K.

Experiment	σ_{in}	σ_{out}	$m_{\text{f,anh,in}}$	$m_{\text{f,w,in}}$
Figure 6.7	-4 %	1 %	5.1×10^{-4} kg	4.26×10^{-3} kg
Figure 6.8a,b	-10 %	10 %	5.1×10^{-4} kg	4.26×10^{-3} kg
Figure 6.8c,d	-12 %	2 %	5.2×10^{-4} kg	4.38×10^{-3} kg
Figure 6.9a	-4 %	4 %	4.9×10^{-4} kg	4.17×10^{-3} kg
Figure 6.9b	-8 %	14 %	4.9×10^{-4} kg	4.17×10^{-3} kg
Figure 6.9c	-5 %	19 %	4.9×10^{-4} kg	4.17×10^{-3} kg

debubbler. The length of this section is called l_{inlet} and is determined in the following.

To calculate the tube length, the mass flow rate is required. The conductivity experiments were carried out at four different pump speeds. To measure the conductivity, the flow-through microscope was replaced by a probe. This may influence the mass flow rate. For upward flow, the mass flow rate was determined once at the four different pump speeds by averaged weighing measurements. For downward flow, the mass flow rate was measured for each experiment by mass flow measurements with a Coriolis type mass flow sensor. Then, the mass flow rate was applied to calculate the average fluid velocity v_{f} using the known tube diameter.

For each tracer experiment, the offset additional length l_{inlet} is the product of the average fluid velocity v_{f} and the mean fluid RT $\tau_{\text{f,inlet}}$ of the tracer signal. $\tau_{\text{f,inlet}}$ was calculated from the conductivity signal of the experiments at the seed addition position, as depicted as "inlet" in Figure 4.6. For each experiment, the calculated v_{f} and l_{inlet} are illustrated in Figure 6.3 by a marker. A simple linear regression model was fitted minimizing least-squares for the upward and downward tracer experiments at the inlet position. The resulting linear polynomials are also shown. For the experiments at the outlet position, l_{inlet} was calculated from these polynomials. The resulting l_{tracer}, which is the sum of l_{inlet} and l_{a}, is given in Table 6.3. For setup a, the additional tube length l_{inlet} is set to 4 m. As explained in Section 6.3, N_j increases proportionally to the increase in tube length. For all tracer simulations, a fluid density ρ_{f} of water at room temperature of

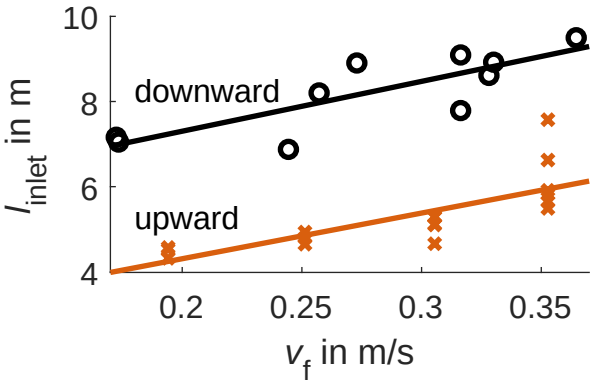

Figure 6.3: Tracer measurements at the seed-addition valve in the HCT setup in Figure 4.4b (Wiedmeyer et al., 2017a) for upward (orange) and downward (black) flow.

Table 6.3: Values of dynamic viscosity, average fluid velocity, Reynolds number, tracer tube length, and inlet pulse duration in the tracer simulations.

Symbol and Unit	Setup b Figure 6.4a-d				Setup a Figure 6.5a-b	
Flow direction	upward	upward	downward	downward	upward	upward
$\eta_\mathrm{f} \times 10^4$ [kg m^{-1} s^{-1}]	8.992	8.992	8.693	8.891	7.058	7.058
v_f [m s^{-1}]	0.23058	0.32518	0.23649	0.34095	0.2564	0.2564
Re [−]	1534	2163	1627	2294	2173	2173
l_tracer [m]	37.6	38.6	40.7	42.0	37	37
t_in [s]	15	15	15	15	19	20

997 kg m^{-3} is assumed. Regarding the simulation, no crystals are added, f_in is zero, and the PBE in Eq. (6.9) remains zero during the simulation. In the mass balance Eqs. (6.10) and (6.11), the same dispersion coefficient is assumed. Initially, the tube is filled with water and the initial condition in Eq. (6.16) for each control volume is

$$m_{\mathrm{f,anh},0} = 0$$
$$m_{\mathrm{f,w},0} = \rho_\mathrm{f} \Delta z \pi R^2 = 4.35 \times 10^{-3}\,\mathrm{kg}$$

where $\rho_\mathrm{f} = 997\,\mathrm{kg\,m^{-3}}$ and $\Delta z = 0.15\,\mathrm{m}$. For the tracer mass fraction, which is given in Section 4.3.1, the boundary condition at the inlet in Eq. (6.15) becomes

$$m_{\mathrm{f,anh,in}} = 1.6 \times 10^{-4}\,\mathrm{kg}$$
$$m_{\mathrm{f,w,in}} = 4.20 \times 10^{-3}\,\mathrm{kg}$$

For a dispersion coefficient $D = 0.015\,\mathrm{m^2\,s^{-1}}$, a good agreement between experiments and simulations can be achieved as displayed in Figures 6.4 and 6.5. The dispersion coefficient is seven to eight magnitudes larger than the diffusion coefficient of potash alum solutions (Mullin et al., 1965), hence, the diffusion coefficient is not further discussed. For setup b, the same tracer outlet signals are depicted in Figure 6.4 as in Figure 4.6 in the experimental section. In Section 4.3.1, only the tube section that is relevant for crystal growth, which starts at the seed-addition valve, was considered to calculate τ_f. The inlet signal, also, was measured at the seed addition position a few seconds after the start of an experiment. Here, the whole tube section is considered to calculate τ_f. The inlet signal illustrates the mass fraction of the tracer solution and the duration of tracer addition at the reservoir position. The axial dispersion coefficient influences the width of the tracer signal at the outlet. The width agrees well for experiments and simulations in Figure 6.4. At downward flow, the simulations show slightly narrower curves, but because the peak height agrees well, the axial dispersion coefficient is not adjusted further. In Figure 6.5 for setup a, the simulations and experiments also agree well. The noise in the second experiment results from air bubbles that disturb the conductivity signal, but the overall peak height and width are in accordance. Hence, the axial dispersion coefficient was validated in setup a. In simulations, axial dispersion results from the dispersion term in Eqs. (6.10) and (6.11) as well as from numerical diffusion. Therefore, the axial dispersion coefficient, which is used for the simulations, is smaller than the physical dispersion coefficient. The extent of the numerical diffusion depends on the grid refinement of the FVM. For comparability of simulations of varying tube length, the number of finite volumes is scaled with the tube length, as noted in Table 6.1. The hydrodynamic axial dispersion coefficient can

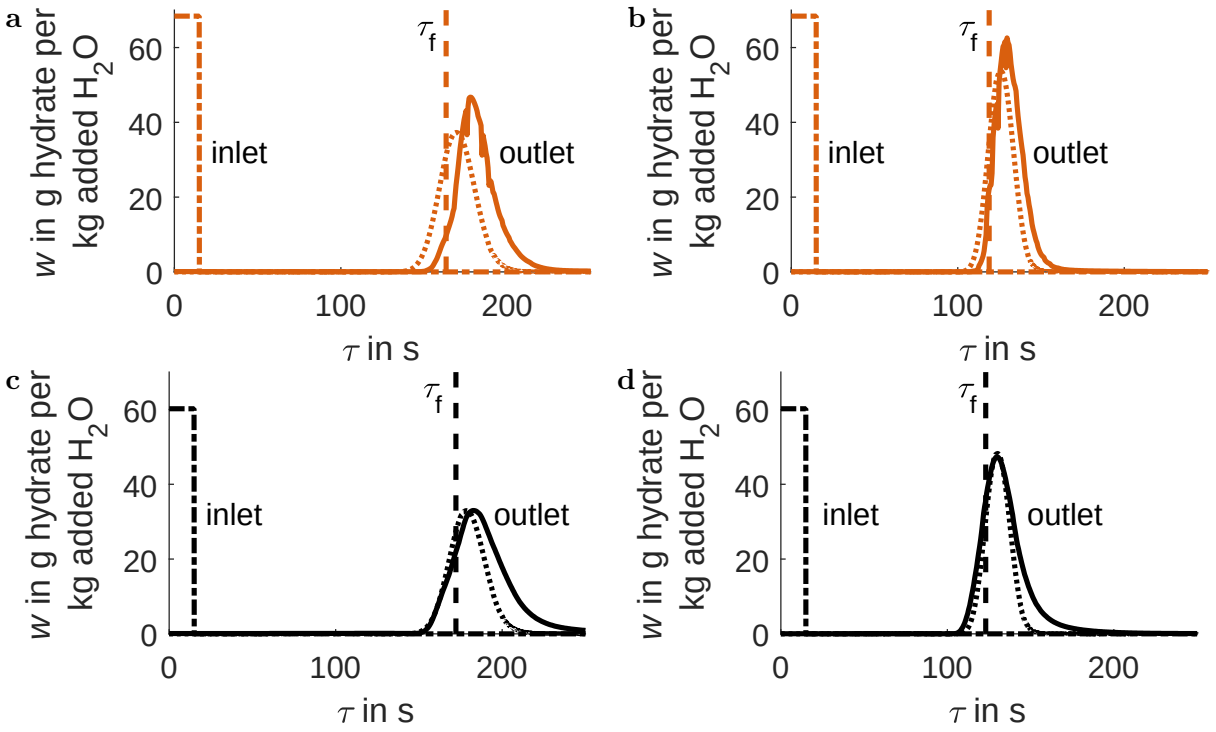

Figure 6.4: Tracer measurements in the HCT setup in Figure 4.4b for (a,b) upward and (c,d) downward flow. (a,c) Low Reynolds numbers $Re_{\mathrm{up/down}} = 1534/1627$; (b,d) high Reynolds numbers $Re_{\mathrm{up/down}} = 2163/2294$. Average RT as determined by the Coriolis-type mass flow sensor (dashed vertical lines). Experimental outlet signal as in Figure 4.6 (solid) and outlet signal determined from simulations (dotted).

Source: Adapted with permission from Wiedmeyer et al. (2017a). Copyright 2017 American Chemical Society.

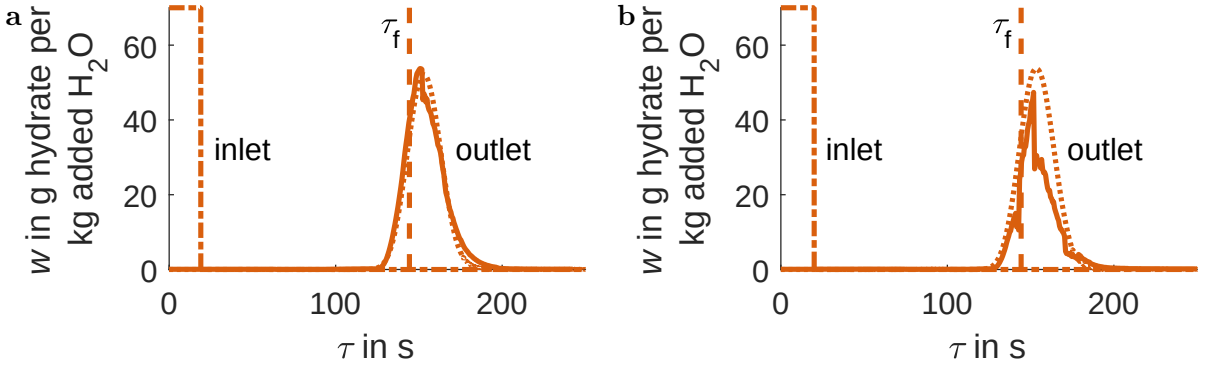

Figure 6.5: Tracer measurements indicating the fluid RT in the HCT setup in Figure 4.4a (Wiedmeyer et al., 2017b) for similar conditions at $Re_{\mathrm{up}} = 2173$. Average RT as determined by the Coriolis-type mass flow sensor (dashed vertical lines). Experimentally measured outlet signal (solid) and outlet signal determined from simulations (dotted).

be derived from the Bodenstein number (Klutz et al., 2015). The Bodenstein number is estimated from a minimization of least squares of the dimensionless tracer concentration, which is estimated from Figures 6.4 and 6.5. The resulting Bodenstein number is 330 ± 92

and the hydrodynamic axial dispersion coefficient is $(0.036 \pm 0.017)\,\mathrm{m^2\,s^{-1}}$.

6.3.2 Size-Dependent Crystal Velocity

In the experimental section 4.3.2, a size-dependent crystal RT was observed. In a PBE model, the particle-size-dependent velocity can be derived from the measured RT in several ways. The RT measurements can be used directly, if the whole range of particle sizes was covered. Outside this range, extrapolations have to be applied, whereas inside interpolations can be used. For the whole size range, two overlapping transformed exponential functions may approximate the relation. Figure 5.4 illustrates that for large crystals, the RT is inversely proportional to the crystal size. A quadratic polynomial fit was applied for the large crystals in setup a (Wiedmeyer et al., 2017b). For small crystals, the RT is proportional to the crystal size. The increase is similar to a positive logarithmic function or a negative inverse hyperbolic cotangent. As discussed in Section 5.5, considering small particles, their initial position becomes important. They leave the tube before sinking to the tube bottom. When they start at a random tube position, their velocity approaches that of the fluid at the corresponding cross-sectional location. The original cross-sectional position in the experiments is unknown. When the particle velocity is modeled in dependence of particle size, the average fluid velocity may be a good assumption for the particle velocity for very small particles.

For the following simulations, the experimental data is used to calculate a size-dependent crystal velocity. The crystal RT was strongly dependent on the average fluid velocity and evinced minor variations with setup and flow direction in the coils. A functional relationship could be derived on the basis of the average fluid velocity. As there were only four different fluid velocities tested in setup b and only two average fluid velocities were applied in all setups, too few data points are available to identify a functional relationship. Instead, for each combination of setup, flow direction, and average fluid velocity, as presented in Figures 4.8, 4.9, and 4.10, a look-up table was generated for the simulations. Each of the crystals that was observed in the experiments was sorted into a size class. The size classes were discretized in 8 µm wide bins starting from 0 µm. The average RT of all crystals in the same size class was marked in the aforementioned figures. The respective tube length is applied to calculate the average crystal velocity from the average RT, which is assumed to be valid in the center of the respective size class. Velocities are interpolated via a cubic spline (Matlab 2018b) on a grid of 1 µm bin width.

For the simulations, any discretization in crystal size may be chosen. The average crystal velocity is required at the center of the current grid h_i for all i. For crystals, as observed in the isothermal experiments, e.g., from 50 µm to 220 µm in setup b, the average crystal velocity is linearly interpolated at the required grid points. During the growth experiments, crystals are likely to grow and to reach larger sizes. It is assumed that crystals that approach the tube diameter, as well as very small crystals, reach the average velocity of the fluid. Hence, a linear extrapolation is applied for crystals from 0 µm to 50 µm and from 220 µm to 1000 µm. For setup b, the results are shown in Figure 6.6. For the other setups, the profiles are similar.

Applying the size-dependent velocity, exemplary simulation results are depicted in Figure 6.7. The experiment was carried out in setup b at a nearly constant temperature. At the inlet, the solution is slightly undersaturated, but the inlet section before the cooled HCT is short and dissolution is negligible. The seeds were a mixed fraction, as illustrated in Figure 4.2. For the simulation, it was assumed that $h > 50\,\mu\mathrm{m}$. The surface and vol-

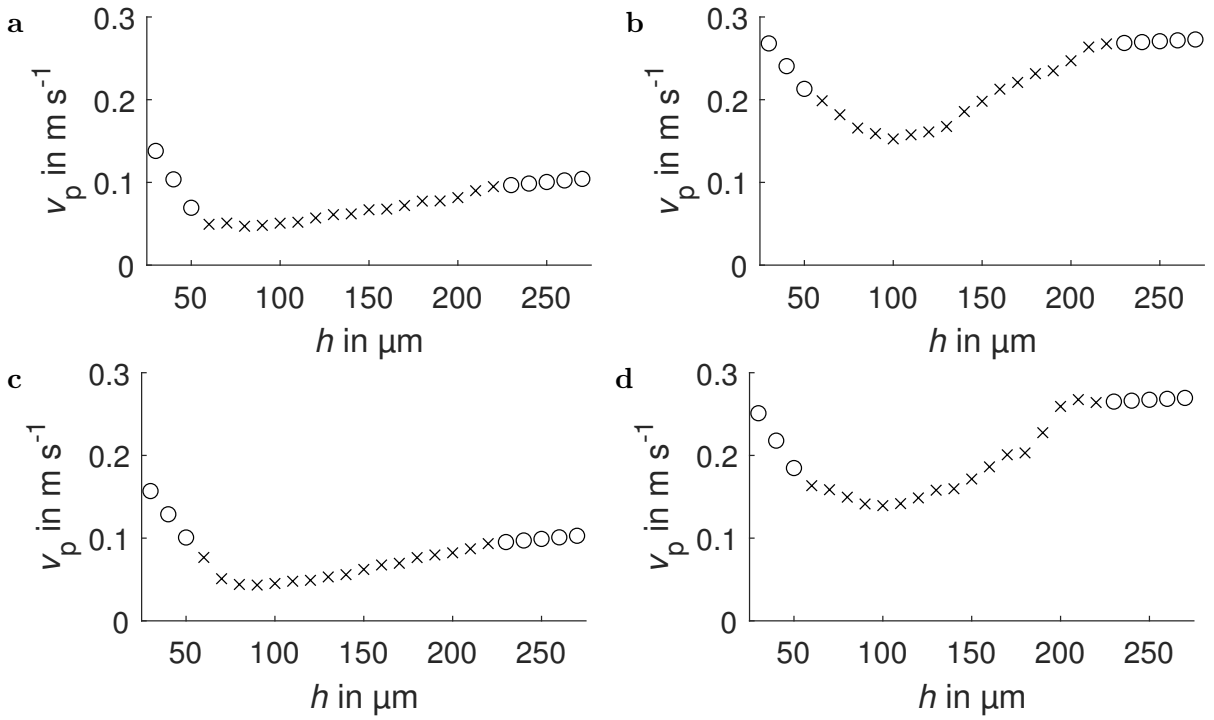

Figure 6.6: Size-dependent crystal velocity values in the setup in Figure 4.4b based on the experimental data shown in Figure 4.9. x for interpolated values and o for extrapolated values. (a,b) Upward flow; (c,d) downward flow; (a,c) $v_{\mathrm{f,low}} = 0.24\,\mathrm{m\,s^{-1}}$; (b,d) $v_{\mathrm{f,high}} = 0.35\,\mathrm{m\,s^{-1}}$.

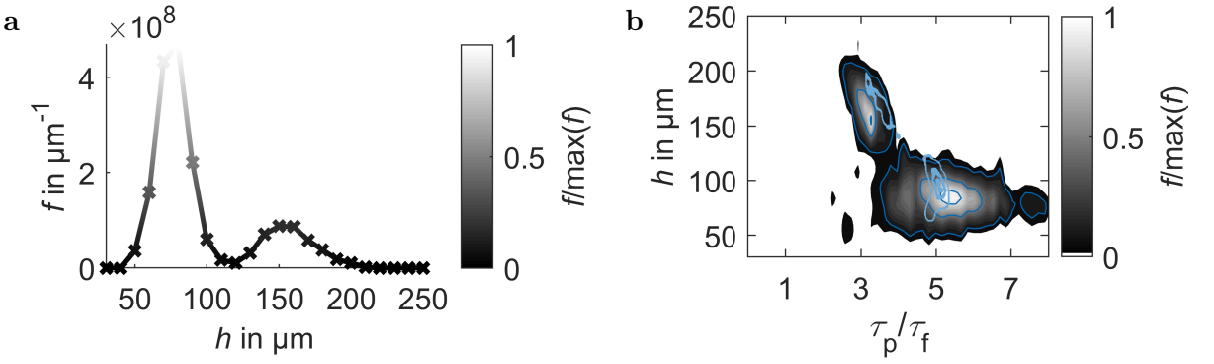

Figure 6.7: Simulation under conditions as in the experiment in Figure 4.13a in the setup in Figure 4.4b at upward flow and low Reynolds number. (a) Seed distribution adapted ($h > 50\,\mu\mathrm{m}$) from the mixed fraction in Figure 4.2; (b) experimental (gray) and simulated (light blue) product distribution with highlighted first decile, median, and ninth decile.

Source: Adapted with permission from Wiedmeyer et al. (2017a). Copyright 2017 American Chemical Society.

ume percentage of the small neglected crystals are 8 % and 1 %. Because the percentage is small, the contribution to the supersaturation depletion is small, and the small crystals can be neglected. The resulting distribution is shown in Figure 6.7a. For this simulation and all the following ones, the initial distribution was scaled to agree with the experimental seed mass. In Figure 6.7b, each size h should be considered with its associated τ_p. The

mean RTs agree well in experiment and simulation. In the simulation, all inserted crystals were observed at the outlet. Hence, the variance is small compared with the experiments. In the experiments, not all crystals were observed, because of a limited frame rate, and because of a limited size of the imaging window of the cuvette.

6.3.3 Growth and Dissolution Kinetics

To select one of different growth rate expressions for potash alum from literature, an appropriate experiment has to be selected for comparison to growth simulations. Ideally that experiment fulfills the following features. A high supersaturation is applied for a large increase in the crystal size, but nucleation is avoided. For the same reason, a large RT and, hence, a small Reynolds number is favorable. For validation, an additional experiment at a large Reynolds number can be selected. The average fluid velocity should be similar to the velocity at which the corresponding crystal-size-dependent velocity was determined.

When the growth kinetic with the best agreement between experiment and simulation has been selected, a dissolution kinetic is added, and experiments and simulations can be compared for further parameter variations. Considering the seed crystal fraction, a small size may be favored to stay in the size range where the size-dependent crystal velocity was measured. A large seed crystal size may be applied to test the extrapolation.

The investigated growth and dissolution rates G have the following form

$$G = p_1 \exp\left(\frac{-p_2}{R_\mathrm{m} T}\right) \sigma^{p_3} \tag{6.17}$$

and the unit of $\mathrm{m\,s^{-1}}$ where R_m is the molar gas constant. Growth occurs for a positive supersaturation σ and dissolution occurs for negative values. The kinetic parameters are listed in Table 6.4. For the simulations with the kinetics by Temmel et al. (2016) also their solubility, which was given in Eq. (4.3), is applied to calculate the supersaturation. The supersaturation σ was defined in Eq. (4.4). It depends on the mass fraction w, which was defined in Eq. (4.1). In Section 4.1, the mass fraction w and the supersaturation σ were defined from an experimental point of view, via the mass of the added solid hydrate, which was dissolved, and the mass of the added liquid water. Here, the continuous phase equations are defined in terms of the anhydrate and water in solution. The anhydrate mass fraction in kg anhydrate per kg solution is

$$w_\mathrm{f,anh} = \frac{m_\mathrm{f,anh}}{m_\mathrm{f,anh} + m_\mathrm{f,w}} \tag{6.18}$$

Table 6.4: Kinetic parameter values for Eq. (6.17) for growth and dissolution. The kinetics by Temmel et al. (2016) are multiplied by a correction factor of $\frac{1}{\sqrt{6}}$ to recalculate the different shape factor.

Reference	Kinetic	p_1 $[\mathrm{m\,s^{-1}}]$	p_2 $[\mathrm{kJ\,mol^{-1}}]$	p_3 $[-]$
Ma et al. (2008)	growth	7.52×10^{-6}	0	1.6
Ma et al. (2012)	growth	19.27×10^{-6}	0	2.24
Temmel et al. (2016)	growth	$\frac{1.7}{\sqrt{6}} \times 10^{-6}$	5.7×10^{-9}	1.04
Temmel et al. (2016)	dissolution	$\frac{4.3}{\sqrt{6}} \times 10^{-6}$	0	1

The mass fraction w was defined in units of hydrate per kg free water in Eq. (4.1). For conversion, w can be calculated in dependence of $m_{\mathrm{f,anh}}$ and $m_{\mathrm{f,w}}$ applying $w_{\mathrm{f,anh}}$, as defined in Eq. (6.18)

$$w = \frac{w_{\mathrm{f,anh}}}{\chi_{\mathrm{anh}} - w_{\mathrm{f,anh}}}$$

As illustrated in Figure 4.3, the temperature was measured at the inlet and outlet of the setup. For the simulations, an interpolation between these temperatures along the tube is required to determine $\vartheta(z)$. It is assumed that the temperature profile is

$$\vartheta(z) = \vartheta_{\mathrm{out}} + (\vartheta_{\mathrm{in}} - \vartheta_{\mathrm{out}}) \exp\left(\frac{-z}{2}\right) \tag{6.19}$$

This correlation was derived from outlet temperature measurements in preliminary setups of shorter tube length. Half of the temperature difference between ϑ_{in} and ϑ_{out} is reached at 1.39 m. No sensors were introduced in the setups in this study and ϑ_{out} was approached within a very short tube distance. Hence, the thermal decay was not specified further. If cooling was slow, the thermal decay might be defined on the basis of l, d, v_{f}, cooling medium flow rate, and specific heat capacity of the cooling medium.

First, different growth kinetics are compared for the experiment that was depicted in Figure 4.13b. The best agreement between experiment and simulation is achieved with the growth kinetic by Temmel et al. (2016) in Figure 6.8a,b. Second, dissolution is taken into account as well. Applying the temperature profile that was given in Eq. (6.19), dissolution has no significant effect on the product distribution according to Figure 6.8b. In both, simulation and experiment, the large crystals in the mixed seed population grow by approximately 40 µm and reach a peak of 190 µm. The distance between the peaks of the small and large fraction widens slightly from 73 µm to 84 µm in the experiment, although it narrows to 60 µm in the simulation. As small crystals spend more time in the HCT, it can be expected that the small crystals grow stronger in the simulation than the large ones. The widening in the experiment may be caused by growth rate dispersion, which was not included in the model.

Another experiment at a high average flow rate was simulated. In this experiment, v_{f} was 4 % lower than $v_{\mathrm{f,high}}$, at which v_{p} was determined. Hence, v_{p} may be too high in the simulation and the crystal RT and the growth may be slightly underestimated in the simulation. This agrees with the small difference in the CSD in Figure 6.8d. Again, the best agreement with the experiment is achieved for the growth kinetic by Temmel et al. (2016). Consequently, this kinetic growth expression is used in the following. Further experiments in setup a are simulated with the selected growth rate. Here, in contrast to the before-mentioned experiment, the measured average fluid velocities were between 3 % to 4 % higher than the low average fluid velocity at which the crystal-size-dependent velocity was determined. Hence, the crystal RT is slightly overestimated in the simulations. The final crystal size seems to be larger in the experiments. There, the actual tube diameter is smaller than the assumed one in the simulations in the first part of the tube. Therefore, in the experiments, the crystals spend more time in the second part of the tube, and they experience cold conditions for a larger ratio of their residence time and grow stronger. Nevertheless, the deviations between the deciles of the experimental and the simulated final product size are small in Figure 6.9. In Figure 6.9b,c, nuclei appear in the experimental product distribution for a high σ_{out}, as discussed in Section 4.3.3. As nucleation is not included in the model, the simulations lead to narrower product

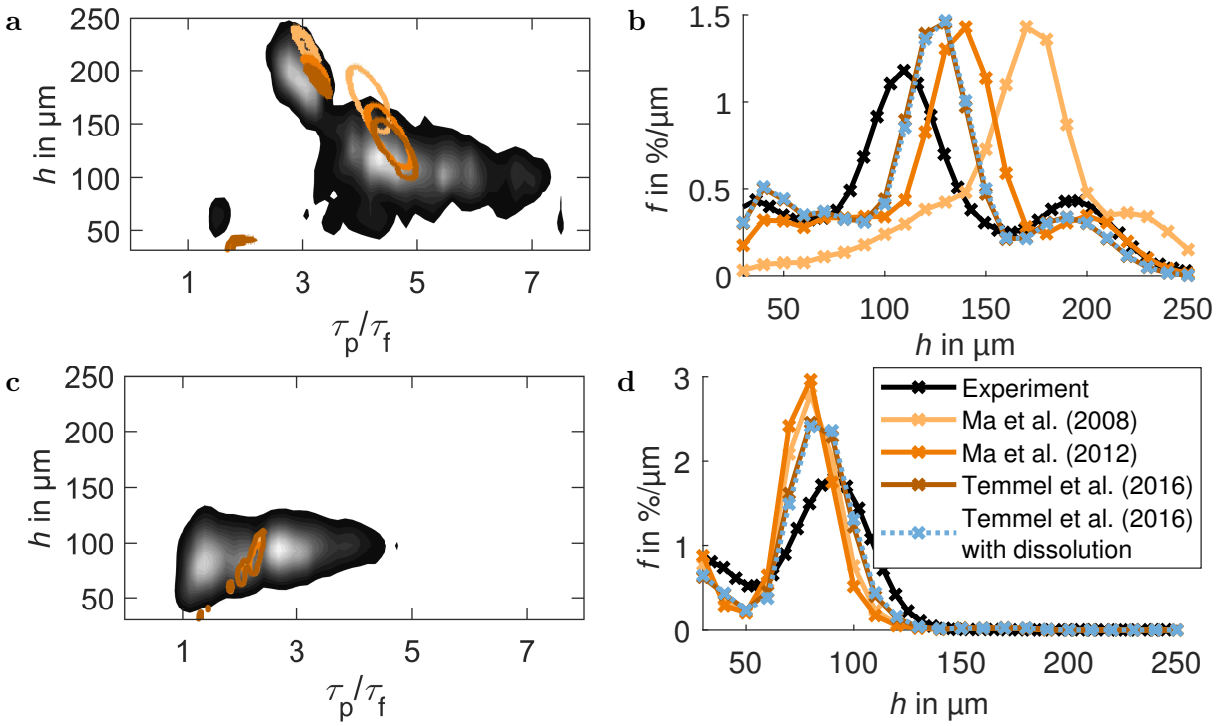

Figure 6.8: Product distributions for the experiment in (a,b) Figure 4.13b and (c,d) Figure 4.11c (gray) and for simulations (color) for various kinetics. (a,c) Growth kinetics by Ma et al. (2008), Ma et al. (2012), and Temmel et al. (2016) (orange with increasing darkness). Simulation contours show where 85 % of the crystal population are located; (b,d) product number density distribution normed by the total crystal number for experiment (black solid), growth simulations (orange solid) with the same kinetics as in (a), and a simulation with growth and dissolution kinetics by Temmel et al. (2016) (blue dotted).

Source: Adapted with permission from Wiedmeyer et al. (2017a). Copyright 2017 American Chemical Society.

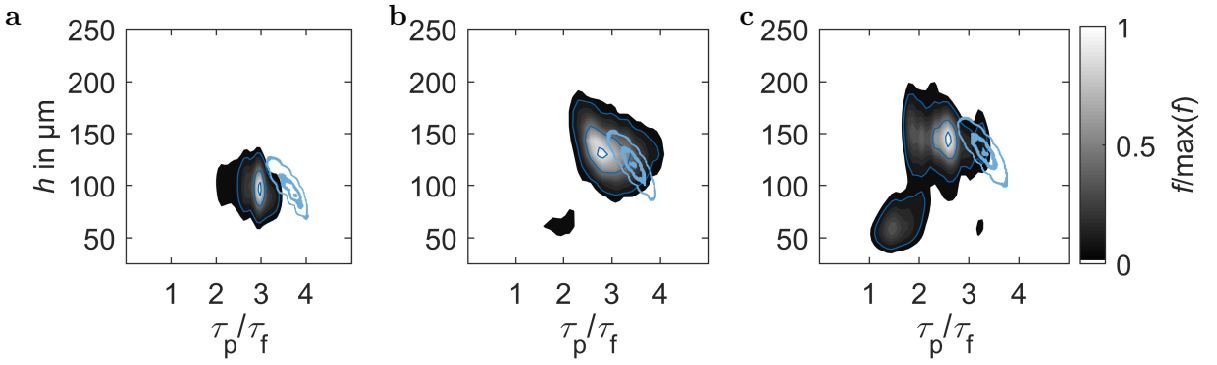

Figure 6.9: Experimental (gray) and simulated (bold light blue) product distribution with highlighted first decile, median, and ninth decile. Experiments as in Figure 4.12.

Source: Reprinted with permission from Wiedmeyer et al. (2017b). Copyright 2017 Wiley-VCH. Modifications: simulated deciles added, smaller crystals considered in the data, x-axis scaled by fluid residence time, limits of y-axis changed, and names of symbols adjusted.

CSDs. Hence, there is a considerable difference in the first decile, but larger deciles agree well. In all growth simulations, the product distributions are slightly narrower than in the experiments. This may be expected, because growth rate dispersion was not included in the model and is only partly accounted for by numerical diffusion.

6.4 Crystal Growth Simulations

Below, the model and process parameters are as described in the previous sections where $m_{\mathrm{seed}} = 1 \times 10^{-4}\,\mathrm{kg}$, $m_{\mathrm{f,anh,in}} = 4.8 \times 10^{-4}\,\mathrm{kg}$, $m_{\mathrm{f,w,in}} = 4.2 \times 10^{-3}\,\mathrm{kg}$, $T_{\mathrm{out}} = 309\,\mathrm{K}$, and $T_{\mathrm{in}} = 313\,\mathrm{K}$, such that the initial and feed solution are at saturation. These parameters and v_{p} are identical to the values that were measured in the HCT setup in Figure 4.4b at upward flow, as displayed in Figure 6.6a,b. The conditions are fixed in all simulations, unless otherwise stated, for comparability, but the discussion is kept general.

6.4.1 Simulations for Batch Seeding

In this section, the effect of the fluid velocity, particle velocity, and tube length on the product CSD is studied via simulations for batch-seeded experiments. First, the effect of the size-dependent crystal velocity is estimated. The size-dependent velocity model and a simplified model are compared. It is assumed that in simplified models, the same, in other words constant, crystal velocity is used for all crystals, which is equal to the velocity of the mean crystal size of an initial distribution under no growth conditions. In this case, the RT, especially of the large growing crystals, does not reduce. Hence, in the simplified model, the RT and the mean product crystal size are overestimated, as illustrated in Figure 6.10. It shows outlet distributions that result from the growth of a normally distributed seed crystal fraction. The width of the CSD broadens, but it is similar for both particle velocity models. The product width of initially very broad CSDs would also be overestimated by the simplified model. In this case, this effect would be amplified by the fluid for batch seeding. The fluid is faster than the crystals. In the size-dependent velocity model, the fluid supplies fresh solution of high concentration to the slow small crystals, which lets them grow stronger than the large ones. Hence, a broad inlet CSD is narrowed further. Another parameter that is varied is the tube length. As expected, the product crystal size increases with tube length. Comparing the constant velocity simulations to the size-dependent velocity simulations in Figure 6.10, the deviation in the estimated RT gets more pronounced with increasing tube length. Summing up, the predictions of the RT and CSD evince good accuracy for low growth conditions, for the simplified model, and for the size-dependent velocity model. For the selected conditions, discernible deviations appear for a tube length above approximately 50 m in Figure 6.10.

In the following, the size-dependent fluid velocity is applied. As depicted in Figure 6.11a, the standard deviation of the mean crystal size increases only slightly with tube length. Comparing different flow rates, at the same tube length, the mean product size is larger for the low flow rate. In this case, the crystals have more time to reduce the supersaturation. At both flow rates, the product CSD stays narrow. Comparing the velocities regarding the space-time yield, in Figure 6.11b, at $v_{\mathrm{f,low}}$, there is a higher product to seed mass ratio. A lower feed rate for the solution is required, but the RT is longer.

Next to tube length, the mean product crystal size is strongly influenced by the temperature profile. Faster cooling along the tube by higher cooling medium flow rates or

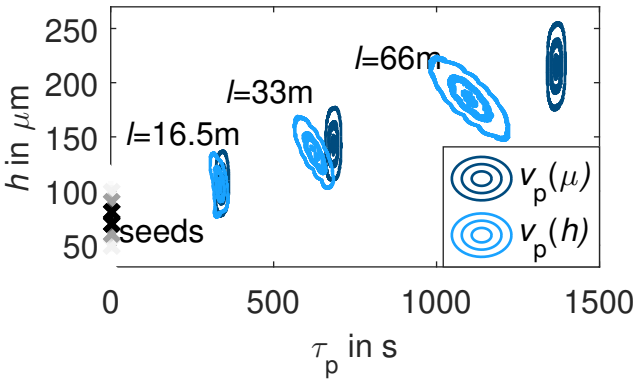

Figure 6.10: Seed distribution (gray) and product CSDs with their first decile, median, and ninth decile (blue) resulting from growth. Normal inlet distribution with a mean of 75 µm and a standard deviation of 10 µm. For low fluid velocity, size-dependent (bright blue) and constant (dark blue) crystal velocity, and different tube lengths.

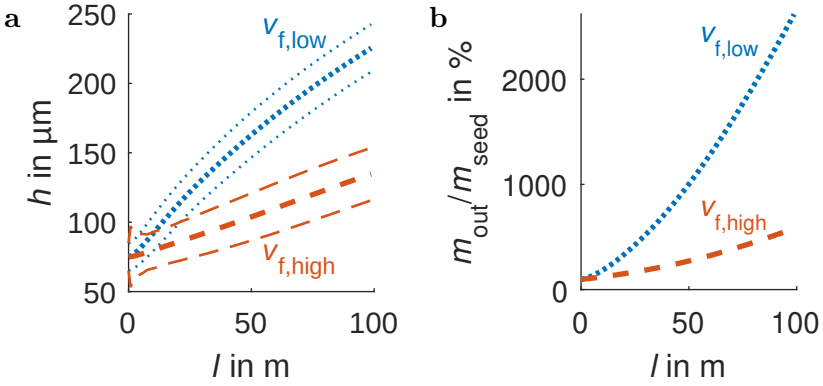

Figure 6.11: Growth simulation for varying tube length for size-dependent v_p at $v_{f,low}$ (blue, dotted) and $v_{f,high}$ (orange, dashed). Conditions as in Figure 6.10. (a) Number based mean size and standard deviation; (b) product to seed crystal mass.

a different choice of cooling medium may increase the growth. The initial supersaturation is already high, such that T_{out} should not be decreased further to avoid nucleation. Operating at different inlet and saturation temperatures is possible but limited. There is an upper temperature limit for tubing and equipment at approximately 330 K. For the solvent water, the freezing point of 273.15 K is a natural lower temperature bound. For a fixed supersaturation, the growth rate increases with temperature. Hence, a low temperature range is not advisable from a yield perspective. For a fixed temperature difference, stronger growth is reached at higher temperatures. Operation at higher temperatures may be costly since it requires more heat to heat up the feed solution and it requires better insulation along the tube, but it increases the growth rate and yield.

6.4.2 Simulations for Continuous Seeding

As pointed out in the previous sections, tubular crystallizers offer the advantage of rather homogeneous residence time distributions. Hence, they are especially suitable for continuous operation with a continuous supply of seeds. In this section, the effect of different

geometry and operation parameters on the CSD and yield is studied via simulations. The same parameters as in Section 6.4.1 are applied, where the seed distribution is fed once per second. Three process options are considered that differ in the average fluid velocity and in the crystal seed mass flow rate, as listed in Table 6.5. Process 1 can be considered as reference case. When the average fluid flow rate is increased, two process options may come into effect. Process 2 occurs when a solution of constant concentration is fed at a higher flow rate, but a separate stream of seed suspension at a high suspension density is supplied at an unchanged rate. In process 3, a suspension is produced in upstream processes and is fed directly to the HCT. In this process, the increase in the seed crystal mass flow rate is proportional to the raise of the average fluid velocity, compared with process 1.

The tube length is discussed. As expected, increasing the tube length increases the mean product crystal size, as illustrated in Figure 6.12a. Simultaneously, there is a slight increase in the width of the initial normal distribution. The distribution width is considered as the standard deviation of the CSD in Figure 6.12b. Compared with batch seeding, the product crystal size attains saturation at increasing tube length in Figure 6.12a. From a certain tube length on, exceeding the length further does not lead to an increase in the product size, because the supersaturation is depleted, as illustrated in Figure 6.12c.

Now, the effect of v_f is evaluated. The largest mean crystal size is reached for $v_\mathrm{f,low}$, when the tube has a length below 87 m, as depicted in Figure 6.12a. As the suspension is slower at $v_\mathrm{f,low}$, the supersaturation is depleted within a shorter length of the tube, compared with $v_\mathrm{f,high}$. For longer tubes, the largest mean crystal size is reached in process 2. Comparing process options 2 and 3, a higher seed mass of the same distribution leads to a higher surface area for growth, to a stronger depletion of the supersaturation (see Figure 6.12c), and to smaller product crystals (see Figure 6.12a). The same could be observed for a different process with the same seed mass flow rate, but smaller crystals. The width of the product CSD is similar in all processes (see Figure 6.12b). Comparing the process options with regard to the product to seed mass ratio, which is shown in Figure 6.12d, the qualitative trends are the same as for the mean crystal size. The product to seed mass ratio does not consider the amount of supplied solution. Hence, another yield expression is applied. The yield η is defined as the ratio of crystallized mass flow rate to the mass flow rate of hydrate that was fed to the system

$$\eta = \frac{\int_{h_\mathrm{min}}^{h_\mathrm{max}} k_V \rho_\mathrm{p} \dot{f}_\mathrm{out} h^3 - \dot{m}_\mathrm{seed}}{\frac{\dot{m}_\mathrm{f,anh,in}}{\chi_\mathrm{anh}} + \dot{m}_\mathrm{seed}}$$

where $\dot{f}_\mathrm{out}$ is the rate of the crystal distribution that leaves the HCT at steady state. In the denominator, solid and liquid feed are added up. The boundary conditions for the liquid phase remain as in the previous section. At different average fluid velocities,

Table 6.5: Process options that are shown in Figure 6.12. The values of the process parameters can be found in Table 6.1.

Process	v_f	$\dot{m}_\mathrm{seed}$	Linestyle
Process 1	$v_\mathrm{f,low}$	$\dot{m}_\mathrm{seed,low}$	·····
Process 2	$v_\mathrm{f,high}$	$\dot{m}_\mathrm{seed,low}$	———
Process 3	$v_\mathrm{f,high}$	$\dot{m}_\mathrm{seed,high}$	- - - - -

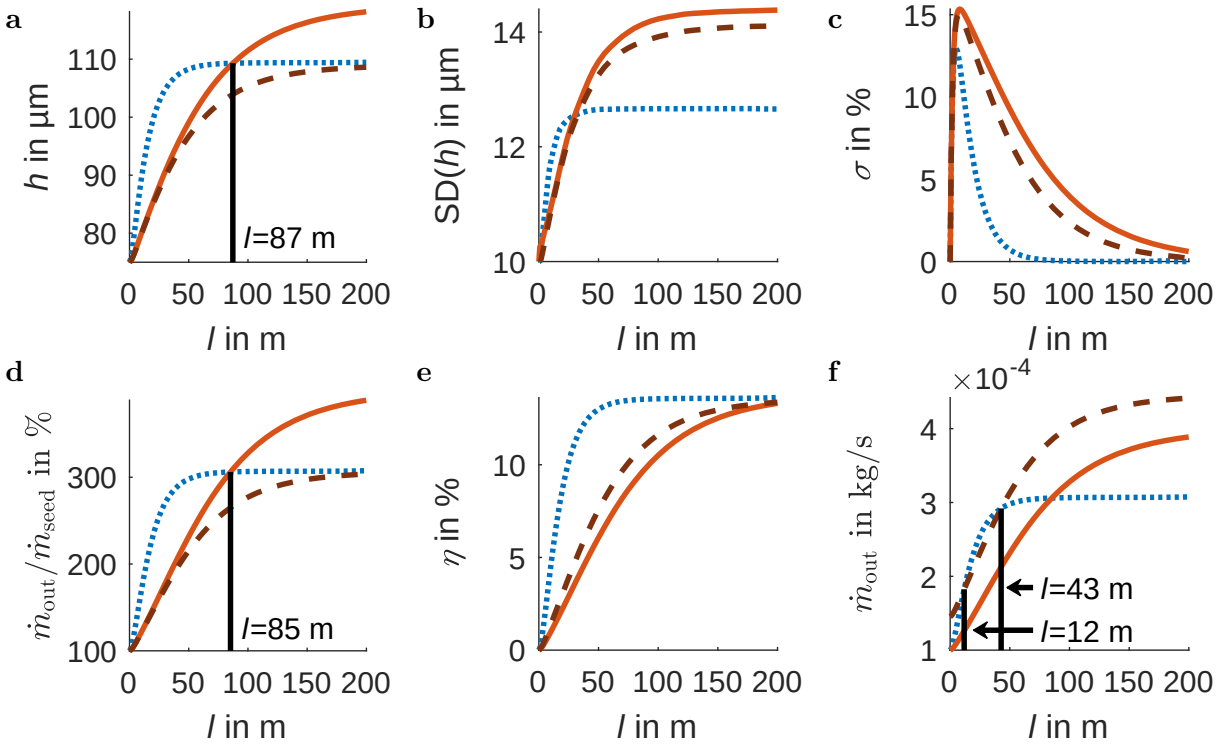

Figure 6.12: Growth simulation for continuous seeding of a normal seed distribution of the mass flow rate $\dot{m}_{\mathrm{seed,small}}$, for size-dependent v_{p}, and for varying tube length. Process 1 (blue, dotted), process 2 (orange, solid), and process 3 (brown, dashed) at steady state. (a) Number based mean product size; (b) standard deviation of the number based mean product size; (c) supersaturation at the tube outlet; (d) product to seed crystal mass flow ratio; (e) yield; (f) product crystal mass flow rate.

different amounts of hydrate are fed in the liquid phase. The resulting mass flow rates at $v_{\mathrm{f,low}}$ are $\dot{m}_{\mathrm{f,anh,in}} = 7.7 \times 10^{-4}\,\mathrm{kg\,s^{-1}}$, $\dot{m}_{\mathrm{f,w,in}} = 6.7 \times 10^{-3}\,\mathrm{kg\,s^{-1}}$, and at $v_{\mathrm{f,high}}$ they are $\dot{m}_{\mathrm{f,anh,in}} = 1.1 \times 10^{-3}\,\mathrm{kg\,s^{-1}}$, $\dot{m}_{\mathrm{f,w,in}} = 9.8 \times 10^{-3}\,\mathrm{kg\,s^{-1}}$. Hence, qualitatively, the yield curves are similar to the product to seed mass ratio curves, but they are scaled differently in Figure 6.12e. When a loss of hydrate mass needs to be kept as low as possible, $v_{\mathrm{f,low}}$ should be preferred up to approximately 200 m tube length (see Figure 6.12e). For very long tubes ($l \geq 200\,\mathrm{m}$), the yield reaches 14 % in all process options. For these long tubes, more absolute mass can be crystallized at $v_{\mathrm{f,high}}$ and it should be preferred, as illustrated in Figure 6.12f. When only the mass of crystals at the outlet is of interest, process 3 is superior for very short and very long tubes, as depicted in Figure 6.12f. For intermediate tube lengths, process 1 delivers a slightly higher crystal mass. For a tube length of 200 m, the total product crystal mass leaving the tube in 24 h is 27 kg in process 1, 34 kg in process 2, and 38 kg in process 3.

The results are summarized in Table 6.6. For the given temperature profile, a tube of approximately 50 m length operated at a low fluid flow rate fulfills most process goals very well. The highest product mass flow rate can be reached with process option 3. The rate is just slightly larger than that for process 1, and process 1 is optimal regarding all the other criteria. Hence, process 1 should be selected.

The pressure loss increases with tube length according to Eq. (5.2), hence, shorter tubes should be preferred. Mishra and Gupta (1979) give a correlation for the friction factor

Table 6.6: Process goals and selected process in dependence of the tube length.

	Best process		
Process goal	Process 1	Process 2	Process 3
Largest crystals	$l \leq 87\,\mathrm{m}$	$l > 87\,\mathrm{m}$	–
Highest $\dot{m}_{\mathrm{out}}$	$12\,\mathrm{m} < l \leq 43\,\mathrm{m}$	–	$l \leq 12\,\mathrm{m}; l > 43\,\mathrm{m}$
Highest ratio $\frac{\dot{m}_{\mathrm{out}}}{\dot{m}_{\mathrm{seed}}}$	$l \leq 85\,\mathrm{m}$	$l > 85\,\mathrm{m}$	–
Highest yield η	for all l	–	–

that is valid in case of laminar flow, for $1 < Re\sqrt{2R/d_{\mathrm{c}}}$ in a coiled tube. Transforming their Fanning friction coefficient to the Darcy friction coefficient, the correlation is

$$\lambda_{\mathrm{friction}} = \frac{64}{Re}\left(1 + 0.033\left(\log_{10} Re\sqrt{\frac{2R}{d_{\mathrm{c}}}}\right)^4\right)$$

At $v_{\mathrm{f,low}}$, the loss caused by the fluid in HCTs of 50 m and 200 m length would attribute to 3×10^4 Pa and 1.1×10^5 Pa. The experimental setups in Chapter 4 have a length between 33 m to 35 m. Regarding those setups, the maximum pressure loss is reached in setup a where Δp is 2×10^4 Pa at $v_{\mathrm{f,low}}$, and 4×10^4 Pa at $v_{\mathrm{f,high}}$. The pressure drop was measured with a differential pressure transmitter based on a piezoresistive stainless steel sensor (IDM 331 with an IPA 430 display, ICS Schneider Messtechnik GmbH, Hohen Neuendorf) in the HCT, without particles in water at room temperature. The pressure drop between the seed position and directly behind the Qicpic reached values from 2×10^4 Pa to 3×10^4 Pa for mass flow rates from $6.5\,\mathrm{g\,s^{-1}}$ to $9.2\,\mathrm{g\,s^{-1}}$. The range of mass flow rates comprises the mass flow rate of potash alum at $v_{\mathrm{f,low}}$, and it is slightly below the rate corresponding to $v_{\mathrm{f,high}}$.

Regarding the setups in Chapter 4, all process goals can be reached best by process option 1. Although process 1 at $v_{\mathrm{f,low}}$ is preferable here, there is a lower limit of Re to avoid crystal sedimentation and fouling. Hohmann et al. (2018) report different regimes of particle fluidization in vertical tubes. They differentiate stagnant sediment, moving sediment flow, and homogeneous suspension flow. They confirm that segregation increases with the solid-to-liquid density ratio. Hohmann et al. (2016a) presented a short-cut method to calculate a cut-size diameter as a limit to keep crystals fluidized. Their correlation is valid for small Re_{p} and should be applied, especially to vertical HCTs, where gravitational settling may be severer.

Farias et al. (2019) simulated nucleation and growth in a combined cooling/antisolvent crystallization of Lovastatin in a continuous coaxial mixer. Different types of product distributions resulted. Depending on the inlet feed velocity, they observed unimodal or bimodal distributions. Also for potash alum, different distributions may be produced in upstream crystallization. These distributions can be applied as seed crystals and can be grown further in a HCT.

So far, a narrow normal distribution of seeds was applied in the simulations. Now, the growth of a broader bimodal seed distribution is investigated, regarding the mean and the width of the product CSD. As before, the tube is fed with $1 \times 10^{-4}\,\mathrm{kg\,s^{-1}}$ of a normal seed distribution with a mean of 75 µm and a standard deviation of 10 µm, and additionally with $2 \times 10^{-4}\,\mathrm{kg\,s^{-1}}$ of a normal distribution with a mean of 150 µm and a standard deviation of 10 µm, as illustrated in Figure 6.13a. The inflow rate of the unimodal number density distribution of seed crystals in the previous simulations agrees

with the first peak of the curves in the figure.

For long tubes, the product mean size is again the highest in process 2, as illustrated in Figure 6.13b. For a tube length of 200 m, the mean size increases by 22 µm in process 3, by 23 µm in process 1, and by 30 µm in process 2. For all process options, the standard deviation of the bimodal initial distribution decreased slightly from 32 µm, whereas the standard deviation of the CSD increased slightly during growth for the narrow unimodal normal distribution in Figure 6.12b. Hence, as expected for the size-dependent particle velocity, there is a slight narrowing of the CSD for a broad initial distribution.

Next to the tube length and the seed distribution at the inlet, the temperature profile can be adjusted to influence the product CSD. When the temperature of the cooling medium and all other parameters are fixed, the product size is limited by the solubility of the material. As shown in Figures 6.12c, saturation was nearly reached by extending the tube length in the previous simulations. The supersaturation and, thus, the driving force for crystal growth can be maintained when the outlet temperature is lower for longer tubes. In this case, nucleation should be avoided during the start up of the device and the outlet temperature should be lowered slowly. This increases the time until the steady state is reached and reduces the overall yield if the start up is included. In the previous simulations, for a tube length of 200 m, 21 min to 22 min were required to reach steady state at $v_{\mathrm{f,high}}$ and 71 min were required at $v_{\mathrm{f,low}}$. The transient time was similar to the residence time of the slowest crystals. For the same tube length, the crystal residence time was 18 min to 21 min at $v_{\mathrm{f,high}}$ and 55 min to 70 min at $v_{\mathrm{f,low}}$ depending on the crystal size.

6.5 Summary of the Chapter

The first question, which was raised in the introduction of this chapter, addressed the necessity of a size-dependent particle velocity in the model. A simplified model for the particle velocity can predict the residence time well, when there is negligible growth. For growth conditions, the size-dependent crystal velocity should be measured and applied in the model. The range of measured crystal velocities should cover not only the initial crystal sizes, but also the large product sizes. When a preliminary measurement is not possible, the average fluid velocity can be an estimate for the lower and upper bound.

Especially for very short tubes, a tube extension is useful to increase the mean product size, product mass, and yield. For the presented conditions, a considerable increase was observed for tube lengths of at least 20 m. For batch seeding, an increase in tube lengths is always advantageous regarding final mean size and product mass, whereas it is disadvantageous regarding yield and pressure drop.

The results for continuous seeding are summarized in the following. An increase of the tube length above 50 m for the low fluid flow rate or above 200 m for the high flow rate is not reasonable. At these lengths, the supersaturation is depleted and the mean crystal size and product mass are approximately constant. The given values for the tube length increase when the same inlet temperature, but a lower cooling temperature, is applied. Comparing the fluid flow rates qualitatively, the same trends should be observed for lower cooling temperatures. Broad distributions may be narrowed when different temperature profiles, for example temperature cycles, are applied. Regarding the fluid flow rates, the low flow rate should be preferred for short tubes up to tube lengths of approximately 85 m. For longer tubes, the achievable mean product size and product mass are higher when only the fluid flow rate is increased. Nevertheless, the tube length should only be increased further if a high product mass is desired. Increasing tube length, the gain in

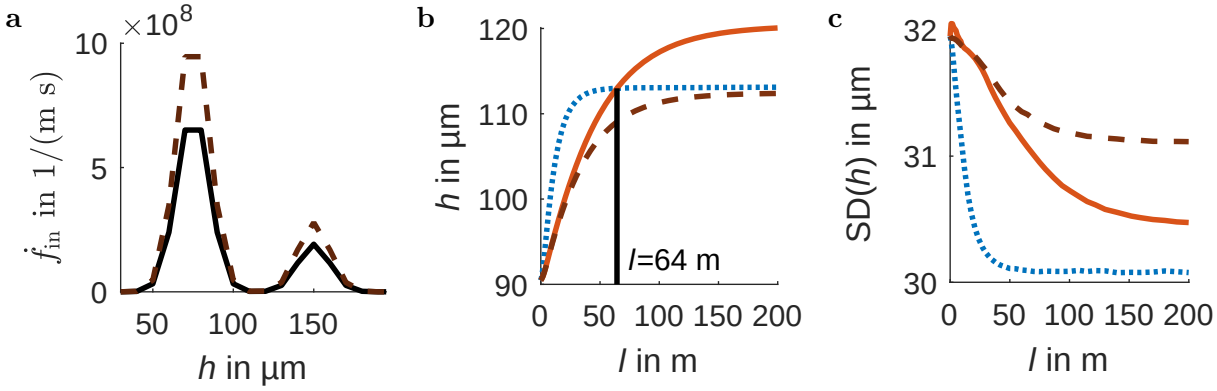

Figure 6.13: Growth simulation for continuous seeding of a bimodal seed distribution, for size-dependent v_p, and for varying tube length. Process 1 (blue, dotted), process 2 (orange, solid), and process 3 (brown, dashed) at steady state. (a) Inflow rate of the number density distribution of seed crystals for the mass flow rates $\dot{m}_{\text{seed,mix,low}}$ (black solid) and $\dot{m}_{\text{seed,mix,high}}$ (brown dashed); (b) number based mean product size; (c) standard deviation of the number based mean product size.

mean size is small, the yield is similar, and practical issues like pressure drop, cleaning, and clogging issues may worsen. All in all, a lower fluid flow rate should be preferred in most cases, but it should be sufficiently high to avoid sedimentation of the product crystals.

At high fluid flow rates, a simultaneous increase in the seed mass leads to a faster decay of the supersaturation. For very short tubes this is advantageous and a higher yield can be achieved. For tube lengths above approximately 50 m at $v_{f,\text{high}}$, an increase in seed mass is disadvantageous for most objectives. Even though the yield is slightly higher, the mean product size and the product mass decrease.

The width of the CSD stayed approximately constant in all simulations. It broadened slightly for narrow initial distributions and narrowed slightly for broad initial distributions. In particular, it increased by up to 4 µm and decreased by up to 2 µm, which is 6 % to 9 % of the increase in the mean size. This effect is expected to be outweighed by growth rate dispersion in experiments.

In Section 4.4, an outlook was given to the extension of the study to multivariate CSSDs. From a modeling point of view, the starting point is the multivariate PBE in Eq. (6.1) and an identical framework of multivariate equations can be derived. A challenge is that the particle-size dependent velocities have to be interpolated and extrapolated for the whole internal coordinate space from experiments. Virtual faces have to be dealt with. The solution of the system becomes numerically expensive as the number of states increases strongly upon discretization.

Further questions, which could be answered via simulations, but were out of the scope of the analysis, are:

- When constructing a HCT for batch-seeded experiments at a given RT, it could be determined beforehand whether to prefer higher flow rates in a longer tube or lower flow rates.

- What is the maximum inlet temperature to avoid dissolution? For predictions, the

feed was close to saturation.

- Growth of another substance, such as the bivariate KDP, could be simulated with the existing model and corresponding solubility and kinetics.
- A comparison to other crystallizers would be possible but requires additional modeling.

7 Summary

In the following summary the seven main achievements of this dissertation are presented and explained.

1. In straight tubes, large particle-to-fluid residence time ratios were observed for laminar flow. Mixing is not sufficient for crystallization at laminar conditions in straight tubes. It is recommended to apply helically coiled flow tubes to improve the mixing.

Residence time distributions of particles were measured in straight and coiled tubes (see Chapters 3 and 4). Experiments were performed with spherical particles and angular crystals at varying laminar flow rates. Particles were always slower than the fluid. As expected from the fluid flow field, the particle residence time distribution was more narrow in coiled tubes than in straight tubes, due to improved radial mixing. Straight tubes have broad fluid residence time distributions, which narrow for helically coiled flow tubes, and nearly approach plug flow in coiled flow inverters. In curved tubes, local differences in the solution concentration are avoided by radial mixing. Mixing further improves with the average fluid velocity.

2. The residence time distribution of particles in helically coiled flow tubes was characterized. The emergence of a particle-size-dependent residence time at laminar flow in tubes was observed, explained, and responsible forces were identified.

Experiments have shown for all aforementioned setups and operation conditions that large spherical particles and angular crystals were faster than smaller ones. Experiments had been performed with particles of higher density when compared with the solution. In Chapter 5, a momentum balance model was developed for a straight tube to validate the experiments. Single particle simulations confirmed that, as soon as a density dissimilarity between particles and fluid exists, a difference in residence time between particles of varying sizes appears. In the simulations, also, large particles spent less time in the tube than small particles. The simulations indicated that, for small particles below the experimental sizes of 100 µm, the residence time decreases again. This is confirmed by the Stokes number of these very small particles, which suggests that they follow the fluid flow easily.

The model can also be deployed to identify forces causing the observed size-dependent residence time. The momentum balance was derived for spherical particles in a straight tube. The relevant forces were the drag as well as the gravitation and buoyancy forces, whereas the Saffman lift was insignificant. The residence time distribution is a result of the forces acting on particles in a fluid. For this kind of residence time distribution to occur, the fluid has to be characterized by variations of the axial velocity in the cross-section of the tube. Because of the observation of a size dependency in both tube types, it is assumed that the same forces determine the residence time distribution in the helically coiled flow tube.

Qualitatively, the model-based simulations reproduced the size-dependent residence time that had been observed experimentally. Quantitatively, there were still differences

between the residence time distribution in the experiments and in the simulations. The agreement may be improved by an angular momentum balance in the model. At high angular velocities, particle rotation lifts particles. Consequently, they reach regions of higher axial fluid velocity affecting their residence time distribution.

For validation in helically coiled flow tubes, the existing fluid velocity profile, which was averaged in time and along the tube axis, could be applied to the model of an inclined straight tube. A general functional dependence of the particle velocities contingent on the average fluid velocity has not been derived. Instead, more advanced numerical simulations including an angular momentum balance and particle-particle collisions could also be applied for validation.

This was not the first effort to measure and simulate particle residence times in horizontal helically coiled flow tubes. However, not only spherical particles, but also angular crystals, have been studied. In addition, the results may be relevant to other solid-liquid processes in which irregular particles appear, such as food particle transport. The new observation of a size-dependent residence time is usually not recognized in population balance models and has not yet been studied for crystals, neither experimentally nor by advanced numerical simulations. Redlinger-Pohn et al. (2016b) reported a size-dependent residence time for fibers in experiments and simulations with helically coiled flow tubes, but they attributed it to flocculation of the fibers.

3. The wall material of the helically coiled flow tubes had no significant influence on the crystalline product. The flow direction, that is, upward or downward flow, was neither a significant parameter, as the tubes were nearly horizontal in both cases.

Different tube wall materials, in particular glass and silicone, were used for the straight tubes and the helically coiled flow tubes. A size dependency of the residence time was observed experimentally for both materials. Simulations with the model from Chapter 5 confirmed that a change in the wall collision coefficients for different wall materials had a negligible effect on the wall collisions; thus, on the particle residence time.

4. The particle-size-dependent residence time has the potential to decrease the width of crystal size distributions that are initially broad.

Plug flow is not reached in helically coiled flow tubes, nonetheless, this may be advantageous for crystal growth. The particle-size-dependent residence time offers the potential to narrow the crystal size distribution during crystal growth, because small crystals stay in the tubes longer and have more time to grow.

5. The width of the applied initial crystal size distributions increased from inlet to outlet by maximum 9 % with regard to the increase in the mean size.

As long as no nucleation occurred, batch experiments in tubes of lengths from 33 m to 35 m confirmed that the width of the crystal size distribution stayed nearly constant although potash alum exhibits growth rate dispersion. Thus, the residence time difference outweighed the growth rate dispersion experimentally as verified by simulations in Chapter 6.

When a substance tends to aggregate or to exhibit growth rate dispersion the distribution cannot be narrowed, but at least broadening of the crystal size distribution is reduced. Simulations have shown that very small, compared to intermediate size, particles are fast and follow the flow. This observation is important in case of nucleation. As a consequence,

small nuclei do not grow sufficiently; they grow even less the farther away they nucleate from the tube inlet. Consequently, they broaden the crystal size distribution. Nucleation should be avoided or fine particles should be dissolved intermittently.

6. During continuous crystallization in helically coiled flow tubes, several process goals are reached simultaneously. Broadening of the crystal size distribution is possible to be prevented, while producing a high mass of crystals at a high yield, considering the solute in the liquid phase.

Suitable conditions for continuous crystallization in helically coiled flow tubes were identified in Chapter 6. For this purpose, a model was developed, which is premised on the experimentally observed crystallization phenomena. It was parameterized on the basis of experimental measurement data and it relied on kinetics from literature. The full crystal size distribution information was obtained from a population balance equation. It was coupled to the continuous phase balances. The growth simulations and the growth experiments for batch seeding agreed well. Simulations of continuous seeding demonstrated that an operation at low average fluid velocities is advantageous to produce a large mass of large crystals with high yield.

7. It was estimated how different operation parameters affect the product crystal size distribution, product mass, and yield for batch and continuous seeding.

The longer the tube, the better the supersaturation can be depleted, but the higher the pressure drop. For laminar flow rates in the given setups, a tube length of approximately 50 m was identified as a productive dimension resulting in large crystals, product mass and yield. The width of a normal seed crystal size distribution increased only slightly with the final mean crystal size, independent of the flow rate. For a bimodal seed crystal size distribution, there was a slight decrease in the width of the crystal size distribution during growth. In terms of flow rates, low flow rates should be preferred to realize short tubes and to deplete the supersaturation. The lower limit of the tube length is determined by the sedimentation of crystals. It is unnecessary to apply flow rates in the transient or turbulent regime. When the seed mass is varied, the cooling profile and the tube length should be adjusted. For suspension densities outside of the dilute regime, the residence time distribution is affected according to Legrand et al. (2007) and uniform beds may form at high suspension densities. For high suspension densities, studies have been performed in the area of food processing.

Outlook

The experimental workflow that was applied in this study is recommended for the characterization of devices that are new to crystallization. For model parameterization, a setup should be investigated experimentally, starting with the fluid residence time distribution and the particle residence time distribution without growth before crystallization. Next, pure growth conditions should be approached before studying further phenomena. These phenomena may be aggregation at high suspension densities or secondary nucleation at high supersaturations.

The findings in this dissertation are intended to provide guidance to prevent clogging in tubes during crystallization. For liquid-solid phase transport in tubes at low flow rates, priority should be given to horizontal coils over vertical coils. This is supported by a

report of Hohmann et al. (2019). They studied flow regimes in nearly vertical tubes and observed that a stagnant sediment may occur and lead to blocking of tubes when particles are too slow. Furthermore it is mentioned that vertical coils may be advantageous for substances that tend to aggregate at higher velocities in the homogeneous suspension flow regime.

In preliminary setups, which were tested for the present dissertation, the following two parts caused clogging: First, cold zones and cold bridges. They appeared where measurement tools had been used, e.g., at the flow-through cell and at metal temperature sensors. Second, internal structures like connectors. They led to dead zones that may have trapped crystals. Nevertheless, there are options available to measure the temperature profile or to parameterize an energy balance. A duplicate setup with temperature sensors may be built and tested without crystals. Using flexible tube material, the outlet temperatures may be measured repeatedly for tubes of different lengths. While a detailed discussion would exceed the scope of this dissertation, the possibility to optimize the temperature profile by modeling the heat transfer shall be mentioned.

In future, the setup might be applied for the crystallization of other substances, e.g., feedstuff like methionine and pharmaceuticals like paracetamol. For some substances in food industries, only a small number of crystals of a defined crystal size distribution are required. In particular, Hartel (2002) mentions refined salt and sugars, such as sucrose and lactose, and the crystallization of organic acids, such as citric acid. In these cases, a helically coiled flow tube could be applied to crystallize foods, when their production involves a cooling crystallization step.

To further change the crystal size distribution, alternating growth and dissolution sections in helically coiled flow tubes could be applied. Besenhard et al. (2017) changed crystal size distributions dissolving fine particles in an helically coiled flow tube that was immersed in a hot and a cold cooling bath. In future simulations, the lengths of the heated and cooled helically coiled flow tubes sections could be optimized to reach a desired crystal size distribution. Even crystal size and shape distributions can be changed exploiting shape-specific growth and dissolution rates. In a batch crystallizer, Eisenschmidt et al. (2016) performed growth and dissolution cycles to change the shape of a bivariate potassium dihydrogen phosphate crystal population. In this case, an optimal saturation was applied and controlled to reach a desired average crystal shape. The same saturation profiles could be applied in helically coiled flow tubes along the tube length. As faster cooling is possible in tubes, the profiles could be further optimized to enable shorter tube lengths.

Helically coiled flow tubes were applied as tube flow fractionators for fibers (Redlinger-Pohn et al., 2016b) and may also be applied as fractionators for crystals. In future research, the residence time distribution and hydrodynamics of crystals of different shapes in helically coiled flow tubes could be analyzed experimentally or via advanced numerical simulations at varying laminar flow rates. If residence times differ with shape, the device could be applied as a classifier. Further, there are polymorphs with varying shapes, such as α and β L-glutamic acid, and the anhydrous $CaCO_3$ polymorphs vaterite and calcite. In this case, the separation of polymorphs or enantiomers of different shapes might be intensified. Fractionation could be realized during or after a crystallization step in helically coiled flow tubes by intermittent seeding of a helically coiled flow tube.

The first continuous crystallizers were developed for large-scale production. Later, small-scale production led to the increased use of batch and semi-batch crystallizers. Since the turn of the millenium, interest in continuous crystallizers for small-scale applications

has increased. However, if a scale-up is desired, tube bundle crystallizers might be applied with several parallel helically coiled flow tubes.

A Solver Selection and Time Step Adjustment in the Straight Tube Force Model

Regarding the time step, simulations were performed for different fixed time steps and for an adjusted time step. Without adjustment, the time step remained unchanged

$$\Delta t\,(n_t + 1) = \Delta t\,(n_t)$$

Considering simulations with fixed time steps, time steps of 2×10^{-4} s, 1×10^{-4} s, 5×10^{-5} s, 2×10^{-5} s and 1×10^{-5} s were tested subsequently for each particle size. Large time steps allow faster computation. Consequently, the largest time step, at which convergence could be reached, was selected. When reducing the time step even further, the difference in the resulting particle RT was maximum 1 %. The time step Δt, where convergence was reached, was 1×10^{-4} s for particles of a diameter of 400 µm, 350 µm, 250 µm and 200 µm, 5×10^{-5} s for particles of a diameter of 250 µm, 2×10^{-5} s for particles of a diameter of 200 µm, 150 µm and 125 µm, and 1×10^{-5} s for particles of a diameter of 100 µm.

In the forward simulations with adjustment, the time step was reduced after a wall contact to prevent the normal velocity from becoming too large. In particular, when a particle touches the wall, the current time step is interrupted at the moment of the wall touch. The velocity in the moment of reflection is used to calculate the velocity for the moment directly after reflection by reversing the sign and applying Eq. (5.13). This leads to a very high normal velocity at the next wall collision. To avoid this, the time step is reduced if not only a wall collision had appeared in the second last time steps but also $\Delta z\,(n_t) < 0.25 \Delta z\,(n_t - 1)$. For the second condition, different factors were tested and the factor of 0.25 was selected. The new time step is

$$\Delta t\,(n_t + 1) = \Delta t\,(n_t)\,\frac{\Delta z\,(n_t)}{\Delta z\,(n_t - 1)}$$

where

$$\begin{aligned} \Delta z\,(n_t) &= z\,(n_t + 1) - z\,(n_t) \\ \Delta z\,(n_t - 1) &= z\,(n_t) - z\,(n_t - 1) \end{aligned}$$

and where $n_t - 1$ is the previous time step, n_t is the current time step, and so forth. The flexible algorithm reduced the step size only for those Δt where no convergence was reached with a fixed step size. The value of Δt at the end of the simulations with the adjustable time step did not fall below 1×10^{-5} s for the mentioned particle sizes.

To validate the choice of the time step, the RTs that were achieved with the forward implementation from Eqs. (5.10) to (5.12) were compared to results achieved with an explicit fifth-order Runge-Kutta “ode45” solver (MATLAB), for particles starting at the

origin. For the adjustable time step, the RT calculated with the forward implementation exceeded that of the ode45 solver by maximum 1.1 %, and for a fixed Δt of 1×10^{-5} s the RT increased by maximum 0.4 %. In either case, the simulations were performed at $v_{\mathrm{f,low}}$, which was specified in Section 5.4. All in all, the deviations are small and the results with both solvers can be considered as identical.

B Algorithm for the Wall Collision in the Straight Tube Force Model

In the following, the velocities after wall collision are described for a particle movement in normal direction to the tube wall. Then, the movement in a random direction is described for particles that touch the wall in the first quadrant of the xy-plane.

The absolute value of the velocity remains unchanged before (b) and after (a) collision and it is

$$|v_\mathrm{p}| = \left|v_\mathrm{p}^\mathrm{a}\right| = \left|v_\mathrm{p}^\mathrm{b}\right| = \sqrt{{v_{\mathrm{p},x}^\mathrm{b}}^2 + {v_{\mathrm{p},y}^\mathrm{b}}^2}$$

In all cases, the azimuth α_p of the particle position is derived using

$$\alpha_\mathrm{p} = \arccos\frac{x}{R}$$

Negative angles are transformed by

$$\alpha_\mathrm{p} = \alpha_\mathrm{p} + 2\pi$$

The azimuth α_v of the velocity before collision is

$$\alpha_v = \arccos\frac{v_{\mathrm{p},x}^\mathrm{b}}{|v_\mathrm{p}|}$$

A wall contact with a radial particle velocity v_p^b before collision appears when $\frac{v_{\mathrm{p},x}^\mathrm{b}}{v_{\mathrm{p},y}^\mathrm{b}} = \frac{x}{y}$. Then, the particle velocity v_p^a after collision is

$$v_{\mathrm{p},x,\mathrm{elastic}}^\mathrm{a} = -v_{\mathrm{p},x}^\mathrm{b}$$
$$v_{\mathrm{p},y,\mathrm{elastic}}^\mathrm{a} = -v_{\mathrm{p},y}^\mathrm{b}$$

The angle β between the radial orientation and the velocity vector vanishes. The azimuths of the particle position α_p and the velocity vector α_v are identical. When the velocity v_p^b is not radial, there are four different cases, depending on the direction of v_p^b, which are shown in Figure B.1 for the first quadrant. For particles in the other quadrants, a transformation to the first quadrant is applied before the case-by-case analysis. To discriminate the four cases, sufficient conditions and the resulting velocities after collision v_p^a are given in Table B.1. The transformation to the first quadrant for the other quadrants is shown in Table B.2.

Correction Algorithm When a Particle Leaves the Tube

The algorithm for the correction of the new position and velocity is given for the case that the particle leaves the tube within a time step, and the point of wall touch is identified.

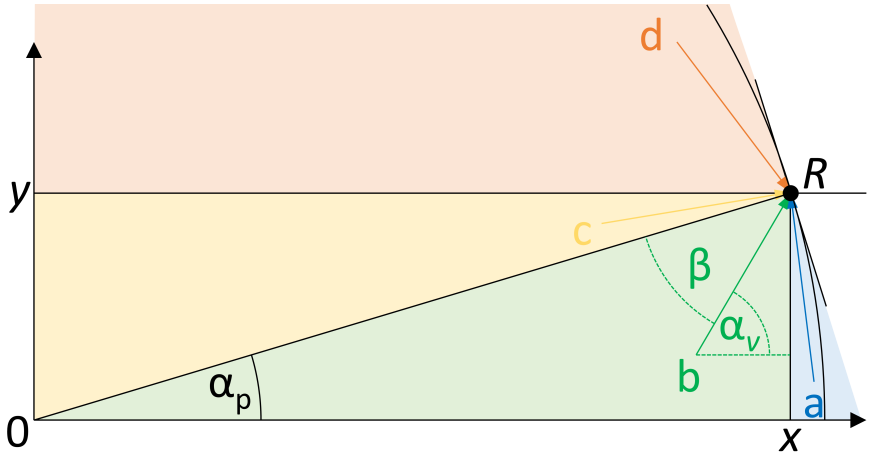

Figure B.1: Types of velocity vector orientations before collision in the first quadrant.

Table B.1: Conditions for each case and velocity components after collision in the first quadrant. The additional conditions on the azimuth of the velocity vector in the headlines discriminate vectors below (cases a and b) and above (cases c and d) the radial vector orientation.

Case	Condition	Angle	Velocity components
	$\alpha_\mathrm{p} < \alpha_v \leq \alpha_\mathrm{p} + \pi/2$		
a	$v^\mathrm{b}_{\mathrm{p},x} \leq 0$	$\beta = \pi - \alpha_\mathrm{p} - \arcsin \frac{\lvert v^b_{\mathrm{p},y}\rvert}{\lvert v_\mathrm{p}\rvert}$	$v^a_{\mathrm{p},x,\mathrm{elastic}} = -\lvert v_\mathrm{p}\rvert \cos(\alpha_\mathrm{p} - \beta)$ $v^a_{\mathrm{p},y,\mathrm{elastic}} = -\lvert v_\mathrm{p}\rvert \sin(\alpha_\mathrm{p} - \beta)$
b	$v^\mathrm{b}_{\mathrm{p},x} > 0,\ v^\mathrm{b}_{\mathrm{p},y} > 0,$ $\frac{\lvert v^\mathrm{b}_{\mathrm{p},x}\rvert}{\lvert v^\mathrm{b}_{\mathrm{p},y}\rvert} < \frac{x}{y}$	$\beta = -\alpha_\mathrm{p} + \arcsin \frac{\lvert v^b_{\mathrm{p},y}\rvert}{\lvert v_\mathrm{p}\rvert}$	$v^a_{\mathrm{p},x,\mathrm{elastic}} = -\lvert v_\mathrm{p}\rvert \cos(\alpha_\mathrm{p} - \beta)$ $v^a_{\mathrm{p},y,\mathrm{elastic}} = -\lvert v_\mathrm{p}\rvert \sin(\alpha_\mathrm{p} - \beta)$
	$\alpha_\mathrm{p} - \pi/2 \leq \alpha_v < \alpha_\mathrm{p}$		
c	$v^\mathrm{b}_{\mathrm{p},x} > 0,\ v^\mathrm{b}_{\mathrm{p},y} > 0,$ $\frac{\lvert v^\mathrm{b}_{\mathrm{p},x}\rvert}{\lvert v^\mathrm{b}_{\mathrm{p},y}\rvert} > \frac{x}{y}$	$\beta = \alpha_\mathrm{p} - \arcsin \frac{\lvert v^b_{\mathrm{p},y}\rvert}{\lvert v_\mathrm{p}\rvert}$	$v^a_{\mathrm{p},x,\mathrm{elastic}} = -\lvert v_\mathrm{p}\rvert \cos(\alpha_\mathrm{p} + \beta)$ $v^a_{\mathrm{p},y,\mathrm{elastic}} = -\lvert v_\mathrm{p}\rvert \sin(\alpha_\mathrm{p} + \beta)$
d	$v^\mathrm{b}_{\mathrm{p},y} \leq 0$	$\beta = \alpha_\mathrm{p} + \arcsin \frac{\lvert v^b_{\mathrm{p},y}\rvert}{\lvert v_\mathrm{p}\rvert}$	$v^a_{\mathrm{p},x,\mathrm{elastic}} = -\lvert v_\mathrm{p}\rvert \cos(\alpha_\mathrm{p} + \beta)$ $v^a_{\mathrm{p},y,\mathrm{elastic}} = -\lvert v_\mathrm{p}\rvert \sin(\alpha_\mathrm{p} + \beta)$

Table B.2: Transformation of coordinates and velocities to the first quadrant (I).

2nd Quadrant	3rd Quadrant	4th Quadrant
$\frac{\pi}{2} < \alpha_\mathrm{p} \leq \pi$	$\pi < \alpha_\mathrm{p} \leq \frac{3}{2}\pi$	$\frac{3}{2}\pi < \alpha_\mathrm{p} \leq 2\pi$
The angle of the velocity is corrected if		
$\alpha_v < -\pi/2$	$\alpha_v < 0$	$\alpha_v < \pi/2$
Then, $\alpha_v = \alpha_v + 2\pi$ for all quadrants.		
The transformed azimuth $\alpha_\mathrm{p,I}$ and $\alpha_\mathrm{v,I}$ in the first quadrant are		
$\alpha_\mathrm{p,I} = \alpha_\mathrm{p} - \frac{\pi}{2}$	$\alpha_\mathrm{p,I} = \alpha_\mathrm{p} - \pi$	$\alpha_\mathrm{p,I} = \alpha_\mathrm{p} - \frac{3}{2}\pi$
$\alpha_\mathrm{v,I} = \alpha_v - \frac{\pi}{2}$	$\alpha_\mathrm{v,I} = \alpha_v - \pi$	$\alpha_\mathrm{v,I} = \alpha_v - \frac{3}{2}\pi$
The transformed particle velocities are		
$v^b_{\mathrm{p},x,\mathrm{I}} = v^b_{\mathrm{p},y}$	$v^b_{\mathrm{p},x,\mathrm{I}} = -v^b_{\mathrm{p},x}$	$v^b_{\mathrm{p},x,\mathrm{I}} = -v^b_{\mathrm{p},y}$
$v^b_{\mathrm{p},y,\mathrm{I}} = -v^b_{\mathrm{p},x}$	$v^b_{\mathrm{p},y,\mathrm{I}} = -v^b_{\mathrm{p},y}$	$v^b_{\mathrm{p},y,\mathrm{I}} = v^b_{\mathrm{p},x}$
The case-by-case analysis following Table B.1 is applied.		
Analogous to the first transformation, the coordinates are transformed back.		
$v^a_{\mathrm{p},x,\mathrm{elastic}} = -v^a_{\mathrm{p},y,\mathrm{I}}$	$v^a_{\mathrm{p},x,\mathrm{elastic}} = -v^a_{\mathrm{p},x,\mathrm{I}}$	$v^a_{\mathrm{p},x,\mathrm{elastic}} = v^a_{\mathrm{p},y,\mathrm{I}}$
$v^a_{\mathrm{p},y,\mathrm{elastic}} = v^a_{\mathrm{p},x,\mathrm{I}}$	$v^a_{\mathrm{p},y,\mathrm{elastic}} = -v^a_{\mathrm{p},y,\mathrm{I}}$	$v^a_{\mathrm{p},y,\mathrm{elastic}} = -v^a_{\mathrm{p},x,\mathrm{I}}$

C Detailed Derivation of the Discretized Population Balance Equation System

Discretization of the Population Balance Equation

The semi-discrete form of the PBE was stated in Eq. (6.9) and it was derived from the continuous Eq. (6.1). A detailed derivation is given in the following. Integration of Eq. (6.1) over control volume $j \in 1 \dots N_j$ yields

$$\underbrace{\int_{z_{j-1/2}}^{z_{j+1/2}} \frac{\partial f}{\partial t} \,\mathrm{d}z}_{\mathrm{I}} + \underbrace{\int_{z_{j-1/2}}^{z_{j+1/2}} G(z) \frac{\partial f}{\partial h} \,\mathrm{d}z}_{\mathrm{II}} + \underbrace{\int_{z_{j-1/2}}^{z_{j+1/2}} v_\mathrm{p}(h) \frac{\partial f}{\partial z} \,\mathrm{d}z}_{\mathrm{III}} = 0 \tag{C.1}$$

For the accumulation term I, Leibniz's rule for differentiation under the integral sign is applied. Next, it is assumed that f is piecewise constant on $\left[z_{j-1/2}, z_{j+1/2}\right]$

$$\mathrm{I} = \frac{\mathrm{d}}{\mathrm{d}t} \int_{z_{j-1/2}}^{z_{j+1/2}} f \,\mathrm{d}z = \frac{\mathrm{d}f_j}{\mathrm{d}t} \Delta z \tag{C.2a}$$

For the convection in the internal coordinate in term II in Eq. (C.1), it is assumed that $G(z)$ is piecewise constant on $\left[z_{j-1/2}, z_{j+1/2}\right]$. Then, it is again assumed that f is piecewise constant on $\left[z_{j-1/2}, z_{j+1/2}\right]$

$$\mathrm{II} = G_j \int_{z_{j-1/2}}^{z_{j+1/2}} \frac{\partial f}{\partial h} \,\mathrm{d}z = G_j \frac{\partial f_j}{\partial h} \Delta z \tag{C.2b}$$

In the convection in the external coordinate in term III in Eq. (C.1), it is considered that $v_\mathrm{p}(h)$ depends only on the particle size. Then, for the convection term in z, the second fundamental theorem of calculus is applied

$$\mathrm{III} = v_\mathrm{p}(h) \int_{z_{j-1/2}}^{z_{j+1/2}} \frac{\partial f}{\partial z} \,\mathrm{d}z = v_\mathrm{p}(h) \left[f\right]_{z_{j-1/2}}^{z_{j+1/2}} = v_\mathrm{p}(h) \left(f_{j+1/2} - f_{j-1/2}\right) \tag{C.2c}$$

Summarizing Eqs. (C.1) and (C.2) leads to

$$\frac{\mathrm{d}f_j}{\mathrm{d}t} + G_j \frac{\partial f_j}{\partial h} + \frac{v_\mathrm{p}(h)}{\Delta z} \left(f_{j+1/2} - f_{j-1/2}\right) = 0 \tag{C.3}$$

The solution domain of $f(h, z, t)$ is discretized along the internal coordinate via the FVM. Equation (C.3) is integrated over one control volume $i \in 1 \dots N_i$.

$$\underbrace{\int_{h_{i-1/2}}^{h_{i+1/2}} \frac{\mathrm{d}f_j}{\mathrm{d}t} \,\mathrm{d}h}_{\mathrm{I}} + \underbrace{\int_{h_{i-1/2}}^{h_{i+1/2}} G_j \frac{\partial f_j}{\partial h} \,\mathrm{d}h}_{\mathrm{II}} + \underbrace{\int_{h_{i-1/2}}^{h_{i+1/2}} \frac{v_\mathrm{p}(h)}{\Delta z} \left(f_{j+1/2} - f_{j-1/2}\right) \,\mathrm{d}h}_{\mathrm{III}} = 0 \tag{C.4}$$

For the accumulation term I, Leibniz's rule for differentiation under the integral sign is applied. Then, it is assumed that f is piecewise constant on $\left[h_{i-1/2}, h_{i+1/2}\right]$

$$\mathrm{I} = \frac{\mathrm{d}}{\mathrm{d}t} \int_{h_{i-1/2}}^{h_{i+1/2}} f_j \, \mathrm{d}h = \frac{\mathrm{d}f_{i,j}}{\mathrm{d}t} \Delta h \tag{C.5a}$$

For the convection in the internal coordinate in term II in Eq. (C.4), it is considered that growth and dissolution are size-independent. Then, the second fundamental theorem of calculus is applied

$$\mathrm{II} = G_j \int_{h_{i-1/2}}^{h_{i+1/2}} \frac{\partial f_j}{\partial h} \, \mathrm{d}h = G_j \left[f_j\right]_{i-1/2}^{i+1/2} = G_j \left(f_{i+1/2,j} - f_{i-1/2,j}\right) \tag{C.5b}$$

For the convection in the external coordinate in term III in Eq. (C.4), it is assumed that $v_\mathrm{p}(h)$ is piecewise constant on $\left[h_{i-1/2}, h_{i+1/2}\right]$. Then, it is again assumed that f is piecewise constant on $\left[h_{i-1/2}, h_{i+1/2}\right]$

$$\mathrm{III} = \frac{v_{\mathrm{p},i}}{\Delta z} \int_{h_{i-1/2}}^{h_{i+1/2}} \left(f_{j+1/2} - f_{j-1/2}\right) \mathrm{d}h = \frac{v_{\mathrm{p},i}}{\Delta z} \left(f_{i,j+1/2} - f_{i,j-1/2}\right) \Delta h \tag{C.5c}$$

Insertion of Eqs. (C.5a), (C.5b), and (C.5c) into Eq. (C.4) leads to Eq. (6.9).

Discretization of the Continuous Phase Mass Balances

The continuous forms of the mass balances of dissolved anhydrate and water were given in Eqs. (6.5) and (6.6). The result after discretization was stated in Eqs. (6.10) and (6.11). A detailed derivation is given below for the anhydrate. Integration of Eq. (6.5) over control volume $j \in 1 \ldots N_j$ yields

$$\begin{aligned} \underbrace{\int_{z_{j-1/2}}^{z_{j+1/2}} \frac{\partial m_{\mathrm{f,anh}}}{\partial t} \, \mathrm{d}z}_{\mathrm{I}} = &- \underbrace{\int_{z_{j-1/2}}^{z_{j+1/2}} v_\mathrm{f} \frac{\partial m_{\mathrm{f,anh}}}{\partial z} \, \mathrm{d}z}_{\mathrm{II}} + \underbrace{\int_{z_{j-1/2}}^{z_{j+1/2}} D \frac{\partial^2 m_{\mathrm{f,anh}}}{\partial z^2} \, \mathrm{d}z}_{\mathrm{III}} \\ &- \underbrace{\int_{z_{j-1/2}}^{z_{j+1/2}} 3 \chi_\mathrm{anh} k_V \rho_\mathrm{p} \int_{h_\mathrm{min}}^{h_\mathrm{max}} G h^2 f \, \mathrm{d}h \, \mathrm{d}z}_{\mathrm{IV}} \end{aligned} \tag{C.6}$$

For the accumulation term I, Leibniz's rule for differentiation under the integral sign is applied. Next, it is assumed that $m_{\mathrm{f,anh}}$ is piecewise constant on $\left[z_{j-1/2}, z_{j+1/2}\right]$

$$\mathrm{I} = \frac{\mathrm{d}}{\mathrm{d}t} \int_{z_{j-1/2}}^{z_{j+1/2}} m_{\mathrm{f,anh}} \, \mathrm{d}z = \frac{\mathrm{d}m_{\mathrm{f,anh},j}}{\mathrm{d}t} \Delta z \tag{C.7}$$

For convection in term II in Eq. (C.6), it is considered that v_f is constant and the second fundamental theorem of calculus is applied

$$\mathrm{II} = v_\mathrm{f} \left[m_{\mathrm{f,anh}}\right]_{z_{j-1/2}}^{z_{j+1/2}} = v_\mathrm{f} \left(m_{\mathrm{f,anh},j+1/2} - m_{\mathrm{f,anh},j-1/2}\right) \tag{C.8}$$

For dispersion in term III in Eq. (C.6), it is considered that D is constant and the second fundamental theorem of calculus is applied.

$$\mathrm{III} = D\left[\frac{\partial m_{\mathrm{f,anh}}}{\partial z}\right]_{z_{j-1/2}}^{z_{j+1/2}} = D\left(\left.\frac{\partial m_{\mathrm{f,anh}}}{\partial z}\right|_{z_{j+1/2}} - \left.\frac{\partial m_{\mathrm{f,anh}}}{\partial z}\right|_{z_{j-1/2}}\right)$$

For $j = 1$, the equation becomes

$$\mathrm{III} = D\left(\left.\frac{\partial m_{\mathrm{f,anh}}}{\partial z}\right|_{z_{3/2}} - \left.\frac{\partial m_{\mathrm{f,anh}}}{\partial z}\right|_{z_{1/2}}\right)$$

It could be assumed that there was no dispersion over the inlet. Whereas here, it is assumed that $m_{\mathrm{f,anh}}$ is piecewise linear on $\left[z_{1/2}, z_1\right]$ and on $[z_1, z_2]$. With the boundary condition from Eq. (6.7a) it results that

$$\begin{aligned}\mathrm{III} &= D\left(\frac{m_{\mathrm{f,anh},2} - m_{\mathrm{f,anh},1}}{\Delta z} - \frac{m_{\mathrm{f,anh},1} - m_{\mathrm{f,anh,in}}}{\Delta z/2}\right)\\ &= D\frac{m_{\mathrm{f,anh},2} - 3m_{\mathrm{f,anh},1} + 2m_{\mathrm{f,anh,in}}}{\Delta z}\end{aligned} \tag{C.9a}$$

approximating the profile again piecewise linearly on $[z_j, z_{j+1}]$, for $j \in 2 \ldots N_{j-1}$

$$\begin{aligned}\mathrm{III} &= D\frac{m_{\mathrm{f,anh},j+1} - m_{\mathrm{f,anh},j}}{\Delta z} - D\frac{m_{\mathrm{f,anh},j} - m_{\mathrm{f,anh},j-1}}{\Delta z}\\ &= D\frac{m_{\mathrm{f,anh},j+1} - 2m_{\mathrm{f,anh},j} + m_{\mathrm{f,anh},j-1}}{\Delta z}\end{aligned} \tag{C.9b}$$

and for $j = N_j$

$$\mathrm{III} = D\left(\left.\frac{\partial m_{\mathrm{f,anh}}}{\partial z}\right|_{z_{N_j+1/2}} - \left.\frac{\partial m_{\mathrm{f,anh}}}{\partial z}\right|_{z_{N_j-1/2}}\right)$$

and assuming that there is no dispersion over the outlet

$$\mathrm{III} = -D\left.\frac{\partial m_{\mathrm{f,anh}}}{\partial z}\right|_{z_{N_j-1/2}}$$

and assuming again that $m_{\mathrm{f,anh}}$ is piecewise linear on $\left[z_{N_j-1}, z_{N_j}\right]$

$$\mathrm{III} = -D\frac{m_{\mathrm{f,anh},N_j} - m_{\mathrm{f,anh},N_j-1}}{\Delta z} \tag{C.9c}$$

Assuming again that f and G are piecewise constant on $\left[z_{j-1/2}, z_{j+1/2}\right]$, the source and sink term IV in Eq. (C.6) becomes

$$\begin{aligned}\mathrm{IV} &= 3\chi_{\mathrm{anh}}k_V\rho_{\mathrm{p}}\int_{h_{\min}}^{h_{\max}} G_j h^2 f_j \,\mathrm{d}h \int_{z_{j-1/2}}^{z_{j+1/2}} \mathrm{d}z\\ &= 3\chi_{\mathrm{anh}}k_V\rho_{\mathrm{p}}G_j\Delta z\int_{h_{\min}}^{h_{\max}} h^2 f_j \,\mathrm{d}h\end{aligned}$$

Assuming a piecewise constant f on $\left[h_{i-1/2}, h_{i+1/2}\right]$

$$\mathrm{IV} = 3\chi_{\mathrm{anh}} k_V \rho_{\mathrm{p}} G_j \Delta z \sum_{i=1}^{N_i} h_i^2 f_{i,j} \Delta h \tag{C.10}$$

Inserting Eqs. (C.7), (C.8), (C.9), and (C.10) into Eq. (C.6) and applying again the boundary condition from Eq. (6.7a) yields for $j = 1$

$$\begin{aligned}\frac{\mathrm{d}m_{\mathrm{f,anh},1}}{\mathrm{d}t}\Delta z =& - v_{\mathrm{f}} \left(m_{\mathrm{f,anh},3/2} - m_{\mathrm{f,anh,in}}\right) + D\frac{m_{\mathrm{f,anh},2} - 3m_{\mathrm{f,anh},1} + 2m_{\mathrm{f,anh,in}}}{\Delta z} \\ & - 3\chi_{\mathrm{anh}} k_V \rho_{\mathrm{p}} G_1 \Delta z \sum_{i=1}^{N_i} h_i^2 f_{i,1} \Delta h\end{aligned}$$

for $j \in 2 \ldots N_{j-1}$

$$\begin{aligned}\frac{\mathrm{d}m_{\mathrm{f,anh},j}}{\mathrm{d}t}\Delta z =& - v_{\mathrm{f}} \left(m_{\mathrm{f,anh},j+1/2} - m_{\mathrm{f,anh},j-1/2}\right) + D\frac{m_{\mathrm{f,anh},j+1} - 2m_{\mathrm{f,anh},j} + m_{\mathrm{f,anh},j-1}}{\Delta z} \\ & - 3\chi_{\mathrm{anh}} k_V \rho_{\mathrm{p}} G_j \Delta z \sum_{i=1}^{N_i} h_i^2 f_{i,j} \Delta h\end{aligned}$$

for $j = N_j$

$$\begin{aligned}\frac{\mathrm{d}m_{\mathrm{f,anh},N_j}}{\mathrm{d}t}\Delta z =& - v_{\mathrm{f}} \left(m_{\mathrm{f,anh},N_j+1/2} - m_{\mathrm{f,anh},N_j-1/2}\right) + D\frac{m_{\mathrm{f,anh},N_j-1} - m_{\mathrm{f,anh},N_j}}{\Delta z} \\ & - 3\chi_{\mathrm{anh}} k_V \rho_{\mathrm{p}} G_{N_j} \Delta z \sum_{i=1}^{N_i} h_i^2 f_{i,N_j} \Delta h\end{aligned}$$

Division by Δz leads to Eq. (6.10). The derivation for water in the continuous phase was carried out analogously to the one for anhydrate.

Bibliography

Adler, M. (1934). Strömung in gekrümmten Rohren. *ZAMM - Journal of Applied Mathematics and Mechanics / Zeitschrift für Angewandte Mathematik und Mechanik*, 14(5):257–275.

Baptista, P., Oliveira, F., Sannervik, J., and Oliveira, J. (1996a). The effect of mixing particles with different characteristics on the residence time distribution of particles in two-phase flow in a tubular system. *Journal of Food Engineering*, 29(3):361–373.

Baptista, P. N., Oliveira, F. A. R., Caldas, S. M., Oliveira, J. C., and Sastry, S. K. (1996b). Effect of product and process variables in the flow of spherical particles in a carrier fluid through straight tubes. *Journal of Food Processing and Preservation*, 20(6):467–486.

Barrett, P. and Glennon, B. (2002). Characterizing the metastable zone width and solubility curve using Lasentec FBRM and PVM. *Chemical Engineering Research and Design*, 80(7):799–805.

Besenhard, M., Thurnberger, A., Hohl, R., Faulhammer, E., Rattenberger, J., and Khinast, J. (2014a). Continuous API-crystal coating via coacervation in a tubular reactor. *International Journal of Pharmaceutics*, 475(1-2):198–207.

Besenhard, M. O., Hohl, R., Hodzic, A., Eder, R. J. P., and Khinast, J. G. (2014b). Modeling a seeded continuous crystallizer for the production of active pharmaceutical ingredients. *Crystal Research and Technology*, 49(2-3):92–108.

Besenhard, M. O., Neugebauer, P., Ho, C.-D., and Khinast, J. G. (2015). Crystal size control in a continuous tubular crystallizer. *Crystal Growth & Design*, 15(4):1683–1691.

Besenhard, M. O., Neugebauer, P., Scheibelhofer, O., and Khinast, J. G. (2017). Crystal engineering in continuous plug-flow crystallizers. *Crystal Growth & Design*, 17(12):6432–6444.

Bittorf, L., Reichmann, F., Schmalenberg, M., Soboll, S., and Kockmann, N. (2019). Equipment and separation units for flow chemistry applications and process development. *Chemical Engineering & Technology*, 42(10):1985–1995.

Borchert, C. and Sundmacher, K. (2011). Crystal aggregation in a flow tube: Image-based observation. *Chemical Engineering & Technology*, 34(4):545–556.

Borchert, C., Temmel, E., Eisenschmidt, H., Lorenz, H., Seidel-Morgenstern, A., and Sundmacher, K. (2014). Image-based in situ identification of face specific crystal growth rates from crystal populations. *Crystal Growth & Design*, 14(3):952–971.

Brenner, H. (1961). The slow motion of a sphere through a viscous fluid towards a plane surface. *Chemical Engineering Science*, 16(3):242–251.

Buckley, D. H. (1981). *Surface effects in adhesion, friction, wear, and lubrication*. Tribology series. Elsevier Science, Amsterdam, 5th edition.

Buckley, H. E. (1930). The crystallization of potash-alum and the effect of certain added impurities on its habit. *Zeitschrift für Kristallographie - Crystalline Materials*, 73:443–464.

Castelain, C. and Legentilhomme, P. (2006). Residence time distribution of a purely viscous non-Newtonian fluid in helically coiled or spatially chaotic flows. *Chemical Engineering Journal*, 120(3):181–191.

Chakrabandhu, K. and Singh, R. K. (2006). Determination of food particle residence time distributions in coiled tube and straight tube with bends at high temperature using correlation analysis. *Journal of Food Engineering*, 76(2):238–249.

Chen, Y., Sabio, J. C., and Hartman, R. L. (2015). When solids stop flow chemistry in commercial tubing. *Journal of Flow Chemistry*, 5(3):166–171.

Cheng, L., Kuznetsov, A. V., and Sandeep, K. P. (2005). Mathematical modelling of two-phase non-Newtonian flow in a helical pipe. *International Journal for Numerical Methods in Fluids*, 48(6):649–670.

Crowe, C. T. (2006). *Multiphase Flow Handbook*. Mechanical engineering series. CRC Press, Boca Raton.

Crowe, C. T., Schwarzkopf, J. D., Sommerfeld, M., and Tsuji, Y. (2012). *Multiphase flows with droplets and particles*. CRC Press, Boca Raton, 2nd edition.

de Albuquerque, I., Mazzotti, M., Ochsenbein, D. R., and Morari, M. (2016). Effect of needle-like crystal shape on measured particle size distributions. *AIChE Journal*, 62(9):2974–2985.

Dean, W. (1927). XVI. Note on the motion of fluid in a curved pipe. *Philosophical Magazine*, 4(20):208–223.

Eder, R. J. P., Radl, S., Schmitt, E., Innerhofer, S., Maier, M., Gruber-Woelfler, H., and Khinast, J. G. (2010). Continuously seeded, continuously operated tubular crystallizer for the production of active pharmaceutical ingredients. *Crystal Growth & Design*, 10(5):2247–2257.

Eder, R. J. P., Schmitt, E. K., Grill, J., Radl, S., Gruber-Woelfler, H., and Khinast, J. G. (2011). Seed loading effects on the mean crystal size of acetylsalicylic acid in a continuous-flow crystallization device. *Crystal Research and Technology*, 46(3):227–237.

Eder, R. J. P., Schrank, S., Besenhard, M. O., Roblegg, E., Gruber-Woelfler, H., and Khinast, J. G. (2012). Continuous sonocrystallization of acetylsalicylic acid (ASA): Control of crystal size. *Crystal Growth & Design*, 12(10):4733–4738.

Eisenschmidt, H. (2018). *A cyclic growth-dissolution process for the controlled manipulation of crystal shape distributions*. Dissertation, Otto-von-Guericke University Magdeburg, Germany.

Eisenschmidt, H., Bajcinca, N., and Sundmacher, K. (2016). Optimal control of crystal shapes in batch crystallization experiments by growth-dissolution cycles. *Crystal Growth & Design*, 16(6):3297–3306.

Eisenschmidt, H., Voigt, A., and Sundmacher, K. (2015). Face-specific growth and dissolution kinetics of potassium dihydrogen phosphate crystals from batch crystallization experiments. *Crystal Growth & Design*, 15(1):219–227.

Farias, L. F., de Souza, J. A., Braatz, R. D., and da Rosa, C. A. (2019). Coupling of the population balance equation into a two-phase model for the simulation of combined cooling and antisolvent crystallization using OpenFOAM. *Computers & Chemical Engineering*, 123:246–256.

Ferguson, S., Morris, G., Hao, H., Barrett, M., and Glennon, B. (2013). Characterization of the anti-solvent batch, plug flow and MSMPR crystallization of benzoic acid. *Chemical Engineering Science*, 104:44–54.

Ferreira, T. and Rasband, W. (2012). *ImageJ User GuideIJ 1.46r*.

Figueiredo, A. and Raimundo, A. (1996). Analysis of the performances of heat exchangers used in hot-water stores. *Applied Thermal Engineering*, 16(7):605–611.

Furuta, M., Mukai, K., Cork, D., and Mae, K. (2016). Continuous crystallization using a sonicated tubular system for controlling particle size in an API manufacturing process. *Chemical Engineering and Processing: Process Intensification*, 102:210–218.

Gao, Y., Magaud, P., Lafforgue, C., Colin, S., and Baldas, L. (2019). Inertial lateral migration and self-assembly of particles in bidisperse suspensions in microchannel flows. *Microfluidics and Nanofluidics*, 23(7):93.

Garside, J., Mersmann, A., and Nỳvlt, J. (2002). *Measurement of crystal growth and nucleation rates*. Institution of Chemical Engineers, Rugby, 2nd edition.

Girolami, M. W. and Rousseau, R. W. (1985). Size-dependent crystal growth—A manifestation of growth rate dispersion in the potassium alum-water system. *AIChE Journal*, 31(11):1821–1828.

Glück, B. (1988). *Hydrodynamische und gasdynamische Rohrströmung, Druckverluste*. Bausteine der Heizungstechnik. VEB Verlag für Bauwesen, Berlin.

Gnielinski, V. (2013). *G3 Durchströmte Rohrwendeln*. VDI-Wärmeatlas. Springer Vieweg, Berlin, Heidelberg.

Goldman, A. J., Cox, R. G., and Brenner, H. (1967). Slow viscous motion of a sphere parallel to a plane wall–I Motion through a quiescent fluid. *Chemical Engineering Science*, 22(4):637–651.

Griffiths, G. (2016). *Numerical Analysis Using R: Solutions to ODEs and PDEs*. Cambridge University Press, New York, NY.

Groll, R. (2015). *Diffusionsmodellierung. Skalenübergreifende Thermofluiddynamik des Wärme- und Stofftransports disperser Systeme*. Springer Fachmedien Wiesbaden, 1st edition.

Gurel, S., Ward, S. G., and Whitmore, R. L. (1955). Studies of the viscosity and sedimentation of suspensions: Part 3. – The sedimentation of isometric and compact particles. *British Journal of Applied Physics*, 6(3):83–87.

Haider, A. and Levenspiel, O. (1989). Drag coefficient and terminal velocity of spherical and nonspherical particles. *Powder Technology*, 58(1):63–70.

Happel, J. and Brenner, H. (1983). *Low Reynolds number hydrodynamics : with special applications to particulate media*. Mechanics of fluids and transport processes. Nijhoff, The Hague, 1st paperback edition.

Hartel, R. W. (2002). 13 - Crystallization in foods. In Myerson, A. S., editor, *Handbook of Industrial Crystallization*, pages 287–304. Butterworth-Heinemann, Woburn, 2nd edition.

Hölzer, A. and Sommerfeld, M. (2008). New simple correlation formula for the drag coefficient of non-spherical particles. *Powder Technology*, 184(3):361–365.

Hofmann, G. and Melches, C. (2013). *Continuous Crystallization*, pages 203–233. Wiley-VCH, Weinheim.

Hohmann, L., Gorny, R., Klaas, O., Ahlert, J., Wohlgemuth, K., and Kockmann, N. (2016a). Design of a continuous tubular cooling crystallizer for process development on lab-scale. *Chemical Engineering & Technology*, 39(7):1268–1280.

Hohmann, L., Greinert, T., Mierka, O., Turek, S., Schembecker, G., Bayraktar, E., Wohlgemuth, K., and Kockmann, N. (2018). Analysis of crystal size dispersion effects in a continuous coiled tubular crystallizer: Experiments and modeling. *Crystal Growth & Design*, 18(3):1459–1473.

Hohmann, L., Kurt, S. K., Soboll, S., and Kockmann, N. (2016b). Separation units and equipment for lab-scale process development. *Journal of Flow Chemistry*, 6(3):181–190.

Hohmann, L., Schmalenberg, M., Prasanna, M., Matuschek, M., and Kockmann, N. (2019). Suspension flow behavior and particle residence time distribution in helical tube devices. *Chemical Engineering Journal*, 360:1371–1389.

Howell, J. P. B., Mott, D. R., Golden, J. P., and Ligler, F. S. (2004). Design and evaluation of a Dean vortex-based micromixer. *Lab on a Chip*, 4(6):663–669.

Hulburt, H. and Katz, S. (1964). Some problems in particle technology: A statistical mechanical formulation. *Chemical Engineering Science*, 19(8):555–574.

Hyde, F. W., Alberg, M., and Smith, K. (1997). Comparison of fluorinated polymers against stainless steel, glass and polypropylene in microbial biofilm adherence and removal. *Journal of Industrial Microbiology and Biotechnology*, 19(2):142–149.

Jokiel, M. and Sundmacher, K. (2019). *Spezielle labortechnische Reaktoren: Wendelrohrreaktor*, pages 1–33. Springer Spektrum, Berlin, Heidelberg.

Kast, W., Gnielinski, V., and Nirschl, H. (2013). *L1.2 Druckverlust in durchströmten Rohren*. VDI-Wärmeatlas. Springer Vieweg, Berlin, Heidelberg.

Kazi, S., Duffy, G., and Chen, X. (2012). Fouling and fouling mitigation on heated metal surfaces. *Desalination*, 288:126–134.

Khinast, J. and Rantanen, J. (2017). *Continuous Manufacturing of Pharmaceuticals*. John Wiley & Sons, Ltd, Chichester, UK.

Kleinstreuer, C. (2017). *Two-Phase Flow: Theory and Applications*. CRC Press, New York.

Klutz, S., Kurt, S. K., Lobedann, M., and Kockmann, N. (2015). Narrow residence time distribution in tubular reactor concept for Reynolds number range of 10–100. *Chemical Engineering Research and Design*, 95:22–33.

Koren, B. (1993). *A robust upwind discretization method for advection, diffusion and source terms*, volume 45 of *Notes on Numerical Fluid Mechanics*, pages 117–138. Vieweg, Braunschweig/Wiesbaden, Germany.

Koutsky, J. A. and Adler, R. J. (1964). Minimisation of axial dispersion by use of secondary flow in helical tubes. *The Canadian Journal of Chemical Engineering*, 42(6):239–246.

Kovačević, T., Wiedmeyer, V., Schock, J., Voigt, A., Pfeiffer, F., Sundmacher, K., and Briesen, H. (2017). Disorientation angle distribution of primary particles in potash alum aggregates. *Journal of Crystal Growth*, 467:93–106.

Kubair, V. and Varrier, C. B. S. (1961). Pressure drop for liquid flow in helical coils. *Transactions, Indian Institute of Chemical Engineers*, 14:93–97.

Kubota, N., Shimizu, K., and Itagaki, H. (1985). Densities and viscosities of supersaturated potash alum aqueous solutions. *Journal of Crystal Growth*, 73:359–363.

Kumar, V. and Nigam, K. (2005). Numerical simulation of steady flow fields in coiled flow inverter. *International Journal of Heat and Mass Transfer*, 48:4811–4828.

Kurt, S. K., Gelhausen, M. G., and Kockmann, N. (2015). Axial dispersion and heat transfer in a milli/microstructured coiled flow inverter for narrow residence time distribution at laminar flow. *Chemical Engineering & Technology*, 38(7):1122–1130.

Legrand, A., Berthou, M., and Fillaudeau, L. (2007). Characterization of solid–liquid suspensions (real, large non-spherical particles in non-Newtonian carrier fluid) flowing in horizontal and vertical pipes. *Journal of Food Engineering*, 78(1):345–355.

Lewis, A. E., Seckler, M. M., Kramer, H. J., and Rosmalen, G. v. (2015). *Industrial crystallization: fundamentals and applications*. Cambridge Univ. Press, Cambridge.

Lide, D., editor (2004). *Coefficient of friction*. CRC Handbook of Chemistry and Physics. CRC Press, Boca Raton, 85th edition.

Llano-Restrepo, M. (2005). Modeling and simulation of vertical continuous cooling crystallizers for the sugar industry. *Industrial & Engineering Chemistry Research*, 44(24):9244–9263.

Ma, C. Y., Wan, J., and Wang, X. Z. (2012). Faceted growth rate estimation of potash alum crystals grown from solution in a hot-stage reactor. *Powder Technology*, 227:96–103.

Ma, C. Y., Wang, X. Z., and Roberts, K. J. (2008). Morphological population balance for modeling crystal growth in face directions. *AIChE Journal*, 54(1):209–222.

Mader-Arndt, K., Aman, S., Fuchs, R., and Tomas, J. (2017). Contact properties determination of macroscopic fine disperse glass particles via compression tests in normal direction. *Advanced Powder Technology*, 28(1):101–114.

Matas, J.-P., Morris, J. F., and Guazzelli, l. (2004). Inertial migration of rigid spherical particles in Poiseuille flow. *Journal of Fluid Mechanics*, 515:171–195.

Maxey, M. R. and Riley, J. J. (1983). Equation of motion for a small rigid sphere in a nonuniform flow. *The Physics of Fluids*, 26(4):883–889.

Mei, R. (1992). An approximate expression for the shear lift force on a spherical particle at finite Reynolds number. *International Journal of Multiphase Flow*, 18(1):145–147.

Michaelides, E. E. (2006). *Particles, bubbles & drops : their motion, heat and mass transfer*. World Scientific, New Jersey.

Michaelides, E. E., Crowe, C. T., and Schwarzkopf, J. D., editors (2017). *Multiphase flow handbook*. Mechanical and aerospace engineering. CRC Press, Taylor & Francis Group, Boca Raton, 2nd edition.

Mishra, P. and Gupta, S. N. (1979). Momentum transfer in curved pipes. 1. Newtonian fluids. *Industrial & Engineering Chemistry Process Design and Development*, 18(1):130–137.

Mridha, M. and Nigam, K. (2008). Coiled flow inverter as an inline mixer. *Chemical Engineering Science*, 63:1724–1732.

Mullin, J. W. (2001). *Crystallization*. Butterworth-Heinemann, Oxford, 4th edition.

Mullin, J. W., Garside, J., and Unahabhokha, R. (1965). Diffusivities of ammonium and potassium alums in aqueous solutions. *Journal of Applied Chemistry*, 15(11):502–505.

Mullin, J. W. and Sipek, M. (1981). Solubility and density isotherms for potassium aluminum sulfate-water-alcohol systems. *Journal of Chemical & Engineering Data*, 26(2):164–165.

Muschelknautz, U. (2013). *L3.3 Druckverlust in pneumatischen Transportanlagen*. VDI-Wärmeatlas. Springer Vieweg, Berlin, Heidelberg.

Myerson, A. S. (2002). *Handbook of industrial crystallization*. Butterworth-Heinemann, Boston, 2nd edition.

Neugebauer, P., Cardona, J., Besenhard, M. O., Peter, A., Gruber-Woelfler, H., Tachtatzis, C., Cleary, A., Andonovic, I., Sefcik, J., and Khinast, J. G. (2018). Crystal shape modification via cycles of growth and dissolution in a tubular crystallizer. *Crystal Growth & Design*, 18(8):4403–4415.

Neugebauer, P. and Khinast, J. G. (2015). Continuous crystallization of proteins in a tubular plug-flow crystallizer. *Crystal Growth & Design*, 15(3):1089–1095.

Oesterlé, B. and Dinh, T. B. (1998). Experiments on the lift of a spinning sphere in a range of intermediate Reynolds numbers. *Experiments in Fluids*, 25(1):16–22.

Palazoglu, T. K. and Sandeep, K. P. (2001). Computational fluid dynamics modeling of fluid flow in helical tubes. *Journal of Food Process Engineering*, 25:141–158.

Palazoglu, T. K. and Sandeep, K. P. (2004). Effect of tube curvature ratio on the residence time distribution of multiple particles in helical tubes. *LWT - Food Science and Technology*, 37(4):387–393.

Patankar, S. V. (1980). *Numerical heat transfer and fluid flow*. Series in computational methods in mechanics and thermal sciences. Hemisphere Publ. Co., New York.

Prohm, C., Gierlak, M., and Stark, H. (2012). Inertial microfluidics with multi-particle collision dynamics. *The European Physical Journal E*, 35(8):80.

Qamar, S. (2008). *Modeling and simulation of population balances for particulate processes*. Habilitationsschrift, Otto-von-Guericke University Magdeburg, Germany.

Qamar, S., Elsner, M., Angelov, I., Warnecke, G., and Seidel-Morgenstern, A. (2006). A comparative study of high resolution schemes for solving population balances in crystallization. *Computers & Chemical Engineering*, 30(6):1119–1131.

Qamar, S., Galan, K., Peter Elsner, M., Hussain, I., and Seidel-Morgenstern, A. (2013). Theoretical investigation of simultaneous continuous preferential crystallization in a coupled mode. *Chemical Engineering Science*, 98:25–39.

Ramkrishna, D. (2000). *Population Balances: Theory and Applications to Particulate Systems in Engineering*. Academic Press, San Diego.

Redlinger-Pohn, J., König, L. M., Kloss, C., Goniva, C., and Radl, S. (2016a). Modeling of non-spherical, elongated particles for industrial suspension flow simulation. In Papadrakakis, M., Papadopoulos, V., Stefanou, G., and Plevris, V., editors, *Proceedings of ECCOMAS Congress 2016*, pages 586–599, Crete Island, Greece.

Redlinger-Pohn, J. D., Jagiello, L. A., Bauer, W., and Radl, S. (2016b). Mechanistic understanding of size-based fiber separation in coiled tubes. *International Journal of Multiphase Flow*, 83:239–253.

Rimez, B., Septavaux, J., and Scheid, B. (2019). The coupling of in-flow reaction with continuous flow seedless tubular crystallization. *Reaction Chemistry & Engineering*, 4(3):516–522.

Roberts, A. and Richardson, J. (1981). Interface study of rubber-ice friction. *Wear*, 67(1):55–69.

Rubinow, S. I. and Keller, J. B. (1961). The transverse force on a spinning sphere moving in a viscous fluid. *Journal of Fluid Mechanics*, 11(3):447–459.

Rusconi, R., Guasto, J. S., and Stocker, R. (2014). Bacterial transport suppressed by fluid shear. *Nature Physics*, 10:212–217.

Sandeep, K., Zuritz, C., and Puri, V. (1997). Residence time distribution of particles during two-phase non-Newtonian flow in conventional as compared with helical holding tubes. *Journal of Food Science*, 62(4):647–652.

Sandeep, K., Zuritz, C. A., and Puri, V. M. (2000). Modelling non-Newtonian two-phase flow in conventional and helical-holding tubes. *International Journal of Food Science and Technology*, 35:511–522.

Saxena, A. K. and Nigam, K. (1983). Effect of coil pitch and cross-sectional ellipticity on RTD for diffusion-free laminar flow in coiled tubes. *Chemical Engineering Communications*, 23(4-6):277–289.

Saxena, A. K. and Nigam, K. D. P. (1984). Coiled configuration for flow inversion and its effect on residence time distribution. *AIChE Journal*, 30(3):363–368.

Schaaf, C., Rühle, F., and Stark, H. (2019). A flowing pair of particles in inertial microfluidics. *Soft Matter*, 15:1988–1998.

Schäffer, E., Nørrelykke, S. F., and Howard, J. (2007). Surface forces and drag coefficients of microspheres near a plane surface measured with optical tweezers. *Langmuir*, 23(7):3654–3665.

Schiller, L. and Naumann, A. (1933). Über die grundlegenden Berechnungen bei der Schwerkraftaufbereitung. *Zeitschrift des Vereines Deutscher Ingenieure*, 77(12):318–320.

Schmidt, E. F. (1967). Wärmeübergang und Druckverlust in Rohrschlangen. *Chemie Ingenieur Technik*, 39(13):781–789.

Schorsch, S., Ochsenbein, D. R., Vetter, T., Morari, M., and Mazzotti, M. (2014). High accuracy online measurement of multidimensional particle size distributions during crystallization. *Chemical Engineering Science*, 105:155–168.

Schorsch, S., Vetter, T., and Mazzotti, M. (2012). Measuring multidimensional particle size distributions during crystallization. *Chemical Engineering Science*, 77:130–142. 18th International Symposium on Industrial Crystallization.

Segré, G. and Silberberg, A. (1961). Radial particle displacements in Poiseuille flow of suspensions. *Nature*, 189:209–210.

Singh, J., Verma, V., and Nigam, K. D. P. (2013). Flow characteristics of power-law fluids in coiled flow inverter. *Industrial & Engineering Chemistry Research*, 52(1):207–221.

Sommerfeld, M. (2013). *L3.1 Bewegung fester Partikel in Gasen und Flüssigkeiten*. VDI-Wärmeatlas. Springer Vieweg, Berlin, Heidelberg.

Sommerfeld, M. and Kussin, J. (2003). Analysis of collision effects for turbulent gas-particle flow in a horizontal channel. Part II. Integral properties and validation. *International Journal of Multiphase Flow*, 29(4):701–718.

Sparks, T. and Chase, G. (2016). Section 1 - Filtration – Introduction, physical principles and ratings. In *Filters and Filtration Handbook*, pages 1–54. Butterworth-Heinemann, Oxford, 6th edition.

Sweby, P. (1984). High resolution schemes using flux limiters for hyperbolic conservation laws. *SIAM Journal on Numerical Analysis*, 21(5):995–1011.

Tanneberger, U., Lacmann, R., Herden, A., Klapper, H., Schmiemann, D., Becker, R. A., Mersmann, A., and Zacher, U. (1996). The dispersion of growth rate as a result of different crystal perfection. *Journal of Crystal Growth*, 166(1):1074–1077.

Tavare, N. S. (1995). *Industrial crystallization: process simulation analysis and design*. The Plenum chemical engineering series. Plenum Press, New York, NY.

Temmel, E., Eicke, M., Lorenz, H., and Seidel-Morgenstern, A. (2016). A short-cut method for the quantification of crystallization kinetics. 2. Experimental application. *Crystal Growth & Design*, 16(12):6756–6768.

ter Horst, J. H., Schmidt, C., and Ulrich, J. (2015). 32 - Fundamentals of industrial crystallization. In Rudolph, P., editor, *Handbook of Crystal Growth*, pages 1317–1349. Elsevier, Boston, 2nd edition.

Tiwari, P., Antal, S. P., and Podowski, M. Z. (2006). Three-dimensional fluid mechanics of particulate two-phase flows in U-bend and helical conduits. *Physics of Fluids*, 18(4):043304.

Tsai, C.-J. and Pui, D. Y. H. (1990). Numerical study of particle deposition in bends of a circular cross-section-laminar flow regime. *Aerosol Science and Technology*, 12(4):813–831.

U.S. Food and Drug Administration (2004). Guidance for industry, PAT - A framework for innovative pharmaceutical development, manufacturing and quality assurance.

Variankaval, N., Cote, A. S., and Doherty, M. F. (2008). From form to function: Crystallization of active pharmaceutical ingredients. *AIChE Journal*, 54(7):1682–1688.

Vashisth, S., Kumar, V., and Nigam, K. D. P. (2008). A review on the potential applications of curved geometries in process industry. *Industrial & Engineering Chemistry Research*, 47(10):3291–3337.

Vashisth, S. and Nigam, K. (2009). Prediction of flow profiles and interfacial phenomena for two-phase flow in coiled tubes. *Chemical Engineering and Processing: Process Intensification*, 48(1):452–463.

Wang, S., Mersmann, A., and Kind, M. (1990). Verification of the constant crystal growth model for attrition particles and its relevance to the modeling of crystallizers. *Journal of Crystal Growth*, 99(1):1104–1107.

Wieckhusen, D. (2013). *Development of Batch Crystallization*, pages 187–202. Wiley-VCH, Weinheim.

Wiedmeyer, V., Anker, F., Bartsch, C., Voigt, A., John, V., and Sundmacher, K. (2017a). Continuous crystallization in a helically coiled flow tube: Analysis of flow field, residence time behavior, and crystal growth. *Industrial & Engineering Chemistry Research*, 56(13):3699–3712.

Wiedmeyer, V., Voigt, A., and Sundmacher, K. (2017b). Crystal population growth in a continuous helically coiled flow tube crystallizer. *Chemical Engineering & Technology*, 40(9):1584–1590.

Winn, D. and Doherty, M. F. (2000). Modeling crystal shapes of organic materials grown from solution. *AIChE Journal*, 46(7):1348–1367.

Yang, H. G., Sun, C. H., Qiao, S. Z., Zou, J., Liu, G., Smith, S. C., Cheng, H. M., and Lu, G. Q. (2008). Anatase TiO2 single crystals with a large percentage of reactive facets. *Nature*, 453:638–641.

Zeidler, E. (2013). *Springer-Handbuch der Mathematik I*. Springer Fachmedien, Wiesbaden.

Zhu, H. P., Zhou, Z. Y., Yang, R. Y., and Yu, A. B. (2007). Discrete particle simulation of particulate systems: Theoretical developments. *Chemical Engineering Science*, 62(13):3378–3396.

List of Figures

List of Tables

Publications

Journal Publications

Bartsch, C., Wiedmeyer, V., Lakdawala, Z., Patterson, R. I., Voigt, A., Sundmacher, K., and John, V. (2019). Stochastic-deterministic population balance modeling and simulation of a fluidized bed crystallizer experiment. *Chemical Engineering Science*, 208:115102.

Kovačević, T., Wiedmeyer, V., Schock, J., Voigt, A., Pfeiffer, F., Sundmacher, K., and Briesen, H. (2017). Disorientation angle distribution of primary particles in potash alum aggregates. *Journal of Crystal Growth*, 467:93–106.

Wiedmeyer, V., Anker, F., Bartsch, C., Voigt, A., John, V., and Sundmacher, K. (2017). Continuous crystallization in a helically coiled flow tube: Analysis of flow field, residence time behavior, and crystal growth. *Industrial & Engineering Chemistry Research*, 56(13):3699–3712.

Wiedmeyer, V., Voigt, A., and Sundmacher, K. (2017). Crystal population growth in a continuous helically coiled flow tube crystallizer. *Chemical Engineering & Technology*, 40(9):1584–1590.

Conference Proceedings

Voigt, A., Wiedmeyer, V., and Sundmacher, K. Agglomeration in a fluidized bed crystallizer - from experiments to modeling. *Conference Proceedings of AIChE Annual Meeting 2016*.

Wiedmeyer, V., Voigt, A., Anker, F., John, V., Ahrens, R., Le Borne, S., and Sundmacher, K. (2018) Kontinuierliche formselektive Kristallisation: Neue Strategien. *ProcessNet-Jahrestagung und 33. DECHEMA-Jahrestagung der Biotechnologen 2018*, *Chemie Ingenieur Technik*, 90(9):1198.

Conference Talks and Posters

Ahrens, R., Anker, F., Bartsch, C., Voigt, A., Wiedmeyer, V., Sundmacher, K., John, V., and Le Borne, S., Advanced numerical methods for the simulation of population balance systems. In *PBM 2018*, May 7-9, 2018. (Poster Presentation).

Eisenschmidt, H., Wiedmeyer, V., Borchert, C., Bajcinca, N., and Sundmacher, K. Shape-Selective Crystallization: Modeling, Observation, Control. In *TU Graz, Institut für Prozess- und Partikeltechnik*, April 24, 2014. (Invited Oral Presentation).

Kovačević, T., Wiedmeyer, V., Schock, J., Pfeiffer, F., Voigt, A., Sundmacher, K. and Briesen, H. Orientation of primary particles in potash alum aggregates. In *BIWIC 2016*

(23rd International Workshop on Industrial Crystallization), Sept 6-8, 2016. (Poster Presentation).

König, L., Wiedmeyer, V.,Voigt, A., Sundmacher, K. Crystallization in standard batch crystallizers and advanced helically coiled flow tubes: Numerical limits of current simulation methods. In *YCOPE 2019 (Young Professionals Conference on Process Engineering)*, March 18-20, 2019. (Poster Presentation).

Voigt, A., Wiedmeyer, V., and Sundmacher, K. Agglomeration-Driven Product Selection in a Continously Operated Fluidized-Bed Crystallizer. In *2018 AIChE Annual Meeting*, Oct 28-Nov 2, 2018. (Oral Presentation).

Wiedmeyer, V., Anker, F., Voigt, A., John, V., and Sundmacher, K. Crystal shape evolution in a continuous helically coiled flow tube crystallizer. In *ECCE10 (10th European Congress of Chemical Engineering)*, Sept 27-Oct 1, 2015. (Poster Presentation).

Wiedmeyer, V., Voigt, A., Le Borne, S., and Sundmacher, K. Experimentelle Aggregation im Wirbelschichtkristaller zur Modellierung von Aggregationskernen, In *ProcessNet Jahrestreffen der Fachgruppe "Kristallisation"*, March 6-9, 2018. (Oral Presentation).

Wiedmeyer, V., Voigt, A., and Sundmacher, K. Formentwicklung bei der kontinuierlichen Kristallisation. In *ProcessNet Jahrestreffen der Fachgruppe "Kristallisation"*, March 18-20, 2015. (Oral Presentation).

Wiedmeyer, V., Voigt, A., and Sundmacher, K. Analysis of growth kinetics of a multivariate crystal population in a continuous crystallizer. In *PARTEC 2016 (International Congress on Particle Technology)*, April 19-21, 2016. (Oral Presentation).

Wiedmeyer, V., Voigt, A., and Sundmacher, K. Continuous crystallization in a helically-coiled flow tube facilitates control over the crystal size and shape distribution. In *ISIC20 (The 20th International Symposium on Industrial Crystallization)*, Sept 3-6, 2017. (Oral Presentation).

Wiedmeyer, V., Voigt, A., and Sundmacher, K. Crystal Growth Simulation in a Continuously Operated Helically Coiled Tube. In *ECCE12 (The 12th European Congress of Chemical Engineering)*, Sept 15-19, 2019. (Poster Presentation).

Wiedmeyer, V., Voigt, A., Sundmacher, K., Anker, F., Bartsch, C., John, V., Ahrens, R., and Le Borne, S. Growth and Aggregation in a Shape Selective Fluidized Bed Crystallizer: Experiments versus Numerical Simulation, In *PARTEC 2019 (International Congress on Particle Technology)*, April 9-11, 2019. (Poster Presentation).